

# JOINT STRAIN ANALYSIS IN CARDIAC MRI

A. M. Hunfuko Asanka Abeykoon

B.Sc(Hons) in Information Technology, University of Moratuwa

A THESIS SUBMITTED FOR THE DEGREE OF  
*MASTER OF ENGINEERING*  
DEPARTMENT OF ELECTRICAL AND COMPUTER  
ENGINEERING  
NATIONAL UNIVERSITY OF SINGAPORE

2014

I would like to dedicate this thesis to my loving parents, and family ...

# DECLARATION

I hereby declare that this thesis is my original work and it has been written by me in its entirety. I have duly acknowledged all the sources of information which have been used in the thesis.

This thesis has also not been submitted for any degree in any university previously.

A handwritten signature in blue ink, appearing to read 'A. M. Hunfuko Asanka Abeykoon', is positioned above a horizontal line.

---

A. M. Hunfuko Asanka Abeykoon on 8<sup>th</sup> July 2014

# Acknowledgements

First and foremost, I would like to express my profound gratitude to my supervisor Assistant Prof. Sun Ying for her encouragement, enthusiasm and support throughout the course of my research. Her guidance meant a lot to me and helped me to develop my skills as a researcher who is new to the field of medical image analysis. Her encouraging words and strong backing up in crucial situations in my M.Eng candidature provided me a great comfort to continue my research works.

I would also like to thank my co-supervisor Prof. Ryohei Nakatsu for his support throughout the time I spend in NUS. The advancements made over the years would not have been possible without his invaluable support in my academic matters. I would take this opportunity to thank my previous supervisor A/Prof. Adrian David Cheok, for helping me in various situations and for giving me the opportunity to work and study in Keio NUS CUTE Center. It was a pleasure doing research with him and he was always there for me when I need help.

I also appreciate the kind advises and support of Prof. P. Gopalakrishnakone for my further development and career. I specially thank him for giving me the opportunity to work in his research projects and helping me in crucial situations.

I would also like to thank for the kind advises and support of Dr. Wei Dong through out my research activities.

Sincere thanks also go to Dr. Ajith Madurapperuma who was former deputy director of Cute Center for his support, guidance and advises since my undergraduate studies. Also I would like to thank Prof. Ellen Do and Dr. Henry Duh for their help during my candidature.

I am grateful to my friends in the lab, Kasun Karunanayaka, Chamari Edirisinghe, Nimesha Ranasinghe, Dilrukshi Abeyrathna, Sanath Siriwardana, Roshan Peiris, Channa Senevirathna, Prabhash Kumarasinghe, Elham Saadatian, Hooman Samani, Jeffrey Koh, Kenning Zhu, Wang Xuan, Wei Jun, Yong Soon, Eng Tat, James Teh, and Xavier Roman for their great support and making my research a pleasant experience at Keio-NUS Cute Center. Sincere thanks also go to all my friends

in vision and machine learning lab and ECE. I would also like to thank my friends Rashed Bhuyan, Ngawang Drakpa, Joshua Varughese and Gowtham Muthusamy, Nimantha Thushan, Sumanaruban Rajadurai, Girisha Durrel De Silva, Rasitha Senarathne and Thilini Shiromani for their friendship and support during the stay in UTOWN.

I also like to extend my gratitude to Dr. Pahala Gedara Jayathilake, Dr. Suranga Nanayakkara, Dr. Rajesh C Panicker for their support. I also appreciate Mr. D.K. Withanage, Prof. Dileeka Dias and Prof. Asoka Karunananda for their kindness and support during my undergraduate studies in University of Moratuwa. Also I would like to thank my friends Sasanka Fernando, Supunmali Ahangama, Sangar Kajanan, Shalinda Adhikari, Ajith Kumara, Manura Pinnaduwa, Pradeep Senanayake, Asanka Sriilal, Nayana Adassuriya, Amila Asiri Aberathna, Asantha Rupasinghe, Niranka Perera and others for making me happy and providing help in certain situations.

Thank you very much for the CUTE center admin staff members Sykin, Rashika, Ngu Wah, Sofi, Marie, Hariyati, Malcom and the ECE department staff members for their help and support provided.

To my parents, father (Jayantha Abeykoon) and mother (Anoma Sriyani Abhayawardana), I express my deep love and gratitude. I would also like to commemorate my late grandfather and grandmother for the love and support they always gave me. Special thank also go to my brothers (Anju Asela and Ayantha Sameera) and my sister (Yumali Naveesha) for their love and support. I would also like to express my sincere gratitude to my friend Ravindra Karunarathna and Roshan Priyankara for their support to me and my family. My thanks also go to Cheralyn Diasanta and Mercedes Diasanta for their love, support and kindness. I would also like to thank my aunties Anula, Harshani, Seetha, Sujatha and uncle Prasanna for their love and support.

Lastly, and most importantly, I am grateful to Gabriel Rojo, Celestial Rojo for their love, support and all the sacrifices they made.

### **Special Acknowledgment :-**

*This research is supported by the Singapore National Research Foundation under its International Research Center Keio-NUS CUTE Center @ Singapore Funding Initiative and administered by the IDM Program Office.*

# Abstract

Cardiac wall motion analysis is a widely used technique for identifying many different types of cardiovascular diseases. Regional abnormalities in myocardial function can be detected with myocardial strain measurements derived from tagged CMR data and of myocardial infarction can be detected with LGE (Late Gadolinium Enhanced) CMR. However, the obvious tag fading effect in tagged CMR image sequences prevents having an accurate motion and strain estimation through out the full cardiac cycle. In order to avoid this issue and to have more robust motion estimation, this thesis proposes a novel optical flow motion estimation method that uses both tagged and cine CMR data simultaneously. Moreover, the results of the proposed method is validated using both real and synthetic data.

Further, this thesis attempts to identify correlation between myocardial infarction percentage/location and myocardial strain. By adding the strain measures calculated throughout the full cardiac cycle, we present an extended correlation analysis between strain measures and infarct percentage. The correlation study has carried out by considering different orientations of left ventricle.

The experimental results suggest that, the tag fading effect and its implications in tagge CMR can be compensated by using both cine and tagged CMR data simultaneously. Besides, it suggests an optical flow based solution can be used effectively to estimate motion jointly using both cine and tagged CMR data.

The results from the correlation study indicate that inferior, inferolateral, and anterolateral segments tend to show stronger correlations than the other segments of LV. Further, the correlation study suggests that Eulerian strains are also having a similar prognosis value as same as with Lagrangian strains in regional and global myocardial function analysis.

The contributions of this thesis includes: (1) a novel optical flow based cardiac motion estimation algorithm which uses both tagged and cine CMR data, and (2) extended correlation analysis between infarct percentage and global/regional myocardial strain measures.

# List of Abbreviations

<b>1D</b>	One dimensional
<b>2C</b>	Two-chamber
<b>2D</b>	Two dimensional
<b>3D</b>	Three dimensional
<b>4C</b>	Four-chamber
<b>4D</b>	Four dimensional
<b>AHA</b>	American Heart Association
<b>BEM</b>	Boundary element method
<b>CAD</b>	Coronary artery disease
<b>CMR</b>	Cardiac magnetic resonance
<b>CO</b>	Cardiac output
<b>CS</b>	Circumferential Strain
<b>CSPAMM</b>	Complementary SPAMM
<b>CT</b>	Computed tomography
<b>CVD</b>	Cardiovascular diseases
<b>DENSE</b>	Displacement encoding with stimulated echoes
<b>DICOM</b>	Digital Imaging and Communications in Medicine
<b>ECG</b>	Electrocardiography
<b>ED</b>	End of ventricular diastole
<b>EDV</b>	End diastolic volume
<b>EF</b>	Ejection Fraction
<b>EFFD</b>	Extended free form deformation
<b>ES</b>	End of ventricular systole
<b>ESV</b>	End systolic volume
<b>FE</b>	Finite element
<b>FEM</b>	Finite element model
<b>FFD</b>	Free form deformation
<b>GRPM</b>	Generalized robust point matching
<b>HARP</b>	Harmonic phase
<b>HR</b>	Heart Rate
<b>I/M%</b>	Infarct percentage



---

<b>IOP</b>	The ImageOrientationPatient field in standard DICOM header
<b>IPP</b>	The ImagePositionPatient field in standard DICOM header
<b>LA</b>	Long-axis
<b>LAD</b>	Left anterior descending
<b>LGE</b>	Late gadolinium enhanced
<b>LV</b>	Left ventricle
<b>LVM</b>	Left ventricular Mass
<b>LVV</b>	Left ventricular Volume
<b>MI</b>	Myocardial Infarction
<b>MRI</b>	Magnetic resonance imaging
<b>MSD</b>	Mean of squared differences
<b>MVO</b>	Microvascular obstruction
<b>NCC</b>	Normalized cross correlation
<b>NMI</b>	Normalized mutual information
<b>PS</b>	The PixelSpacing field in standard DICOM header
<b>RA</b>	Right Atrium
<b>RMSE</b>	Root Mean Squared Error
<b>ROI</b>	Region of interest
<b>RV</b>	Right Ventricle
<b>SA</b>	Short-axis
<b>SinMod</b>	Sine wave modeling
<b>SPAMM</b>	SPAtial Modulation of Magnetization
<b>SPECT</b>	Single-photon emission computed tomography
<b>STD</b>	Standard deviation
<b>SV</b>	Stroke Volume

# Contents

<b>List of Abbreviations</b>	<b>vii</b>
<b>Contents</b>	<b>ix</b>
<b>List of Figures</b>	<b>xii</b>
<b>List of Tables</b>	<b>xv</b>
<b>1 Introduction</b>	<b>1</b>
1.1 Motivation . . . . .	1
1.2 Scope and Contributions . . . . .	5
1.3 Thesis Organization . . . . .	6
<b>2 Background and Related Work</b>	<b>7</b>
2.1 Anatomy and Structure of the Heart . . . . .	7
2.1.1 Main Cycles of Heart . . . . .	8
2.2 Cardiovascular Diseases . . . . .	10
2.3 Detecting Coronary Artery Disease . . . . .	11
2.4 Imaging Planes and Standardized Myocardial Segmentation . . . . .	12
2.5 Cardiac MRI . . . . .	17
2.5.1 Tagged CMR . . . . .	17
2.5.2 Cine CMR . . . . .	20
2.5.3 LGE CMR . . . . .	22
2.6 Structural and Functional Descriptors . . . . .	22
2.6.1 Global Functional Parameters . . . . .	23
2.6.2 Regional Functional Parameters . . . . .	24

2.6.2.1	Strain . . . . .	24
2.6.2.2	Apico-basal Twist (Torsion) . . . . .	25
2.6.3	Infarct Quantification . . . . .	26
2.7	Cardiac Motion Estimation Methods . . . . .	27
2.7.1	Feature Based Motion Estimation . . . . .	28
2.7.1.1	Tracking Land marks . . . . .	28
2.7.1.2	Deformable Models . . . . .	30
2.7.2	Direct Motion Estimation . . . . .	31
2.7.2.1	Harmonic Phase MRI (HARP) . . . . .	31
2.7.2.2	Local Sine Wave Modeling(SinMod) . . . . .	31
2.7.2.3	Gabor Filter Banks . . . . .	32
2.7.2.4	Registration-Based Methods . . . . .	32
2.7.2.5	Optical Flow Based Methods . . . . .	33
2.7.3	Joint Motion Estimation Methods . . . . .	37
2.8	Validation of Cardiac Motion Estimation Methods . . . . .	38
<b>3</b>	<b>Joint Motion Estimation Using Cine and Tagged CMR</b>	<b>40</b>
3.1	Overview . . . . .	40
3.2	Spatial and Temporal Alignment of Tagged and Cine Images . . .	41
3.3	Segmentation of Myocardium . . . . .	43
3.4	Algorithm Development . . . . .	43
3.4.1	Recursive Least-Squares Estimation(RLSE) . . . . .	48
3.4.2	Strain Estimation . . . . .	51
3.5	Evaluation and Experiments . . . . .	52
3.5.1	Synthetic Data - Method A . . . . .	52
3.5.2	Synthetic Data - Method B . . . . .	55
3.5.3	Experiments with Real Data . . . . .	62
3.6	Results . . . . .	63
3.6.1	Results with Simulated Data . . . . .	63
3.6.1.1	Synthetic Data - Method A . . . . .	63
3.6.1.2	Synthetic Data - Method B . . . . .	63
3.6.2	Results with Real Data . . . . .	63
3.7	Discussion . . . . .	66

<b>4</b>	<b>Correlation Analysis</b>	<b>74</b>
4.1	Objective . . . . .	74
4.2	Data . . . . .	75
4.3	Data Processing . . . . .	76
4.3.1	Infarct Quantification . . . . .	76
4.3.2	Strain Quantification . . . . .	76
4.4	Statistical Analysis . . . . .	80
4.5	Results and Discussion . . . . .	85
4.6	Conclusion . . . . .	89
<b>5</b>	<b>Conclusion and Future Work</b>	<b>90</b>
5.1	Conclusion . . . . .	90
5.1.1	Cardiac Motion Estimation . . . . .	90
5.1.2	Correlation Analysis . . . . .	91
5.2	Limitations and Future Work . . . . .	92
	<b>Bibliography</b>	<b>93</b>

# List of Figures

1.1	Distribution of CVD deaths due to heart attacks, strokes and other types of cardiovascular diseases, <i>males</i> (left), <i>females</i> (right) [1] . .	2
2.1	Anatomy(left) and blood flow(right) of heart [2] . . . . .	8
2.2	Orientation of major body planes with respect to patient and their corresponding appearance on bright blood imaging sequences [3] . .	13
2.3	Orientation of major cardiac planes with respect to heart and their corresponding appearance [3] . . . . .	14
2.4	Left: the basal, mid-cavity and apical SA slices; right: the 4C and 2C LA views. IDs of the 17-segment model recommended by the AHA [4] . . . . .	15
2.5	17 myocardial segments and the recommended nomenclature [4] . .	16
2.6	Orientation of major cardiac planes with respect to heart and their corresponding appearance [4] . . . . .	16
2.7	Corresponding tagged (left), cine (middle) and LGE (right) SA images obtained from a mid SA slice . . . . .	17
2.8	First 20/16 frames of a SPAMM tagged basal SA slice. Frame numbers are indicated at top left corner of each image . . . . .	19
2.9	First 16 of 20 frames of a basal cine SA slice. Frame numbers are indicated at top left corner of each image . . . . .	21
2.10	A stack of SA LGE images of a patient [5] . . . . .	22
2.11	Schematic diagram demonstrating the three dimensional circumferential - radial - longitudinal (RCL) coordinate system used for strain calculation [6] . . . . .	25

2.12	Bull's eye plot of a myocardium which shows I/M% in standard 16 segments [5] . . . . .	27
2.13	Abstract hierarchical computational model of cardiac motion estimation techniques . . . . .	29
3.1	The hierarchical computational process of cardiac motion estimation	42
3.2	The motion estimated between two tagged MR images (top-left and top-right) is used as ground truth. The ground truth is illustrated using a color wheel (bottom-left) and using vector fields within myocardium (bottom-right). . . . .	54
3.3	The pair of tagged CMR images created in synthetic data - Method A, a) known motion interpolated image and b) after adding rician noise to the image in a). . . . .	55
3.4	Results obtained with synthetic data - method A (without noise) is illustrated using a color wheel. . . . .	56
3.5	Results obtained with synthetic data - method A (with noise) is illustrated using a color wheel. . . . .	57
3.6	Process of generating first synthetic tagged CMR image in synthetic data - method B. . . . .	60
3.7	The first 4 frames of synthetic tagged CMR sequence obtained using synthetic data - method B. . . . .	60
3.8	Simulated tag fading effect in synthetic tagged CMR sequence using synthetic data - method B. . . . .	61
3.9	The first 4 frames of synthetic cine CMR sequence obtained using synthetic data - method B. . . . .	61
3.10	Ground truth radial motion between each pair of frames in synthetic tagged and cine sequences in synthetic data - method B. . . . .	62
3.11	Pixel error bar plot of the results in Table 3.4 . . . . .	64
3.12	Angle error bar plot of the results in Table 3.4 . . . . .	64
3.13	Global circumferential and radial strains of a basal slice calculated within whole myocardium . . . . .	66
3.14	XX,XY,YY Eulerian strains of a basal slice calculated in whole myocardium . . . . .	67

3.15	Circumferential strain of a basal slice calculated according to standard segmentation . . . . .	67
3.16	Radial strain of a basal slice calculated according to standard segmentation . . . . .	68
3.17	XX Eulerian strains of a basal slice calculated according to standard segmentation . . . . .	68
3.18	XY Eulerian strains of a basal slice calculated according to standard segmentation . . . . .	69
3.19	YY Eulerian strains of a basal slice calculated according to standard segmentation . . . . .	69
3.20	Color map used for strain illustrations . . . . .	70
3.21	Evolution of radial strain visualized using color map in Figure 3.20 . . . . .	70
3.22	Evolution of circumferential strain visualized using color map in Figure 3.20 . . . . .	71
3.23	Tracked points along 16/20 frames of a basal slice. Frame numbers are indicated at the top-right of each image . . . . .	72
3.24	Trajectories of selected Points in Figure 3.23 . . . . .	73
4.1	The scatter plot of Max. and Min. of regional Lagrangian strains calculated over whole cardiac cycle (I/M% was normalized in to [0 1]) . . . . .	78
4.2	The scatter plot of Max. and Min. of regional Eulerian strains calculated over whole cardiac cycle (I/M% was normalized in to [0 1]) . . . . .	79

# List of Tables

2.1	Major types of cardiovascular diseases . . . . .	10
3.1	Optical flow methods used for evaluation and their abbreviations ( <i>Only the proposed method is using both tagged and cine CMR images while the other methods are only using tagged CMR images</i> ) . .	53
3.2	Mean and STD of angle and pixel errors obtained from synthetic data method A, with out adding noise (abbreviations are indicated in Table 3.1) . . . . .	55
3.3	Mean and STD of angle and pixel errors obtained from synthetic data- method A, with added noise (abbreviations are indicated in Table 3.1) . . . . .	58
3.4	Angle and pixel error of optical flow obtained after applying the methods in Table 3.1 to synthetic data - method B. . . . .	65
4.1	Abbreviation and description of strain measures used for correlation analysis . . . . .	77
4.2	The results of slice-wise correlation analysis between I/M% strain measures in Table 4.1. $*p < 0.05$ , $**p < 0.01$ , $***p < 0.001$ and $\odot$ indicates $p > 0.05$ . . . . .	81
4.3	The results from standard AHA segment-wise correlation Analysis [Segments 1-8] between I/M% strain measures in Table 4.1. $*p < 0.05$ , $**p < 0.01$ , $***p < 0.001$ and $\odot$ indicates $p > 0.05$ . . . . .	82
4.4	The results from standard AHA segment-wise correlation Analysis [Segments 9-10] between I/M% strain measures in Table 4.1. $*p < 0.05$ , $**p < 0.01$ , $***p < 0.001$ and $\odot$ indicates $p > 0.05$ . . . . .	83



4.5    he results from standard AHA vertical segments-wise correlation  
Analysis between I/M% strain measures in Table 4.1.  $*p < 0.05$ ,  $**$   
 $p < 0.01$ ,  $***p < 0.001$  and  $\circlearrowright$  indicates  $p > 0.05$ . Ant-*anterior*,  
AS-*anteroseptal*, IS-*inferoseptal*, Inf-*inferior*, IL-*inferolateral*, AL-  
*anterolateral* . . . . . 84

# Chapter 1

## Introduction

Firstly, this thesis aims at automatic motion and strain analysis of the heart using cardiac magnetic resonance imaging (CMR). The proposed method uses both tagged and cine CMR data in order to estimate the motion within myocardium and calculate strain. A synthetically generated CMR image sequences have been used to validate the proposed motion estimation algorithm. Secondly, the correlations between myocardial infarct percentage (I/M%) and different strain measures of myocardium are also presented. In order to quantify infarctions, late gadolinium enhanced (LGE) CMR data is used. Section 1.1 briefly introduces the motivation behind this thesis. The scope and contributions of the thesis are highlighted in Section 1.2 and Section 1.3 gives an overview of the organization of this thesis.

### 1.1 Motivation

Cardiovascular diseases (CVD) are the number one cause of death and are projected to remain so [7]. Among the various types of CVDs, coronary artery disease

or ischemic heart disease is one of the leading causes of death. According to the World Health Organization (WHO), 17.3 million people died from CVDs in 2008 (30% of all global deaths) and 7.3 million were due to coronary heart disease (CAD) and 6.2 million were due to stroke [7] [1]. The distribution of global CVD deaths is shown in Figure 1.1. Detecting these CVDs early is the key to prevent the deaths and if the diseases are identified early, inexpensive treatments are available [7] [1]. With advances in spatial and temporal resolution and with increased

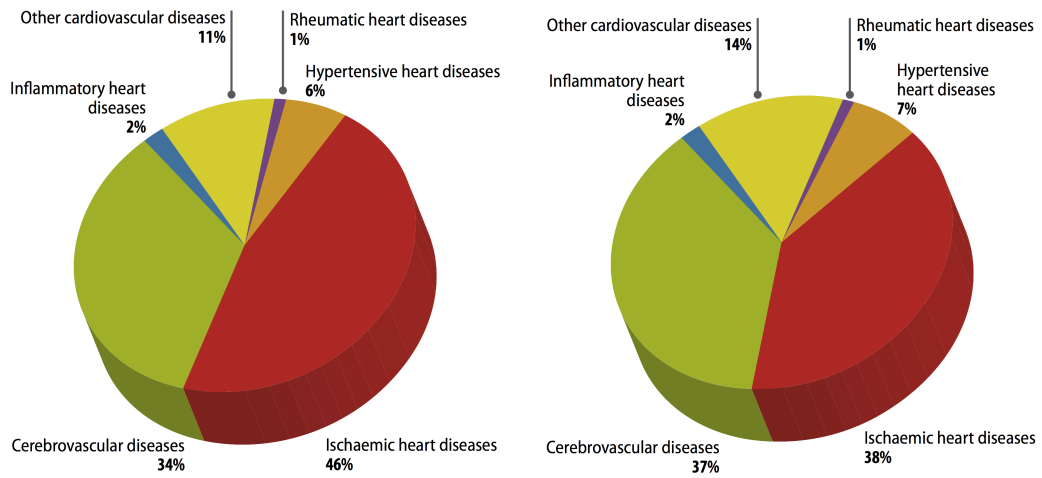


Figure 1.1: Distribution of CVD deaths due to heart attacks, strokes and other types of cardiovascular diseases, *males* (left), *females* (right) [1]

availability of digital imagery technologies such as Magnetic Resonance Imaging (MRI), CT, Echocardiography and SPECT, automated image analysis has become viable technology in CVD diagnosis and treatments. Among these technologies, cardiac MRI plays a major role due to its advantages over other imaging modalities. These cardiac MRI technologies include various imaging techniques such as tagged MRI, perfusion MRI, cine MRI and LGE MRI, which are dedicated to different types of diagnosis and is being used widely because of its advantages on

functional, structural analysis and viability assessment of heart.

The motion of the ventricular walls prognosis about the CVDs. In CAD, plaque is building up along the inner walls of the arteries of the heart (scar or infarction) [8] and it results in a loss of cardiac function. These infarctions affects the LV to a greater extent because of it's larger size and greater demand for energy [9]. Hence, tagged CMR is widely used in analyzing ventricular motion of the heart. Even though tagged CMR can provide a primary way of visualizing cardiac motion, fast and accurate image analysis methods have been developed by using tagged MRI data and these methods can be used for routine quantitative analysis [10]. However, the tag patterns in tagged CMR fades due to the  $T_1$  relaxation of magnetization and therefore, motion analysis over full cardiac cycle is a challenging task. Tag fading and noise in tagged CMR image sequences tend to give erroneous results in the latter part of the cardiac cycle (usually in diastolic phase). Moreover, this issue prevents having an accurate analysis of cardiac motion and strain over the full cardiac cycle and usually it is only limited to systolic phase of cardiac cycle. Further, researchers have proposed various methods to overcome the tag fading issue, in order to have a robust and accurate motion estimation of myocardium. Hence, this thesis is mainly aimed at developing an automatic cardiac motion estimation method that can minimize the error due to tag fading effect and noise. In order to minimize the effect from tag fading, this thesis proposes a method that estimate cardiac motion jointly using both tagged and cine CMR data. Subsequently, the estimated motion is used to calculate strain of LV that can be later used for the analysis of CVDs. Moreover, this thesis proposes an optical flow based method in order to have a dense motion field estimation and faster calculation.

LGE CMR is another main imaging method used in diagnosis of CAD. LGE CMR provides capability to visualize and discriminate infarct regions within myocardium directly. However, LGE CMR is relatively less available and inherent resolution issues of MRI prevent exploiting infarctions in full 3D range. In addition, LGE CMR requires the injection of contrast agent which poses risk for certain patients. Hence, direct quantification of infarction from other prognostic information such as motion, strain, ejection fraction and wall thickening is vital [11]. Moreover, noninvasive monitoring of regional myocardial function after survived myocardial infarction is proffered in clinical practice [12], since quantifying the transmural extent of the scar is important in determining the chance of recovery after intervention [13] [14]. Hence, the correlation between infarct size/percentage and regional cardiac function descriptors such as motion, strain, ejection fraction and wall thickening are analyzed in order to provide prognosis information. However, such correlation analyses which is based on strain measures also suffers from the erroneous motion and strain estimation results due to the tag fading effect. There are only few works can be found in literature that are used strain data over full cardiac cycle and most of the analysis is limited to systolic phase. In addition, the correlation between strain measures and infarct size/percentage is not well defined [15]. Therefore, this thesis presents the analysis of the correlation between infarct percentage and motion/strain throughout the whole cardiac cycle. Moreover, this thesis uses maximum and minimum efficient, Lagrangian and Eulerian strains take place during the full cardiac cycle, in order to analyze the correlation with infarct percentage.

## 1.2 Scope and Contributions

This thesis aims to contribute new algorithms for motion estimation of cardiac magnetic resonance imaging sequences. The main focus of the proposed motion estimation method is to minimize the tag fading effect issues of tagged CMR. The starting point has been the optical flow based methods. Firstly, our purpose is to evaluate the feasibility of a motion estimation method based on optical flow technique which uses both tagged and cine CMR sequences. The SA slices of tagged and cine CMR data are used to estimate 2D motion over the full cardiac cycle and 2D strain tensors are calculated subsequently. These strain tensors are then used to derive Lagrangian, Eulerian and Efficient strains.

Secondly, this thesis aims to identify any correlation exists between myocardial strain measures and infarctions. LGE CMR data is used to quantify infarct percentage. These infarct data is analyzed subsequently with the maximum and minimum of each strain throughout the cardiac cycle. Moreover, the correlation is analyzed by considering different orientations of LV.

To summaries, this thesis makes the following contributions toward joint analysis of CMR images:

- Introducing a new motion estimation method based on optical flow which uses both cine and tagged CMR data simultaneously.
- Comparison and evaluation of results with the established methods using synthetic image sequences.
- Evaluation of the results obtained with real tagged CMR sequences.
- Analysis of correlation between myocardial strain (global and regional) and

infarct percentage by considering the strain data for whole cardiac cycle.

- Incorporating both lagrangian and eulerian strains for the correlation analysis.

### 1.3 Thesis Organization

Chapter 2 describes the background medical context and the related works. Firstly, the anatomy and physiology of the heart is presented. After that, a description of cardiac motion estimation methods using tagged CMR is provided.

In Chapter 3, the scientific background about motion estimation is presented. The concept of optical flow is explained, and a review of the most relevant techniques of motion estimation is mentioned.

In Chapter 3, the motion estimation method based on the optical flow is presented. The results on synthetic and real cardiac MRI sequences are presented and validation methods are described along with the results obtained in comparison to the reference methods.

Chapter 4 presents the correlation analysis between myocardial strain measures and infarct percentage. Finally, the main conclusions and future topics of research are presented in Chapter 5.

# Chapter 2

## Background and Related Work

This chapter describes the main aspects of anatomy, physiology and function of the heart, together with the most important cardiovascular diseases. Cardiac imaging techniques are briefly explored. Moreover, cardiac motion estimation and validation methods are discussed while giving more focus to optical flow based methods.

### 2.1 Anatomy and Structure of the Heart

The heart is a vital organ in human body and main function of the heart is circulating blood around the body and pumping blood through blood vessels to all body tissues. The human heart is nearly the size of a human fist and pumps around 2000 gallons of blood per day while beating around 80,000 100,000 times. The heart consists of four chambers and the largest two chambers are called the ventricles, while the smaller two are called the atria (please see Figure 2.1).

- The RA receives blood from the veins and pumps it to the RV.



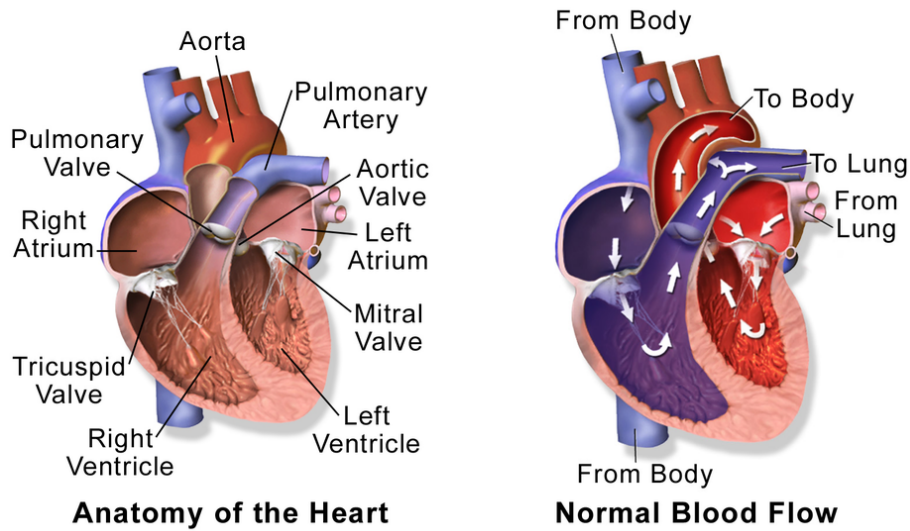


Figure 2.1: Anatomy(left) and blood flow(right) of heart [2]

- The RV receives blood from the RA and pumps it to the lungs, where it is loaded with oxygen.
- The LA receives oxygenated blood from the lungs and pumps it to the LV.
- The LV (the strongest chamber) pumps oxygen-rich blood to the rest of the body. The LV's vigorous contractions create our blood pressure.

### 2.1.1 Main Cycles of Heart

In each cardiac cycle, the atria and ventricles alternately contract and relax in order to move blood from areas of higher pressure to areas of lower pressure. The contraction of these chambers increases the pressure within the chamber and relaxation allows to decrease the pressure. This repeated contraction and relaxation cycle allows the circulation of blood through out the body continuously. Approx-

## 2. Background and Related Work

---

imately, when a heart rate is 75 beats/min, a cardiac cycle lasts 0.8 sec. The correlated events occur during a cardiac cycle is mainly divided in to three phases as below;

**Atrial Systole:** This is a relatively short phase which takes place for about 0.1 seconds. During this phase left and right atria are contracting and the blood is pumped into the ventricles while the ventricles are also relaxed. The end of this phase is also called end of ventricular diastole (ED) and the blood volume is called the end-diastolic volume (EDV).

**Ventricular Systole:** During this phase(about 0.3 seconds) the ventricles are contracting and the atria are relaxed. As they begin to contract the mitral and tricuspid valves close to prevent any backflow into the atria. At the end of this phase the pulmonary and aortic valves close and diastole begins again. The end of this phase is also called end of ventricular systole (ES) and the blood volume is called the end-systolic volume (ESV).

**Diastole:** During this phase blood flows into the heart and it takes about 0.4 seconds. Both atria and ventricles are relaxed and as a result blood comes into the atria through the pulmonary veins (left atrium) and the superior and inferior vena cava (right atrium). From the left and right atria the blood flows directly into both ventricles because both the mitral and tricuspid valves are open. The aortic and pulmonary valves are closed during this phase to prevent the reverse flow of blood from the aorta and pulmonary artery. When the heart beats faster, this phase becomes shorter.

## 2.2 Cardiovascular Diseases

Cardiovascular diseases (or heart diseases) are any disorders which are related to both heart (cardio) and/or the blood vessels (vascular) including arteries, capillaries, and veins. Table 2.1 shows the major types of cardiovascular diseases. Among these diseases, the coronary artery disease is the most common type of disease or ischemic heart disease (IHD) and this disease is caused by plaque building up along the inner walls of the arteries of the heart, which narrows the arteries and reduces blood flow to the heart [8]. This plaque is a deposit of cholesterol, fat, calcium, and other cellular sludge from blood. The coronary artery disease is also the main cause of heart attack (**Myocardial Infarction - MI**) which may occur suddenly due to various risks factors such as age, sex, family history, smoking, hypertension, diabetes, obesity, ...etc. During a heart attack blood stops flowing properly to part of the heart and heart muscles due to lack of oxygen supply [16]. This condition which results in reducing blood and oxygen supply to the heart is called **cardiac ischemia**.

Table 2.1: Major types of cardiovascular diseases

Name	Description
Coronary artery disease	Blocking of arteries supplying blood to the heart
Cardiomyopathy	Diseases of cardiac muscle
Hypertensive heart disease	diseases of the heart secondary to high blood pressure
Valvular heart disease	Diseases of the valves between heart chambers
Heart failure	Inability of heart to pump enough blood to organs

Coronary artery disease (CAD) is the one of the major causes of cardiomyopathy, which literally means "heart muscle disease", is the deterioration of the function of the myocardium (i.e., the actual heart muscle) for any reason [17]. Peo-

ple with cardiomyopathy are often at risk of arrhythmia or sudden cardiac death or both.

### 2.3 Detecting Coronary Artery Disease

The basic diagnosis process includes physical examination, blood tests, and electrocardiogram tests (ECG). However, depending on the initial diagnosis, one or more diagnostic tests might be prescribed for a more detailed analysis of the symptoms [18], [19]. In order to further detect ischemia, an invasive or non-invasive imaging method can be used.

Cardiac catheterization (heart cath) can be considered as a widely used invasive method which is used to detect ischemia. In “Catherization” process, a long, thin, flexible tube called a catheter is put into a blood vessel in patients arm, groin (upper thigh), or neck and threaded to the heart. Then through the catheter, diagnostic tests and treatments can be executed [19].

In order to detect ischemia, a noninvasive coronary imaging can be done using x-ray angiography to detect narrowing that reduces or obstructs the flow of blood. Electrocardiography or MRI can also be used to detect ischemia instead of x-ray angiography.

Finally, this assessment can also be performed by means of the evaluation of cardiac motion. Due to ischemia, motion irregularities take place and a proper motion analysis of heart can have a significant impact on diagnosing ischemia [20]. Hence, the estimation of the myocardial motion, wall thickening, strain and detection of abnormal patterns has become vital. Moreover, enhanced regional function assessment in terms of wall motion and strain is one of the main areas of

focus in new cardiac imaging modalities and post processing tools.

Echocardiography (ultrasound) and cardiac MRI can be considered as the most popular methods that are used to estimate global and regional cardiac function. Due to noninvasive and real time nature of echocardiography, it has also become an important imaging modality. However, echocardiography has a poor image quality relative to MRI and echocardiography allows imaging of the body only through certain windows. In addition to that, echocardiography images have a higher noise than MRI images. Hence, MRI has become more popular and the main advantages of cardiac MRI can be listed as below;

- MRI is noninvasive and uses nonionizing radiation.
- 3D and 4D imaging capabilities.
- good soft tissue contrast.
- Imaging capability at arbitrary orientations.
- Ability to diagnose broad range of conditions.
- Ability to evaluate both the structure and function of the heart.

### 2.4 Imaging Planes and Standardized Myocardial Segmentation

Two main coordinate systems are used for cardiac MR and it includes body planes (scanner) and the cardiac planes. Body planes are oriented orthogonal to the long

axis of the body and consist of axial, sagittal, and coronal planes as shown in Figure 2.2 [3]

Standard cardiac planes include short axis, horizontal long axis (four-chamber view), and vertical long axis (two-chamber view) as shown in Figure 2.3. However, the American Heart Association (AHA) has suggested and introduced a standard methodology to segment myocardium and adjacent cavity for different types of cardiac imaging modalities (CMR,PET,CT...etc). One of the main advantages of the standardization is to avoid difficulties in accurate intra and cross-modality comparisons for clinical patient management and research [4]. This dissertation has also followed the Standardized Myocardial Segmentation proposed by AHA.

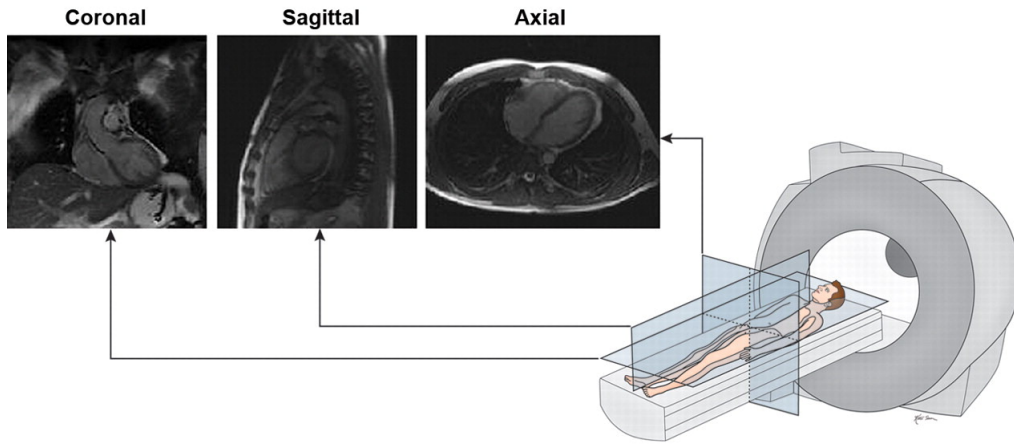


Figure 2.2: Orientation of major body planes with respect to patient and their corresponding appearance on bright blood imaging sequences [3]

According to AHA, cardiac planes used in all imaging modalities should be oriented relative (90 angles) to long axis of the left ventricle and selected planes include short axis, vertical long axis, and horizontal long axis (see Figure 2.3). Moreover, it is suggested that the heart should be divided into equal thirds per-

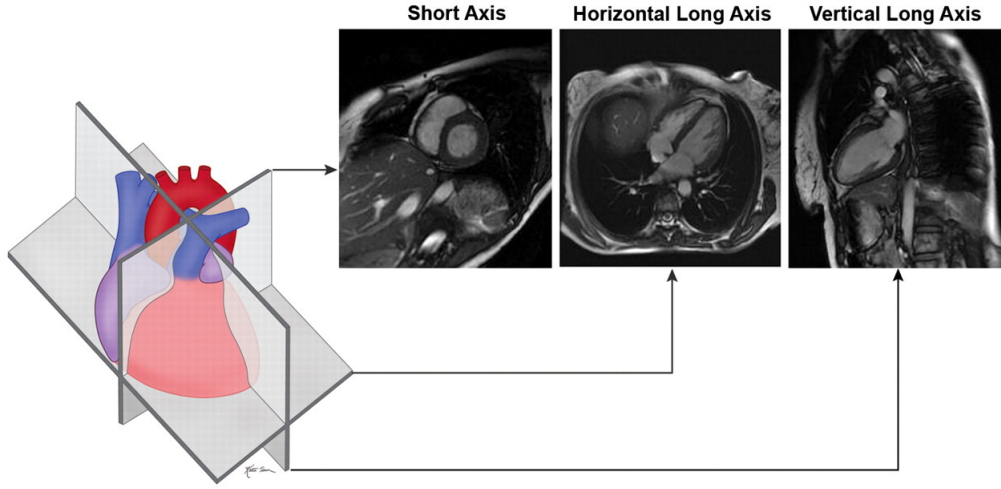


Figure 2.3: Orientation of major cardiac planes with respect to heart and their corresponding appearance [3]

pendicular to the long axis and will generate three circular basal, mid-cavity, and apical SA slices of the LV.

According to the proposed standard, the heart should be divided into 17 segments for assessment of the myocardium and the left ventricular cavity as show in Figure 2.4 and names for the myocardial segments should define the location relative to the long axis of the heart and the circumferential location [4]. Based on the circumferential location, basal and mid cavity slices are divided in to 6 segments with each segment covering 60 degrees angle and apical slice is divided in to 4 segments. The 17<sup>th</sup> segment which is the true apex is derived from 2C or 4C views. However, this dissertation has not considered the 17<sup>th</sup> segment for strain calculations. The bull's eye plot in Figure 2.5 shows the locations and recommended names for each segment.

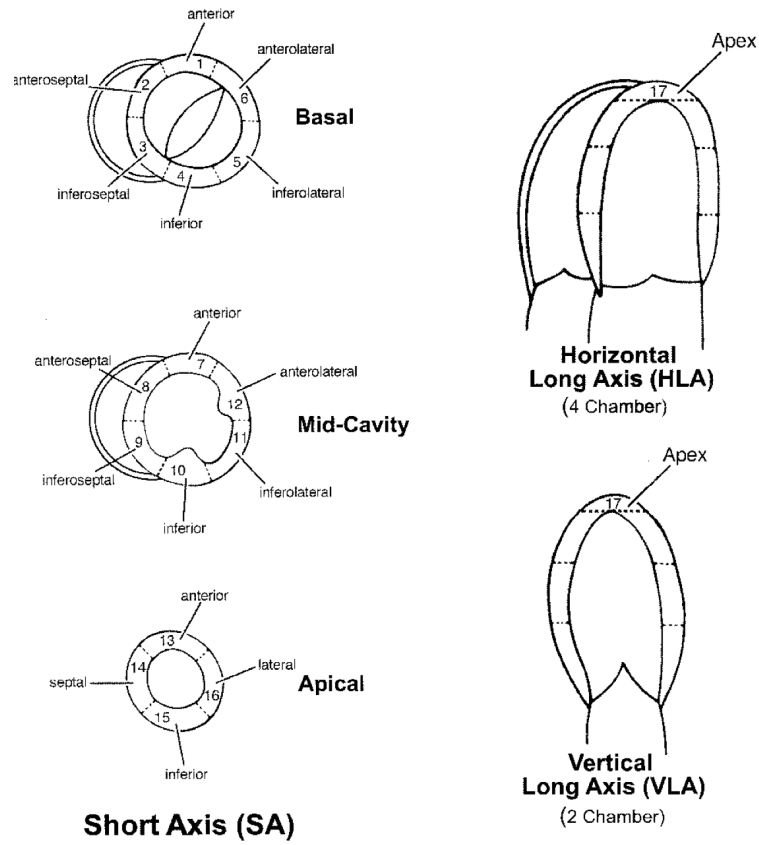


Figure 2.4: Left: the basal, mid-cavity and apical SA slices; right: the 4C and 2C LA views. IDs of the 17-segment model recommended by the AHA [4]



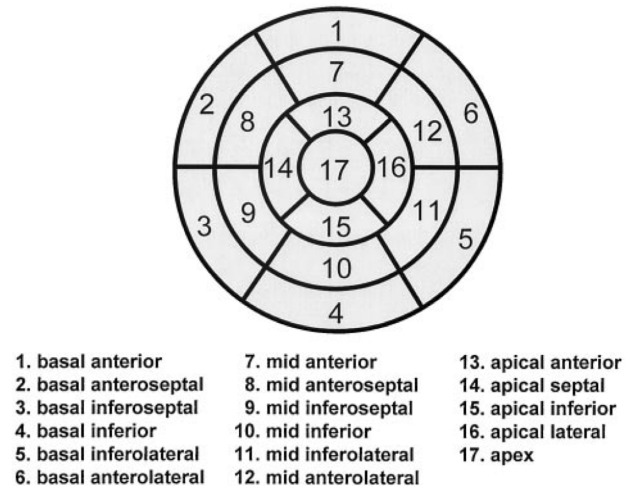


Figure 2.5: 17 myocardial segments and the recommended nomenclature [4]

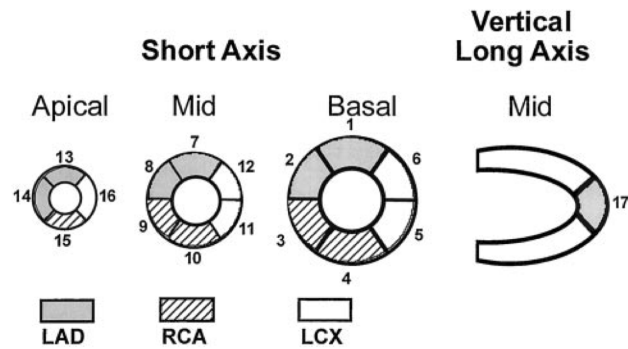


Figure 2.6: Orientation of major cardiac planes with respect to heart and their corresponding appearance [4]

### 2.5 Cardiac MRI

Cardiac MRI is a widely used imaging modality. Cardiac MRI is used to assess function and structure of the cardiovascular system. Cardiac MRI is also based on nuclear medicine principles and has been optimized to assess cardiovascular system. Even though, there are a number of imaging techniques used in cardiac MRI, this section has introduced tagged, cine and LGE CMR since those are within the scope of this thesis. The corresponding Tagged, Cine and LGE CMR images of a selected patient can be shown as in Figure 2.7.

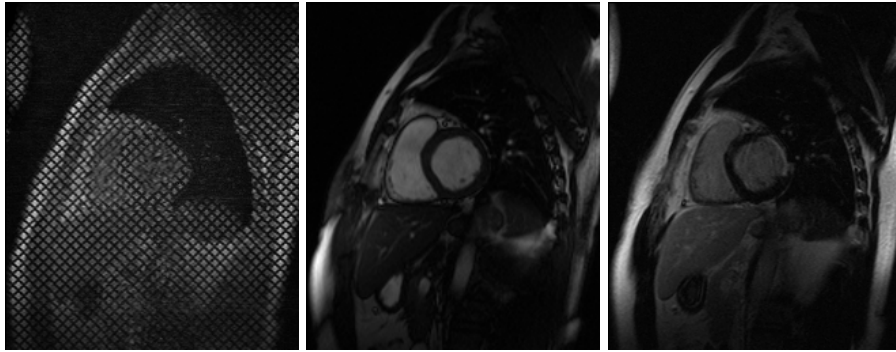


Figure 2.7: Corresponding tagged (left), cine (middle) and LGE (right) SA images obtained from a mid SA slice

#### 2.5.1 Tagged CMR

Analysis of the cardiac deformation (heart wall motion of Left and Right ventricular) is a widely used technique in identifying many types of cardiovascular diseases. Early efforts for analyzing ventricular wall motion used surgical implantation and tracking of radiopaque markers with X-ray imaging in canine hearts. In order to avoid this time consuming and risky invasive heart wall motion analysis, MR

tagging (Tagged MRI) was first proposed by [21] and [22] as a noninvasive motion tracking method of heart walls. Using this technology [21] and [22] introduced noninvasive markers directly into the tissue during the image acquisition process as magnetization pattern that remains persistent even in the presence of motion through cardiac cycle. However, tag lines fade due to  $T_1$  relaxation of magnetization as can be seen in Figure 2.8. Tagged images are obtained with ECG triggered segmented imaging where cardiac cycle is divided into multiple segments (frames) to produce a series of images that can be displayed as a movie (cine). The cardiac cycle begins with the  $R$  wave of the ECG, ends with the subsequent  $R$  wave and is typically divided into 10 to 20 segments, depending on the heart rate. In order to create this tagged image sequence requires multiple heartbeats with a single breath hold to create full image sequence in a single slice (plane). Hence, tagged CMR needs longer time than cine CMR and due to this reason, the number of frames in a tagged CMR sequence is fewer than a corresponding cine CMR sequence, even though the quality of image is similar.

The most widely used tagging patterns include SPAMM (Spatial modulation of Magnetization) introduced by [22] and CSPAMM (Complementary Spatial modulation of Magnetization ) introduced by [23]. Both of these methods result in a light and dark pattern in images due to using a special pulse sequence to spatially modulate the longitudinal magnetization, prior to image acquisition using conventional imaging [10]. CSPAMM tagging has longer tag persistence than SPAMM. With the artificial markers embedded into the tissues, it is possible to assess cardiac motion qualitatively by visualizing the tag pattern evolution throughout the cardiac function. However, to avoid erroneous human analysis of such patterns and to avoid high time consuming, new image processing and analysis methods

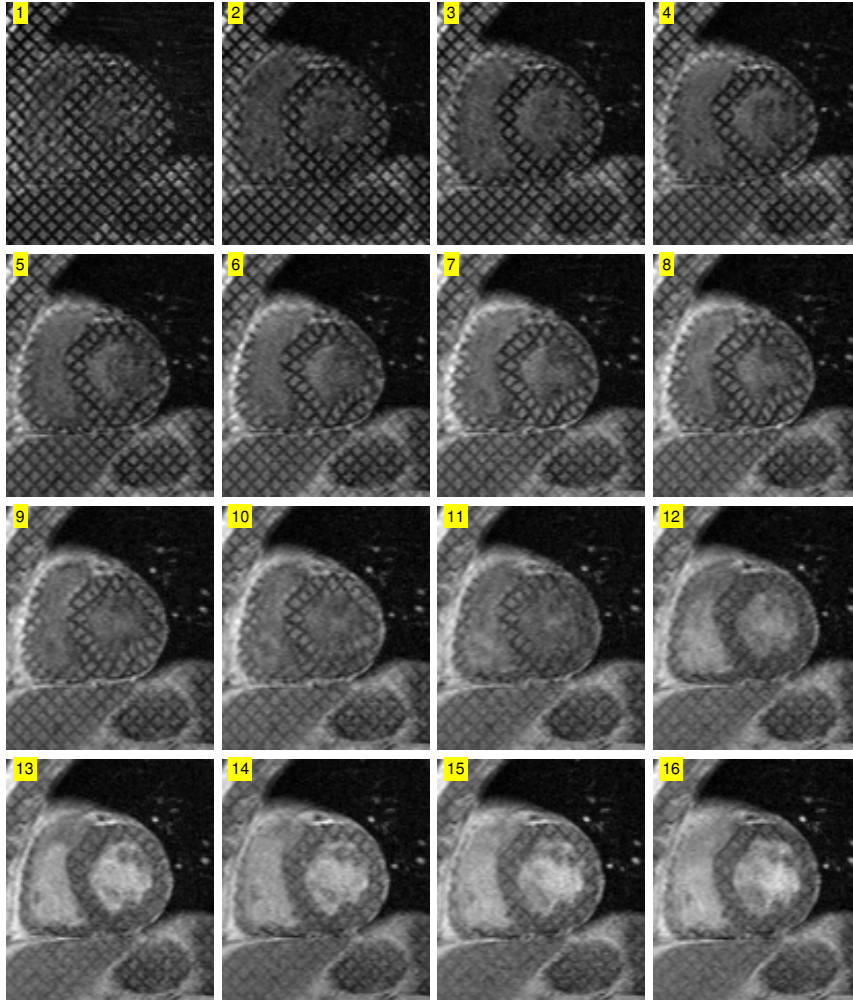


Figure 2.8: First 20/16 frames of a SPAMM tagged basal SA slice. Frame numbers are indicated at top left corner of each image

emerged to cope with automatic analysis of these tagged CMR images. More over, 3D automatic cardiac analysis methods emerged which make use multiple SA and LA image slices along with 3D tagging.

### 2.5.2 Cine CMR

Cine images are a series of images or movie, which shows heart motion throughout the cardiac cycle. Cine images are obtained with ECG triggered segmented imaging where cardiac cycle is divided into multiple segments (frames) to produce a series of images that can be displayed as a movie (cine). The cardiac cycle begins with the R wave of the ECG, ends with the subsequent R wave and is typically divided into 10 to 20 segments, depending on the heart rate [24]. This cine image sequence is obtained with a breath-hold of 10 to 20 seconds and the resulting images may be gathered over several heart beats[24].

A cine CMR sequence is carrying both functional and anatomical information. Hence, cine CMR is used as gold standard for quantifying global heart function in measuring ejection fraction, cavity volume and mass. Cine CMR has a high soft tissue contrast and due to its high soft tissue contrast, cine CMR can also be used to derive anatomical information. Moreover, cardiac wall motion tracking is also possible with cine CMR since it provides a relatively high temporal resolution. In these cine CMR images, the myocardium is shown as dark regions and blood is shown as brighter regions. Figure 2.9 shows the first 16/20 frames of a typical SA slice.

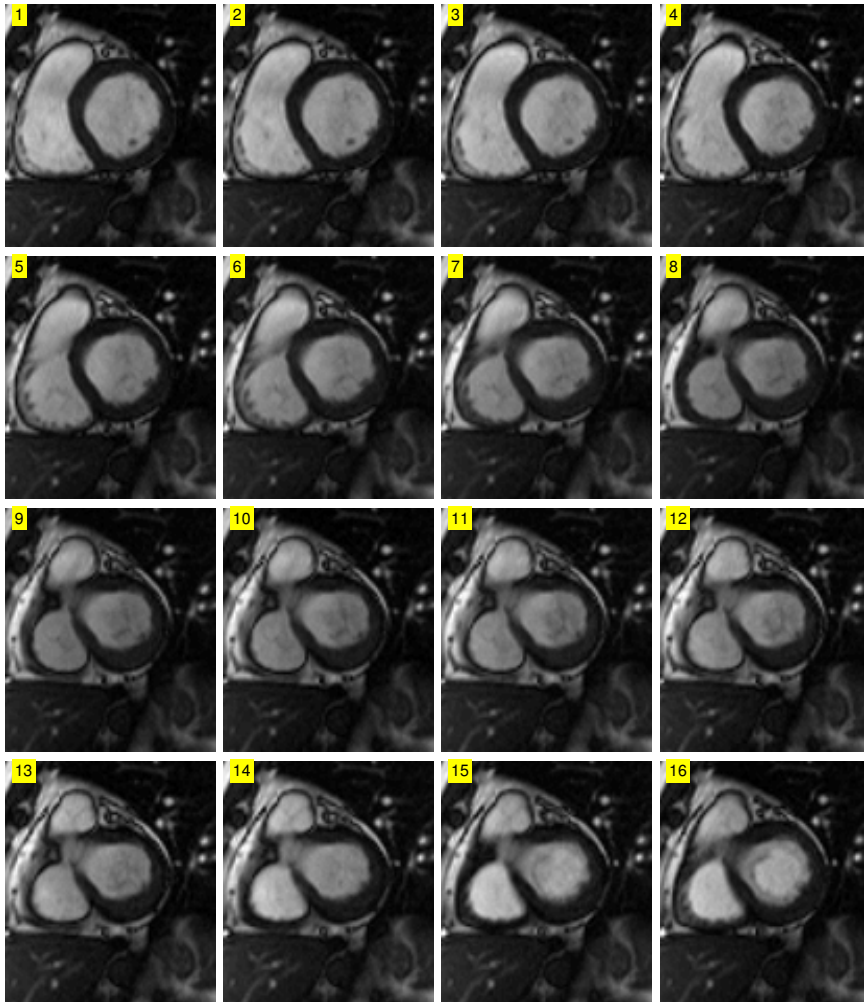


Figure 2.9: First 16 of 20 frames of a basal cine SA slice. Frame numbers are indicated at top left corner of each image

### 2.5.3 LGE CMR

Late Gadolinium Enhancement imaging is used in viability assessment of the myocardium. Imaging is performed 10 to 20 min after contrast agent (gadolinium-based) application to produce LGE images which depict diseased myocardium with excellent reproducibility. LGE CMR is capable of detecting advanced ischemic heart disease conditions while distinguishing from nonischemic dilated cardiomyopathy. LGE CMR can also be used to evaluate functional recovery after revascularization procedures [25]. The Figure 2.10 shows a LGE CMR image stack derived from a real human.

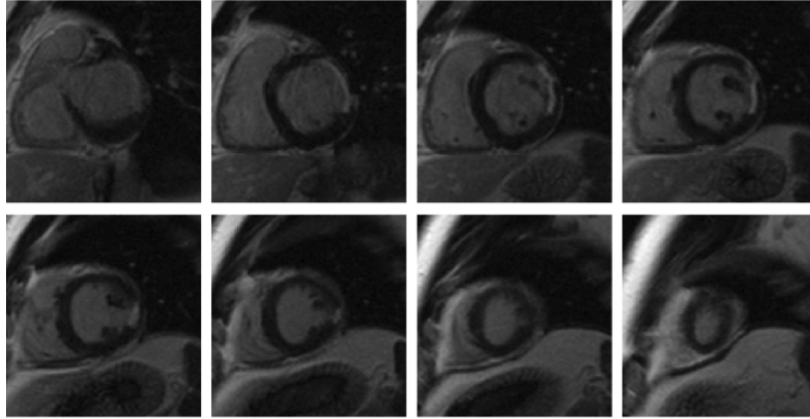


Figure 2.10: A stack of SA LGE images of a patient [5]

## 2.6 Structural and Functional Descriptors

Even though there are multiple modalities and techniques to assess cardiac function, standard measures are used to quantify the results of such assessment. These measures which represent structural and functional parameters of heart can be mainly divided into *global* and *regional* measures.

### 2.6.1 Global Functional Parameters

Global functional parameters are used to assess overall performance of the ventricles and their ability to eject blood. These measures are defined as below;

**Stroke Volume (SV)** volume ejected during systole.

$$SV = EDV - ESV \quad (B.1)$$

**Ejection Fraction (EF)** The ratio of the SV to the EDV as a percentage.

$$EF = \frac{SV}{EDV} \times 100 \quad (B.2)$$

**Cardiac Output (CO)** amount of blood ejected from the LV per minute and is equal to the SV multiplied by the heart rate (HR):

$$CO = SV \times HR \quad (B.3)$$

**Left Ventricular Volume (LVV)** the volume enclosed by the LV.

**Left Ventricular Mass (LVM)** LV mass defined as myocardium volume ( $V_m$ ) multiplied by its density( $\rho_m$ ).

$$LVM = V_m \rho_m \quad (B.4)$$

However, global measures are not sufficient to assess cardiac function. Specially, global measures cannot detect sub-clinical anomalies or the localize abnormal re-



gions [26], [20]. Moreover, global functional parameters fall within normal limits even though the wall motion is abnormal[9]. Hence, regional analysis of cardiac function is important and essential for detecting ischemia.

### 2.6.2 Regional Functional Parameters

Even though, electrocardiography and cine MRI can be used to assess regional function, it is limited to analysis of wall thickening. However, the regional cardiac function can be evaluated using tagged MRI due to tagged pattern visible in myocardium throughout the cardiac function. When considering the assessment of heart motion using tagged MRI, strain is considered as one of the major parameters.

#### 2.6.2.1 Strain

The motion of the heart is usually computed as a dense or sparse displacement field. If it is a sparse displacement field an interpolation is done to get the dense displacement field. This dense displacement field is used to calculate strain tensors which describe the function of the heart.

From the displacement field, both lagrangian and eulerian strains can be calculated. The circumferential, radial and longitudinal strains are lagrangian strains and these strains are defined with respect to the myocardium center. In addition to the lagrangian strains, this thesis has incorporated regional eulerian strains in XX, XY, and YY directions to have a more detailed analysis. Finally, these regional strains are calculated according to standard myocardium segmentation as shown in Figure 2.5.

In Figure 2.11, normal strains (dark solid arrows) are described with respect to the short axis plane:  $E_{CC}$  represents circumferential shortening tangential to epicardial surface,  $E_{RR}$  represents myocardial thickening radially towards the center of the ventricle and  $E_{LL}$  represents basal to apical shortening along the ventricular long axis [6]. These three measures indicated in Figure 2.11, are used to calculate circumferential, radial and longitudinal strains consecutively. However, longitudinal strain is out of the scope of this thesis.

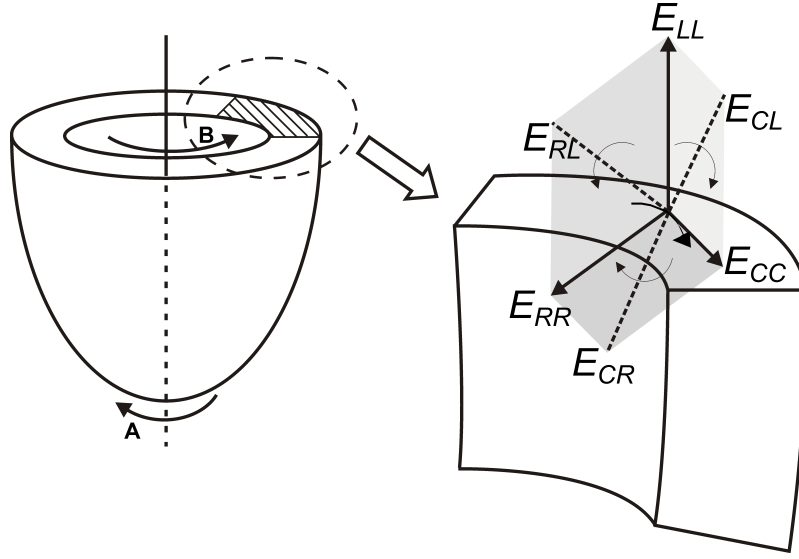


Figure 2.11: Schematic diagram demonstrating the three dimensional circumferential - radial - longitudinal (RCL) coordinate system used for strain calculation [6]

### 2.6.2.2 Apico-basal Twist (Torsion)

Left ventricular (LV) twist or torsion is used as another parameter to assess cardiac function and it represents the mean longitudinal gradient of the net difference in clockwise and counterclockwise rotation of the LV apex and base, as viewed

from LV apex [27]. Due to the torsion in the LV, oxygen demand during systole and transmural myocardial strain is reduced. When muscle cells die, systolic LV torsional deformation is delayed and decreased, impairing the beneficial effects of torsional deformation [9], [27]. However, myocardial torsion is out of this thesis scope and has not taken into account for the analysis.

### 2.6.3 Infarct Quantification

The Late gadolinium enhanced (LGE) imaging protocol can be used to assess ischemia due to myocardial infarction directly. This viability assessment of myocardium is done either directly visualizing or quantifying infarct region. Specially, quantifying and localizing infarcted tissue (infarct/ infarction/ scar) is important for diagnosis, planing and evaluation of treatments.

In order to quantify infarction, infarct transmurality and absolute infarct area / volume / mass are usually taken into account [28], [29]. Specially, the percentage of the infarcts with respect to the entire myocardium (thereafter denoted by I/M%) is intuitively used by cardiologists to reflect the extent and severity of infarction [30], [5].

$$I/M\% = \frac{\text{Size of the infarcts}}{\text{Total size of the myocardium}} \quad (\text{B.5})$$

In this thesis, I/M% is used as quantitative index of myocardial infarction since it is independent of variable individual heart size compared to the absolute infarct measurements such as area, volume and mass.

In order to segments, localize and quantify the infarction and I/M% from LGE data, this thesis has adapted the 3D graph-cut algorithm proposed by [5], [30]. Moreover, infarctions have localized and I/M% has been calculated according to

standard myocardium segmentation proposed by [4]. The Figure 2.12 shows infarct percentage calculated according to standard myocardium segmentation (apex is not considered).

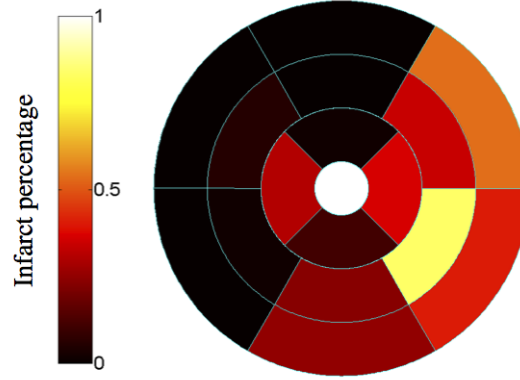


Figure 2.12: Bull's eye plot of a myocardium which shows I/M% in standard 16 segments [5]

## 2.7 Cardiac Motion Estimation Methods

Using the MR tagging method introduced by [21], cardiologists, surgeons and doctors could analyze the heart wall motion by looking at apparent motion in tagged MRI image frames. However, human analysis of such patterns caused erroneous results. It is also highly time consuming and expert knowledge is essential in this process. As a solution for these issues, with the development of cardiac MRI and other cardiac imaging modalities, new image processing techniques for rapid analysis of images sequences were emerged. These image analysis lead to recover cardiac wall motion and compute measures like strain and ejection fraction in order to assess cardiac function. However, due to inherent issues of these cardiac image

sequences (noise, fading, resolution issues and so on), accurate motion recovery has been a challenging task.

In recent times, MRI tagging has seen increased applications and is becoming the gold standard for quantifying regional function [10]. However, it can be seen that similar techniques have been applied to both tagged and cine CMR in order to recover motion. Cardiac motion analysis methods can be divided in to two categories as follows:

- Feature based motion estimation techniques
- Direct motion estimation techniques

After applying a feature based or direct motion estimation technique, the interpolation method may apply if the motion field is sparse. These interpolation methods include; B-Splines, Thin plate Spline, Finite Element method, parametric functions and so on. Moreover, based on the dense or sparse displacement field, the strain measures are calculated. An abstract hierarchical computational model of cardiac motion estimation techniques can be illustrated as in Figure 2.13. A comprehensive review about cardiac motion estimation methods can be found in [10]. This section briefly describes the main tagged CMR based cardiac motion estimation methods while giving more focus to optical flow based methods.

### 2.7.1 Feature Based Motion Estimation

#### 2.7.1.1 Tracking Land marks

Feature based motion estimation methods are based on tracking one or more selected features through out a MR image sequence. Most of such features include

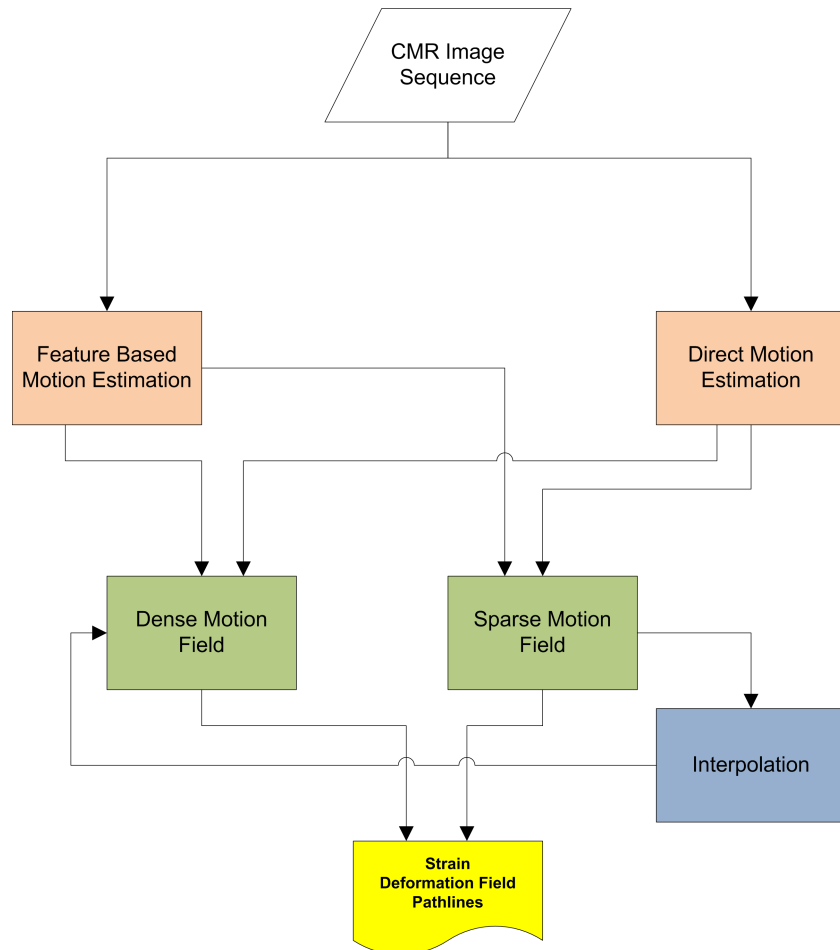


Figure 2.13: Abstract hierarchical computational model of cardiac motion estimation techniques

sparse taglines, landmarks, tag intersections and epi/endo cardial contours. Myocardial beads which are defined as the intersection points of orthogonal tagging planes, can be used as noninvasive markers [31]. These intersections encode a unique 3D position in the myocardium which move along with the deforming tissue during the cardiac cycle helps to estimate the motion accordingly. However, to track the true 3D motion, myocardial beads need to be reconstructed or extracted by considering tag planes and tag lines. The parametric representation of the tag surfaces using models like B-Spline [31], thin-plate [32] provides an easier way of computing the position of 3D myocardial beads by minimizing the summation of distances between any two reconstructed tag surfaces. Further, [33] proposed an automatic 3D cardiac beads tracking method using 2D HARP tracking. [34].

### 2.7.1.2 Deformable Models

In the deformable modeling approach, a model deforms to fit the data using energy minimization or based on classical physics-based equation of motion [35]. The constraints on these models vary with applications. Tag intersections, tag lines, or tag surfaces like features are used to drive the deformation. However, due to the sparsity of feature information, vector field interpolation techniques are applied to obtain a dense motion field. These interpolation methods include: mathematical regularization [36], Finite Element Method [37], Boundary Element Method [38], parameter functions based deformable methods [39], B-splines [31]. However, these methods assume extracted tags and myocardial contours in order to produce deformation analysis.

The accuracy of feature-based image analysis methods using tagged CMR depends highly on the quality of the image and the spacing of tag lines. Tagged MR

images with higher spatial resolution will provide more information and constraints on the models [10].

### 2.7.2 Direct Motion Estimation

#### 2.7.2.1 Harmonic Phase MRI (HARP)

HARP can be considered as the most widely referred rapid cardiac motion analysis method since it was introduced by [34], [40] and [41]. In HARP tracking, harmonic phase image is derived by isolated spectral peaks in SPAMM tagged CMR images and material points are tracked based on the fact that phase of a material point remains constant as it moves during the cardiac cycle. Hence, unique phase of a particular point can be tracked along the cardiac cycle and estimate the displacement field. Even though, HARP is a fast and automatic that does not need any preprocessing, it can fail in the presence of a large amount of motion. However, various enhancements to this method can be found in literature, as it is the most widely referred method. Moreover, the phase wrapping function in HARP methods become problematic with increasing noise in tagged CMR sequence.

#### 2.7.2.2 Local Sine Wave Modeling(SinMod)

SinMod [42] is also a phase based motion estimation method which is similar to HARP. However, SinMod is different from HARP since it detects both local spatial phase shift and local spatial frequency from band-pass filtered images while HARP assumes phase invariant condition to track and estimate [10].



### 2.7.2.3 Gabor Filter Banks

Gabor filter is a band-pass filter. This filter takes the form of a Gaussian multiplied by a complex sinusoid in the spatial domain. It can also be obtained by a shifted Gaussian in the spatial frequency domain. Gabor filters are used in computer vision community for edge detection and it is said that frequency and orientation representations of Gabor filters are similar to those of the human visual system [43]. By choosing appropriate and optimized parameters from a gabor filter banks, relevant magnitude response of the Gabor filter can be used to remove tags and the phase response can be used to track tags. Once the tags lines, tag intersections or material points are tracked, interpolation methods can be applied to get a dense motion field [44], [45],[46], [47]. However, HARP and Gabor filter based methods require an unwrapping step, which is an error prone process prevents giving an accurate motion estimate over full cardiac cycle. In order to prevent these issues, [45] have proposed a slightly different approach. In [45], a gabor filter bank is used to detect tag intersections over the image sequence and then the tag intersection points is followed by robust point matching (RPM) and meshless deformable model to track 3D motion.

### 2.7.2.4 Registration-Based Methods

Estimating motion between two CMR images can be modeled as an image registration problem. Registration process finds the optimal transformation that can transform one image to the other, maximizing a similarity metric between two images. Image registration has been used in both tagged and cine CMR in order to estimate cardiac motion [48], [49]. Image registration can also be considered as

a widely used method to track cardiac motion due to its advantages. With image registration, tag detection/extraction or segmentation steps are not required and the algorithm allows motion tracking to be fully automatic. However, these methods may get stuck in local minima while tend to have potential misalignment due to image noise and artifacts. Moreover, the computational time is longer than other methods like HARP [10].

### 2.7.2.5 Optical Flow Based Methods

In general, 3D motion appeared in a 2D image motion, and resulting 2-D motion estimation problem is cast as the problem of estimating the time-varying derivatives of the image brightness pattern, usually called optical flow. The optical flow approximates the motion field based on a few assumptions. These assumptions include:

- No photometric distortion
- No occlusion problem occurs
- Lambertian surfaces
- Point-wise light sources at infinity

The optical flow estimations are usually divided in to three categories as follows:

#### Differential Techniques:

The differential methods estimate optical flow vectors from the derivatives of image intensity over space and time. These are typically derived directly by considering the total temporal derivative of a preserved quantity such as the brightness.

### Matching Techniques:

These methods operate by matching small regions of image intensity or specific features from one frame to the next. The matching criterion is usually a least squares or normalized correlation measure.

### Frequency or Filter Based Techniques:

In these methods, motion problem is addressed in the Fourier domain. Spatio-temporally oriented filters are used to derive velocity sensitive data which are related to motion. These methods can be categorized as either energy-based or phase-based in terms of the analysis method.

However, in general, a good solution still remains elusive in challenging situations such as occlusions, motion boundaries, texture-less regions, and/or large displacement motions. Each of above mentioned optical flow estimation method has its own advantages and disadvantages.

Methods based on optical flow have also been applied to the analysis of tagged MR images. By using optical flow in cardiac motion estimation context, tag detection/extraction or segmentation steps are not required and the algorithm allows the motion tracking to be fully automatic similar to image registration methods. In general, optical flow methods are relatively faster than image registration methods.

However, the general the brightness consistency assumption made to derive optical flow gives erroneous results due to obvious tag fading effect in tagged CMR.

In order to deal with tag fading and to have an accurate optical flow estimation [50] introduced an approach called *Variable Brightness Optical Flow (VBOF)* which accounts for temporal variation of signal intensities. The algorithm de-

scribed in VBOF basically does not make the brightness consistency assumption. Instead, it included tag pulse sequence parameters such as  $D_0$  is the spin density,  $T_1$  is longitudinal relaxation time,  $T_2$  is the transverse relaxation time,  $T_E$  is the echo time, and the cosine of the magnetization tip angle needed to produce the tag pattern. By using prior knowledge of these parameters, the VBOF method modeled the tagged pattern generation process in order to avoid the erroneous result. However, the need of this prior knowledge in VBOF method is a major limitation of the method.

The Gennert and Neghadirapour's optical flow (GNOF) method [51] relaxes the intensity constancy constraint by modeling the intensity variations or the noise as a local linear transformation. Moreover, [52] made the VBOF algorithm more practical by using MR imaging physics to derive approximations for brightness variations. In this enhanced VBOF method  $T_1$  relaxation is used as the only prior knowledge to estimate the optical flow.

In the method proposed by [53], an additional preprocessing step of the images has been followed using a Laplacian filter which eliminates any local offset field and enhances the edges in the image (by compensating intensity and contrast loss in myocardial tags). Therefore, [53] has proposed a method that enhance tagged CMR images prior to calculate optical flow.

In addition to above optical flow methods, phase based optical flow methods have also been used to estimate myocardial motion [54], [10]. In the method proposed in *Band pass optical flow* [55] [56], Fourier space information in tagged images is used to extract various sub band images by filtering out relevant portions of frequency space. After that, optical flow constraint equations are then formulated for each of tagged MR images based on sub band images. Further,

[57] extended the phase consistency information into a multiresolution framework, while yielding a dense, smooth and robust estimation. Alternatively, [58] used both phase based information and intensity based information to derive the optical flow. In [58], the variational optical flow method has been improved by adding a new term in the optical flow equation that incorporates tracking points with high stability of phase. Moreover, [58] used a variational integrals based regularization method to improve noise robustness.

When considering the optical flow based cardiac motion estimation methods, it can be seen that available methods tend to reduce the effect of error due to tag fading. The inevitable tag fading effect in tagged CMR is the main reason for trying to reduce the tag fading error. In order to minimize or avoid this error, these methods have followed the strategies such as modeling error term, using filtering techniques, using phase information and so on. Alternatively, this thesis suggests estimating optical flow jointly by using both cine and tagged CMR data simultaneously. Moreover, the proposed method in this thesis uses cine CMR optical flow data as a prior to estimate final tagged CMR optical flow. Further, the proposed method is motivated to use a gradient-based optical flow technique due to the fact that it is well suited for processing tagged CMR images. Further, tagging produces the spatial brightness gradients on which the brightness constraint equation depends [59] and best results from gradient based methods are obtained using two orthogonal SPAMM tagged images [59]. In addition, gradient-based optical flow methods are relatively fast in computation and it gives a dense motion field. In this thesis, [60] method has been taken as the basis since the window size in which the motion is assumed to be consistent, can be used to prevent or threshold the erroneous optical flow estimations. In addition, this motion consistency assump-

tion is more realistic on heart wall motion context where the complex motions of multiple objects and occlusions do not appear like in real world.

### 2.7.3 Joint Motion Estimation Methods

When considering the joint cardiac motion estimation methods using both tagged and cine CMR data, [61] is the only method available according to the best of our knowledge. In [61] a nonrigid image registration was introduced for myocardial motion estimation using both cine (Untagged) and 3-D tagged MR images. The method proposed in [61] used complementary information from both cine and 3-D tagged CMR images simultaneous to estimate the motion within the myocardium. Moreover, [61] register a sequence of tagged and cine CMR images during the cardiac cycle to a set of reference tagged and cine CMR images at end-diastole. In [61], it has been proposed a spatially adaptive weighting to help extract complementary information from both tagged and Cine CMR images.

The method introduced by [61] and the method proposed by this thesis is closely related. Both of these methods have used rich anatomical information in cine CMR images to compensate for problems arising with tag fading in the tagged CMR images over the cardiac cycle. However, this thesis presents an optical flow based solution while [61] is using an image registration based solution. In addition, [61] computed 3D strains while this thesis focuses on 2D strain.

## 2.8 Validation of Cardiac Motion Estimation Methods

Validation of cardiac motion estimation methods is a challenging task. There exists no gold standard validation method in order to validate cardiac motion methods. The following methods can be mentioned as the main validation methods that are used by the community.

**Validation with a cardiac motion simulator** One of the most widely used cardiac motion simulators is the simulator proposed by [62] based on 13-parameter model of LV motion introduced by [63]. The [62] method simulates the tagged CMR imaging process using a standard (tagged) spin-echo imaging equation while applying prolate spherical based known LV motion. Moreover, the known motion can be used to validate the method and image sequences can be synthesized at arbitrary orientations at any phase using [62]. The [62] method is useful specially in validating 3D motion estimation methods. However, the disadvantage of this approach is that difficulties encountered in clinical practice has not taken into account [9] and the tag fading is not realistic as in tagged CMR.

**Validation with a numerical phantom** The numerical phantoms are also used widely in validating cardiac motion estimation algorithms [64], [58],[65], [50]. The numerical phantoms are simpler to generate than simulators. Numerical phantoms can be used to simulate tag fading effect in tagged CMR better than in simulators. Moreover, these phantoms are deformed according to a known motion field and further use this motion field as the ground

truth. The numerical phantoms do not require making any assumption on the imaging process and these phantoms are mostly used in validating 2D motion estimation algorithms.

**Validation with manually tracked points** Obtaining ground truth data from real cardiac CMR images by manually tracking the motion of the myocardium is another method for validating cardiac motion estimation algorithms [66]. Usually graphical tools are incorporated in order to make the points tracking more accurate and easier. The main advantage of this method is that it is operating on real CMR data rather than synthetic CMR data. However, tracking points is a time consuming task that needs careful attention. In addition to that, no ground truth for functional descriptors such as strain can be obtained in this way[9] while simulators and phantoms provide ground truth for both motion and strain.

The methods described above are mainly applied into tagged CMR images. However, due to the limited number of methods proposed which are jointly estimating with both tagged and cine CMR data, this thesis proposes a slightly different numerical phantom from the numerical phantoms used in [64], [58],[65]. Specially, in addition to tagged CMR phantom, the corresponding cine CMR phantom is also generated in order to validate the proposed algorithm in this thesis.



## Chapter 3

# Joint Motion Estimation Using Cine and Tagged CMR

This chapter describes the proposed new approach for motion estimation using both tagged CMR and cine CMR sequences. The proposed method is jointly estimating the strain from left ventricle myocardial motion using a optical flow method. The proposed method aims to take the advantage of two imaging modalities that represent same motion of a particular patient. The method is validated using synthetic and real data from tagged and cine CMR image sequences.

### 3.1 Overview

In order to estimate cardiac motion, several steps need to be followed as shown in Figure 3.1. Firstly, the tagged and cine CMR sequences need to be aligned spatially and temporally in order to estimate the motion in a common reference frame. This thesis assumes that both cine and tagged slice pairs are obtained from

same patient location and orientation. However, it has been taken into account that spatial resolution of tagged and cine image sequences may differ during the image acquisition process.

Once the tagged and cine image sequences relevant to a particular slice are aligned, the endocardial and epicardial contours of first frame of each slice are obtained for segmenting the myocardium. Further, the myocardium of each slice further segmented into standard AHA segmentation as described in [4].

After myocardium segmentation, motion is estimated between each frames of a particular slice and whole slices are processed in order to get data relevant to a particular patient. Moreover, the strain tensors are calculated from motion obtained from each frame pairs and these strain tensors are used to calculate the AHA segment wise lagrangian (radial and circumferential) and eulerian strains (XX, XY and YY direction) measures.

## 3.2 Spatial and Temporal Alignment of Tagged and Cine Images

The analysis of cardiac motion information from different images requires a common spatial and temporal reference space. However, this is a challenging task due to differences in image acquisition for the different images. There are three major difficulties; 1) the anatomy is not clearly visible due to the presence of tag lines, 2) respiratory and patient motion within sequences and across sequences, and 3) temporal resolution of different image sequences is vary [61].

In [5] proposed a registration algorithm to correct the spatial misalignment

### 3. Joint Motion Estimation Using Cine and Tagged CMR

---

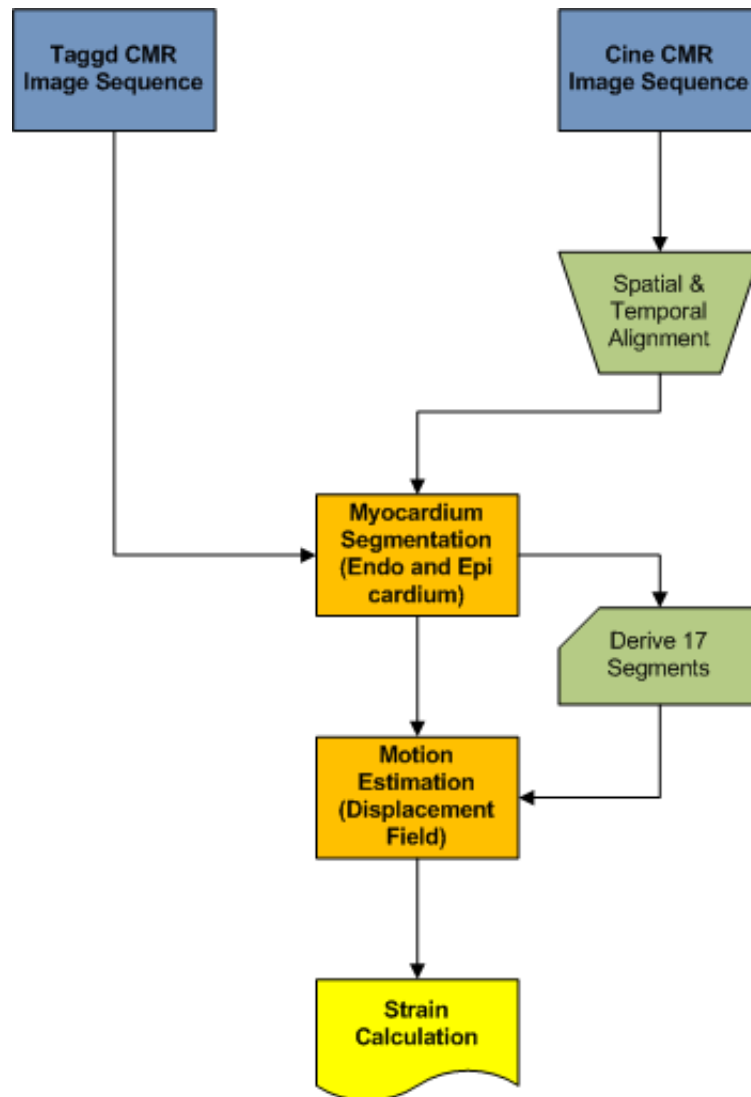


Figure 3.1: The hierarchical computational process of cardiac motion estimation

between cine and LGE images. This thesis uses the method proposed by [5] in order to align tagged and cine CMR image sequences. However, in this thesis temporal alignment has not been performed and has assumed that phases in which the tagged and cine image sequences obtained are equal approximately.

## 3.3 Segmentation of Myocardium

In order to derive myocardial contours, this thesis has adapted the method used in [5]. In [5], cine contours are used as a prior knowledge to segment LGE images via a 2D translational registration. Two meshes representing respectively endocardial and epicardial surfaces are then constructed with the propagated contours. After construction, the two meshes are deformed towards the myocardial edge points detected in both SA and LA LGE images in a unified 3D coordinate system[5]. In this thesis, the same procedure is followed to segment endocardial and epicardial contours in tagged CMR images by considering cine CMR images.

## 3.4 Algorithm Development

Optical flow is often a convenient and useful in image motion representation. Optical flow based techniques have been applied to estimate motion in Cardiac MR sequences in order to estimate the myocardial displacement. Once having the displacement field the related strain measures can be computed. Each optical flow estimation technique has several advantages and disadvantages. However, the main advantage of the optical flow methods is that they provide a dense estimation of the motion field in two dimensions rather than just a sparse set of data, and

### 3. Joint Motion Estimation Using Cine and Tagged CMR

---

they do not require a prior segmentation of myocardium [58].

Intensity based optical flow methods are widely used to compute vector fields from spatio temporal derivatives given by an image sequence. [67] and [60] can be considered as the most popular methods among them. The basic assumption common in both these methods is that the intensity of a particular point does not change over a short period of time. Suppose,  $(u, v)$  are the  $x$  and  $y$  components of optical flow and  $(I_x, I_y, I_t)$  are intensity derivatives. Based on this intensity/brightness consistency assumption the 2D motion constraint equation is derived as in Equation C.1.

$$I_x u + I_y v + I_t = 0 \quad (\text{C.1})$$

In the method proposed by [60] method, it assumes additionally that the displacement of the image contents between two nearby instants (frames) is small and approximately constant within a neighborhood of the point  $p$  under consideration. Hence, [60] assumes that motion within a small window of size  $\sqrt{n} \times \sqrt{n}$  pixels is equal. Bases on these assumptions, optical flow equations for the  $\sqrt{n} \times \sqrt{n}$  pixels can be written as in Equation C.2.

$$\begin{aligned} I_x(q_1)u + I_y(q_1)v &= -I_t \\ I_x(q_2)u + I_y(q_2)v &= -I_t \\ &\vdots \\ &\vdots \\ &\vdots \\ I_x(q_n)u + I_y(q_n)v &= -I_t \end{aligned} \quad (\text{C.2})$$

### 3. Joint Motion Estimation Using Cine and Tagged CMR

---

where  $q_1, q_2, \dots, q_n$  are the pixels inside the window surrounding point  $(x, y)$ , and  $I_x(q_i), I_y(q_i), I_t(q_i)$  are the partial derivatives of the image  $I$  with respect to  $x, y$  and time  $t$ , evaluated at the point  $q_i$  at the current time. The Equation C.2 can be written in matrix form  $A\tilde{x} = b$ , where

$$A = \begin{bmatrix} I_x(q_1) & I_y(q_1) \\ I_x(q_2) & I_y(q_2) \\ \vdots & \vdots \\ I_x(q_n) & I_y(q_n) \end{bmatrix}, \quad \tilde{x} = \begin{bmatrix} u \\ v \end{bmatrix}, \quad \text{and} \quad b = \begin{bmatrix} -I_t(q_1) \\ -I_t(q_2) \\ \vdots \\ -I_t(q_n) \end{bmatrix}$$

This system has more equations than unknowns. Thus it is an over-determined linear system and can be solved using least squares method.

In order to estimate optical flow (motion) from tagged CMR and cine CMR, the proposed method is basically followed [60] method. Moreover, [60] is less sensitive to image noise and computationally efficient.

Lets assume that we have two pair of Tagged and Cine CMR images which represent the same cardiac motion of a particular patient and each image pair has been taken in similar cardiac phases.  $(I_{t=t1}^{\text{cine}}, I_{t=t1}^{\text{tagged}})$  and  $(I_{t=t1+1}^{\text{cine}}, I_{t=t1+1}^{\text{tagged}})$ . According to optical flow Equation C.1, we can derive Equation C.3, Equation C.4 for a particular point  $(x, y)$  of each tagged and cine CMR image pair which undergoes same motion  $(u, v)$ .

### 3. Joint Motion Estimation Using Cine and Tagged CMR

---

$$(I_x^{\text{cine}})u + (I_y^{\text{cine}})v + (I_t^{\text{cine}}) = 0 \quad (\text{C.3})$$

$$(I_x^{\text{tagged}})u + (I_y^{\text{tagged}})v + (I_t^{\text{tagged}}) = 0 \quad (\text{C.4})$$

If we take a  $\sqrt{n} \times \sqrt{n}$  window in cine CMR image which surrounds point  $(x, y)$ , we can write down the system of equations as follows and it can be written in matrix form as in Equation C.5.

$$A^{\text{cine}} = \begin{bmatrix} I_x^{\text{cine}}(q_1) & I_y^{\text{cine}}(q_1) \\ I_x^{\text{cine}}(q_2) & I_y^{\text{cine}}(q_2) \\ \vdots & \vdots \\ I_x^{\text{cine}}(q_n) & I_y^{\text{cine}}(q_n) \end{bmatrix}, \quad \tilde{x} = \begin{bmatrix} u \\ v \end{bmatrix}, \quad \text{and} \quad b^{\text{cine}} = \begin{bmatrix} -I_t^{\text{cine}}(q_1) \\ -I_t^{\text{cine}}(q_2) \\ \vdots \\ -I_t^{\text{cine}}(q_n) \end{bmatrix}$$

$$A^{\text{cine}}\tilde{x} = b^{\text{cine}} \quad (\text{C.5})$$

Again, If we consider a  $\sqrt{m} \times \sqrt{m}$  window in tagged CMR image which surrounds point  $(x, y)$ , we can write down the system of equations as follows and it can be written in matrix form as in C.6.

### 3. Joint Motion Estimation Using Cine and Tagged CMR

---

$$A^{\text{tagged}} = \begin{bmatrix} I_x^{\text{tagged}}(r_1) & I_y^{\text{tagged}}(r_1) \\ I_x^{\text{tagged}}(r_2) & I_y^{\text{tagged}}(r_2) \\ \vdots & \vdots \\ I_x^{\text{tagged}}(r_m) & I_y^{\text{tagged}}(r_m) \end{bmatrix}, \quad \tilde{x} = \begin{bmatrix} u \\ v \end{bmatrix}, \quad b^{\text{tagged}} = \begin{bmatrix} -I_t^{\text{tagged}}(r_1) \\ -I_t^{\text{tagged}}(r_2) \\ \vdots \\ -I_t^{\text{tagged}}(r_m) \end{bmatrix}$$

$$A^{\text{tagged}} \tilde{x} = b^{\text{tagged}} \quad (\text{C.6})$$

Since Equation C.5 and Equation C.6 represent same motion, we can get the Equation C.7 as follows;

$$A^{\text{combined}} \tilde{x} = b^{\text{combined}} \quad (\text{C.7})$$

Where;

$$A^{\text{combined}} = \begin{bmatrix} A^{\text{cine}} \\ - \\ A^{\text{tagged}} \end{bmatrix}, \quad \tilde{x} = \begin{bmatrix} u \\ v \end{bmatrix}, \quad b^{\text{combined}} = \begin{bmatrix} b^{\text{cine}} \\ - \\ b^{\text{tagged}} \end{bmatrix}$$

Again Equation C.7 can be considered as an over determined linear system and can be solved for  $(u, v)$  using Least Squares Estimation. However, the intensity constancy condition is not satisfied in CMR image sequences due to the relaxation of the magnetization of the spins throughout the cardiac cycle. In addition, the differential optical flow methods have a major drawback in the estimation of the first and second derivatives of pixel intensity, mainly in the case of noisy images. Hence, to have an accurate solution for Equation C.7, noise also need to be considered.



In order to solve over-determined linear system in Equation C.7, **Recursive Least-Squares Estimation (RLSE)** method has been used. RLSE method can be considered as a recursive method to compute the Least-Squares Estimation based solutions [68].

#### 3.4.1 Recursive Least-Squares Estimation(RLSE)

Suppose we get first  $k$  entries in  $A^{\text{combined}}(1 : k, :) = A_k$  and  $b^{\text{combined}}(1 : k, :) = b_k$ . By considering first  $k$  elements, over-determined case dealt with in the Equation C.7 can be formulated as an LSE problem which is restricted to first  $k$  entries of the Equation C.7 as in Equation C.8.

$$A_k x_k = b_k \tag{C.8}$$

where;

$$A_k = A^{\text{combined}}(1 : k, :), b_k = b^{\text{combined}}(1 : k, :)$$

Further, we can apply Least-Squares to Equation C.8 and get the solution as,

$$x_k = [A_k^T A_k]^{-1} A_k^T b_k \tag{C.9}$$

Let  $a_{k+1}$  and  $r_{k+1}$  denote the  $(k+1)$ -th entry in  $A^{\text{combined}}$  and  $b^{\text{combined}}$ , respectively. RLSE method is basically adding the correction term based on the new data to get the new estimate rather than solving Equation C.10 for the  $(k+1)$  th entry. Hence, the  $(k+1)$ -th entry in Equation C.7, can be further derived as in

### 3. Joint Motion Estimation Using Cine and Tagged CMR

---

Equation C.11 for the inverse matrix  $P_{k+1}$ .

$$x_{k+1} = [A_{k+1}^T A_{k+1}]^{-1} A_{k+1}^T b_{k+1} \quad (\text{C.10})$$

Where;

$$A_{k+1} \begin{bmatrix} A_k \\ - \\ a_{k+1} \end{bmatrix}, \quad x_{k+1} = \begin{bmatrix} u_{k+1} \\ v_{k+1} \end{bmatrix}, \quad b_{k+1} = \begin{bmatrix} b_k \\ - \\ r_{k+1} \end{bmatrix} \quad \text{and} \quad P_k = [A_k^T A_k]^{-1}$$

$$P_{k+1} = [A_{k+1}^T A_{k+1}]^{-1} = P_k - P_k a_{k+1} [a_{k+1}^T P_k a_{k+1} + 1]^{-1} a_{k+1}^T P_k \quad (\text{C.11})$$

One of the advantages in using C.11 is that  $P_{k+1}$  can be computed without calculating matrix inverses. Now,  $x_{k+1}$  (the new  $(u, v)$  estimates of optical flow with the arrival with  $(k+1)$ -th entry) can be written as in Equation C.12 and further, it can be derived as in Equation C.13.

$$x_{k+1} = P_{k+1} A_{k+1} b_{k+1} \quad (\text{C.12})$$

$$x_{k+1} = x_k + P_{k+1} a_{k+1} (r_{k+1} - a_{k+1}^T x_k) \quad (\text{C.13})$$

In equation C.13,  $P_{k+1} a_{k+1}$  is multiplied by the error  $(r_{k+1} - a_{k+1}^T x_k)$  to make the correction term. Hence, the gain matrix  $K_{k+1}$  can be derived as in C.14 and updating rule of  $P_{k+1}$  in terms of  $K_{k+1}$  can be written as in C.15 [68].

$$K_{k+1} = P_{k+1} a_{k+1} = P_k a_{k+1} [a_{k+1}^T P_k a_{k+1} + 1]^{-1} \quad (\text{C.14})$$

### 3. Joint Motion Estimation Using Cine and Tagged CMR

---

$$P_{k+1} = P_k - K_{k+1} a_{k+1}^T P_k \quad (\text{C.15})$$

Assuming that  $(I_{t=t1}^{\text{cine}}, I_{t=t1}^{\text{tagged}})$  and  $(I_{t=t1+1}^{\text{cine}}, I_{t=t1+1}^{\text{tagged}})$  are spatially and temporarily aligned, the following procedure has been followed to solve Equation C.7 using RLSE method for each point  $(x, y)$ .

Suppose, number of rows in  $A^{\text{cine}}$  is  $p$  and number of rows in  $A^{\text{tagged}}$  is  $q$ ;

1. Define ROI surrounding the myocardium.
2. Select first  $k=50$  elements from  $A^{\text{cine}}$  and  $b^{\text{cine}}$  and initialize  $A_k$  and  $b_k$ .
3. Calculate  $x_k$  using Least-Squares Method.
4. Update  $x_{k+1}$ ,  $K_{k+1}$  and  $P_{k+1}$  for next  $(p - k)$  entries in  $A^{\text{cine}}$  iteratively.
5. Update  $x_{k+1}$ ,  $K_{k+1}$  and  $P_{k+1}$  further using next  $q$  entries in  $A^{\text{tagged}}$  and  $b^{\text{tagged}}$  iteratively.
6. Get the final  $x$  as the solution where  $x$  contains optical flow parameters  $(u, v)$  relevant to point  $(x, y)$ .

As can be seen in above procedure that calculates optical flow of a point using RLSE method, tagged CMR data is considered as the accurate modality for calculating optical flow. However, in order to estimate optical flow from tagged CMR, cine CMR data is used get a prior estimate for the optical flow in tagged CMR. The error in prior estimated optical flow from cine CMR is then reduced iteratively using tagged CMR data.

### 3.4.2 Strain Estimation

Generically, strain is the change in length per unit length. The 2-D analog of this concept is defined using the displacement gradient  $\Delta u(x, t)$ , which is given by;

$$\Delta u(x, t) = \begin{bmatrix} \frac{\partial u_x}{\partial x} & \frac{\partial u_x}{\partial y} \\ \frac{\partial u_y}{\partial x} & \frac{\partial u_y}{\partial y} \end{bmatrix}$$

Then the deformation gradient  $F$  of point  $x$  at time  $t$  is given by :

$$F(x, t) = (I - \Delta u(x, t))^{-1} \quad (\text{C.16})$$

where  $I$  is the identity matrix.

Finally, the 2-D Eulerian strain tensor is defined as;

$$E(x, t) = \Phi_n \Phi_n^\top - I \quad (\text{C.17})$$

where  $\Phi_n = F(x, t)$ .

Hence, prior to calculating each strain measure, myocardial strain tensor can be directly estimated as in Equation C.17 from the spatial derivatives of a dense displacement field  $\Phi_n$  [66].

Eulerian strains in XX, XY, YY directions can be directly obtained from the strain tensor in Equation C.17. Having calculated the strain tensor in Equation C.17, circumferential, radial and longitudinal strain can be calculated by projecting the strain tensor along a specific direction of a local coordinate system related to the anatomy of the LV [66]. In order to calculate each Lagrangian strain, the Equation C.18 can be used where  $P$  indicates unit vectors in radial, longitudinal,

circumferential directions and  $E(x, t)$  indicates strain tensor derived for point  $x$  at time  $t$  using Equation C.17.

$$Strain(x, t) = P^T \cdot E(x, t) \cdot P \quad (C.18)$$

## 3.5 Evaluation and Experiments

In order to evaluate the proposed algorithm, two types of synthetic images are used: "Method-A" and "Method-B". Method-A aims to evaluate the algorithm with the presence of both rotation and contraction in myocardium. Method-B aims to evaluate the algorithm with radial contraction occurs in consecutive images while the noise is getting increased. Moreover, the proposed method is evaluated on real CMR data.

### 3.5.1 Synthetic Data - Method A

To begin with first experiments, synthetic data is generated by giving a known motion to real tagged and cine CMR images of a healthy male. In order to generate these synthetic data, two pairs of cine ( $Cine^{image\ 1}$  and  $Cine^{image\ 2}$ ) and tagged CMR images ( $Tagged^{image\ 1}$  and  $Tagged^{image\ 2}$ ) with spatial resolution of  $256 \times 256$  are selected. Then the motion between the selected two tagged CMR images are estimated using [67]. The Figure 3.2 shows two tagged CMR images and estimated motion. Later this estimated motion is used as ground truth to evaluate the algorithms. After estimating the motion from real data, two new images ( $Tagged^{Simage}$  and  $Cine^{Simage}$ ) are created by interpolating the motion estimated with  $Tagged^{image1}$  and  $Cine^{image1}$ . Further, this estimated motion between a pair

### 3. Joint Motion Estimation Using Cine and Tagged CMR

of real tagged CMR images using [67] can be considered as a motion that represent complex rotations and contractions of LV approximately.

Now we have ( $Tagged^{image\ 1}$  and  $Tagged^{Simage}$ ) and ( $Cine^{image\ 1}$  and  $Cine^{Simage}$ ) which are having same known motion. In order to test the algorithms with noise, “Rician Noise” is added to  $Tagged^{Simage}$ . Therefore, final noisy image  $\tilde{I}_t$  is obtained by applying Rician noise to  $I_t$  as in Equation C.19, where  $c_1$  and  $c_2$  are normally distributed random variables with zero mean and variance  $\sigma_r^2$  [69] [58] [65].

$$\tilde{I}_t(x, y) = \sqrt{(I_t(x, y) + c_1)^2 + c_2^2} \quad (C.19)$$

Finally, noisy image  $Tagged^{Simage\ 0.5}$  is obtained by adding Rician noise of  $\sigma_r^2 = 0.5$  as showed in Figure 3.3. However, noise is not added to  $Cine^{Simage}$  since noise in real cine CMR images are relatively less effective.

After generating the synthetic data by giving a known motion to real tagged and cine CMR images, the proposed method and few other existing methods is evaluated.

Table 3.1: Optical flow methods used for evaluation and their abbreviations (*Only the proposed method is using both tagged and cine CMR images while the other methods are only using tagged CMR images*)

Method	Abbreviations
Proposed Method	PM
Variational method [58]	VM
Horn & Schunck method [67]	HS
Lucas & Kanade method [60]	LK

### 3. Joint Motion Estimation Using Cine and Tagged CMR

---

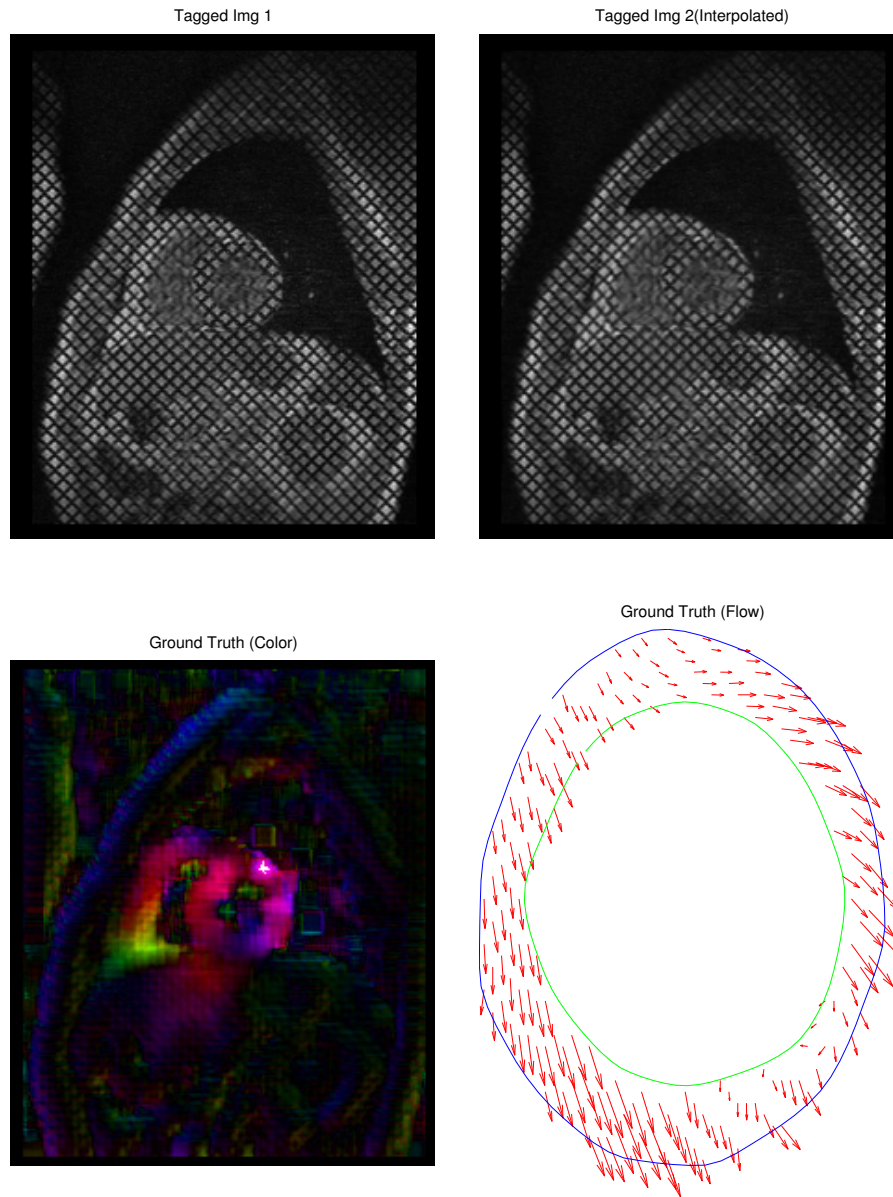
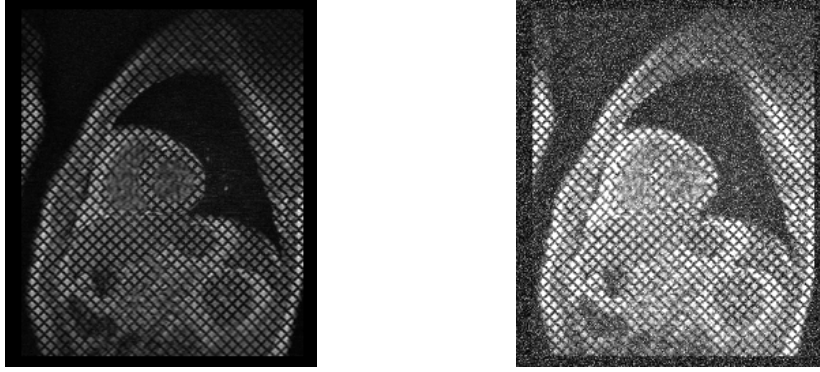


Figure 3.2: The motion estimated between two tagged MR images (top-left and top-right) is used as ground truth. The ground truth is illustrated using a color wheel (bottom-left) and using vector fields within myocardium (bottom-right).



(a) Interpolated Tagged Image

(b)  $\sigma_r^2 = 0.5$  noise added

Figure 3.3: The pair of tagged CMR images created in synthetic data - Method A, a) known motion interpolated image and b) after adding rician noise to the image in a).

Table 3.2: Mean and STD of angle and pixel errors obtained from synthetic data method A, with out adding noise (abbreviations are indicated in Table 3.1)

Method	Angle Error		Pixels Error	
	Mean	STD	Mean	STD
HS	8.913206	1.866722	0.748801	0.321206
LK	6.029994	1.432386	<b>0.093221</b>	0.128575
VM	9.707466	3.194840	0.280561	0.244060
PM	<b>5.557973</b>	<b>1.302442</b>	0.111354	<b>0.121222</b>

#### 3.5.2 Synthetic Data - Method B

This synthetic data generation models the expansion and contraction of an annular object. The proposed method is based on the method used in [65] and aims to assess the accuracy and robustness of the selected methods (in Table 3.1) by considering only pure radial motion and eliminating the influence of other factors, which typically increase the error in tag position estimation[65]. Tagged and cine images are generated using numerical simulations of signal, noise, and motion to



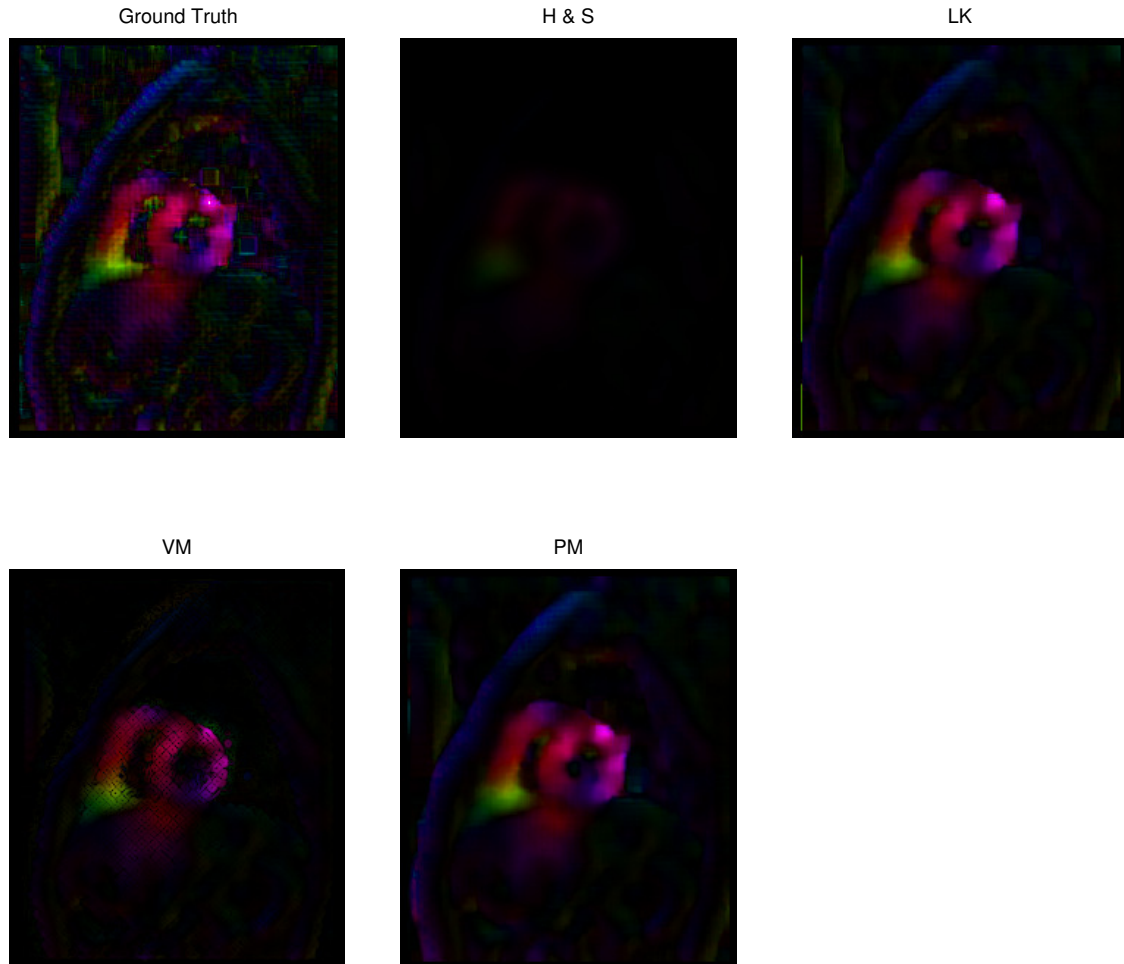


Figure 3.4: Results obtained with synthetic data - method  $A$  (without noise) is illustrated using a color wheel.

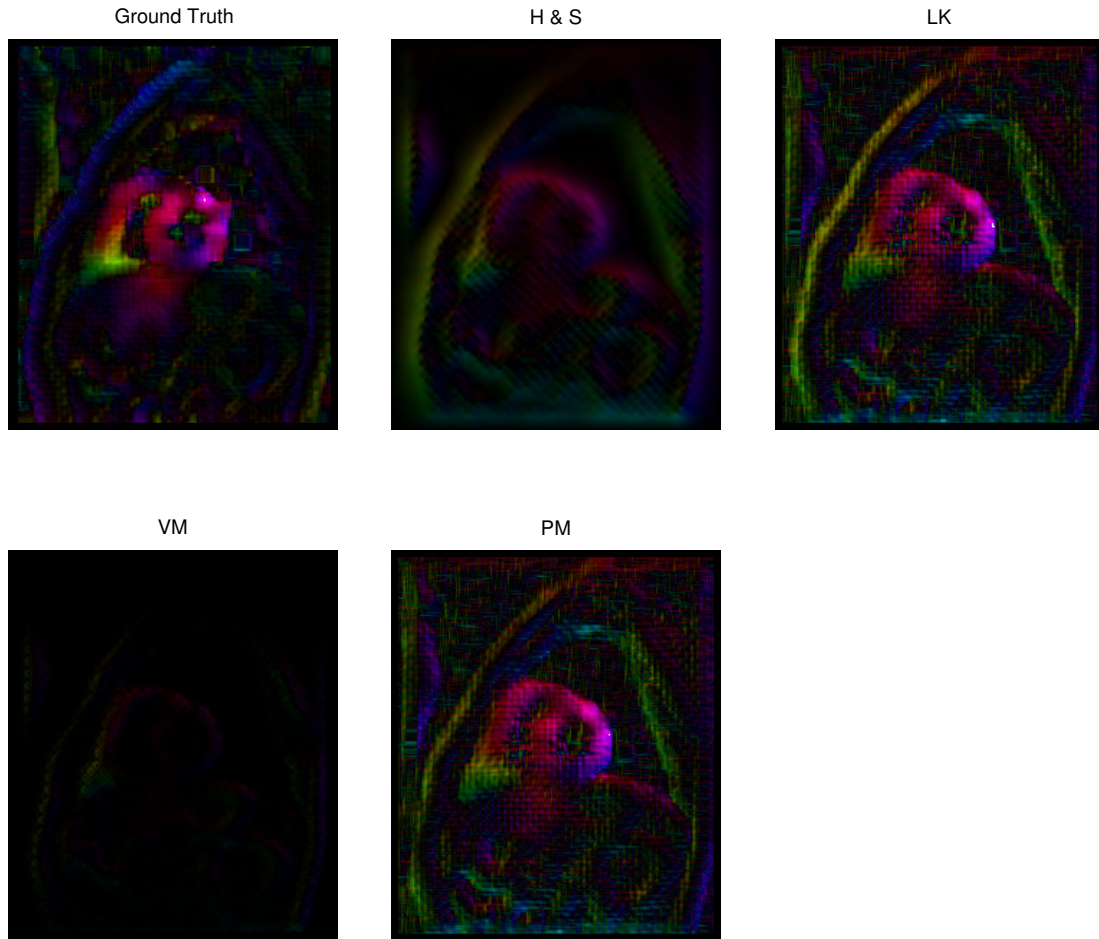


Figure 3.5: Results obtained with synthetic data - method  $A$  (with noise) is illustrated using a color wheel.

### 3. Joint Motion Estimation Using Cine and Tagged CMR

Table 3.3: Mean and STD of angle and pixel errors obtained from synthetic data-method  $A$ , with added noise (abbreviations are indicated in Table 3.1)

Method	Angle Error		Pixels Error	
	Mean	STD	Mean	STD
HS	17.122046	2.606918	0.611332	0.311961
LK	15.426983	2.418938	<b>0.206301</b>	0.236503
VM	18.310476	2.598635	0.831756	0.332600
PM	<b>14.066784</b>	<b>2.253401</b>	0.210594	<b>0.222719</b>

systematically test the performance.

The two image sequences consisted of  $T$  images  $I_t$  (size  $256 \times 256$  pixels). If the myocardium has an outer radius  $r_{ext}$  and inner radius  $r_c$ , the motion can be described as below.

$$r_t = \frac{(r_t^{out} - r_t^{in})}{(r_{ext} - r_c)}(r - r_c) + r_t^{in}, \theta_t = \theta \quad (\text{C.20})$$

where

$$r_t^{in} = r_c + kA \sin(\pi t/T)$$

and

$$r_t^{out} = \sqrt{r_{ext}^2 - r_c^2 + (r_t^{in})^2}$$

In Equation C.20,  $t$  represents the cardiac phase and  $(r, \theta)$  and  $(r_t, \theta_t)$  indicates the corresponding polar coordinates of a point in two consecutive images. Further,  $A$  controls the motion amplitude while  $k$  determines the motion type ( $k = 1$  represents expansion and  $k = -1$  represents contraction) [65]. The parameters were fixed to the following values (all spatial parameters are in pixel units):  $d = 8$  (spacing of tag lines),  $r_c = 50$ ,  $r_{ext} = 80$ ,  $I_{myo} = 10$  (intensity within annuls),

$I_{bg} = 0$  (background intensity),  $A = 20$  and  $T = 24$ .

#### Generation of synthetic tagged image sequence

Firstly the image with grids (tag lines) is created using a two dimensional sine function and then random noise is added to the image with grids which mimic the real tagged CMR image. Moreover, the created image then convolved with a Gaussian kernel in order to generate a similar intensity profile as in a tagged CMR image in ED phase (Figure 3.6).

After generating the first synthetic tagged CMR image then the motion is estimated according to the Equation C.20. In this experiment, first four images have been taken and each image is added a gradually increasing Rician noise of  $\sigma_r^2 = 0.5, 1, 1.5, 2$  consecutively according to the Equation C.19. Figure 3.7 shows the first four frames of the synthetic tagged CMR sequence and Figure 3.8 shows the evolution of simulated tagged fading. The tag fading effect is visible due to the addition of increasing rician noise in consecutive images.

#### Generation of synthetic Cine image sequence

In order to generate the first synthetic cine CMR image, a speckle image is generated and random noise is added to the speckle image. Then after, this speckle image is convolved with a Gaussian kernel in order to generate a similar intensity profile as in a cine CMR image in ED phase. Then after the motion derived from Equation C.20 was applied generate a synthetic cine CMR sequence as shown in Figure 3.9. However, noise is not added to these synthetic cine images since the noise in real cine CMR images are relatively less effective.

### 3. Joint Motion Estimation Using Cine and Tagged CMR

---

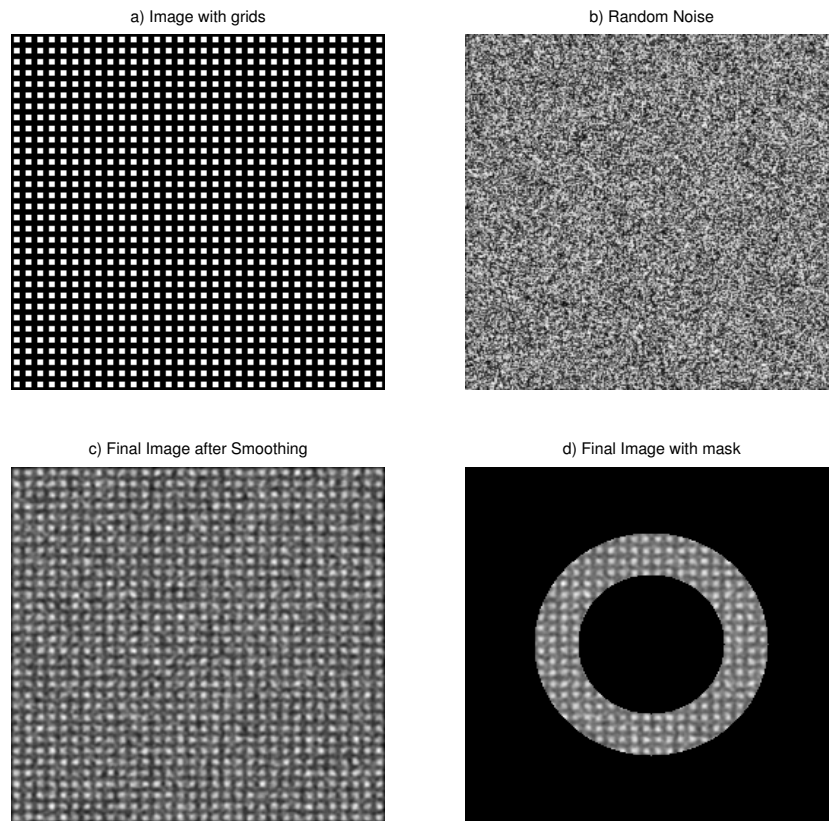


Figure 3.6: Process of generating first synthetic tagged CMR image in synthetic data - method  $B$ .

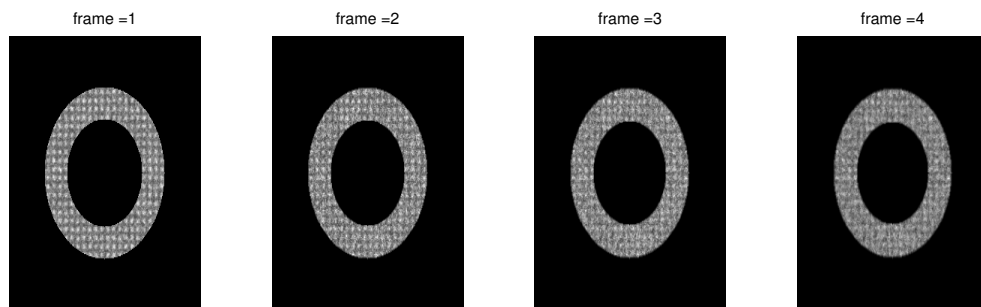


Figure 3.7: The first 4 frames of synthetic tagged CMR sequence obtained using synthetic data - method  $B$ .

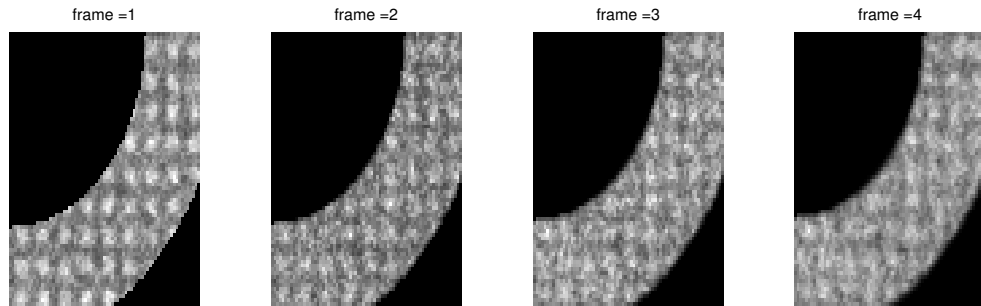


Figure 3.8: Simulated tag fading effect in synthetic tagged CMR sequence using synthetic data - method  $B$ .

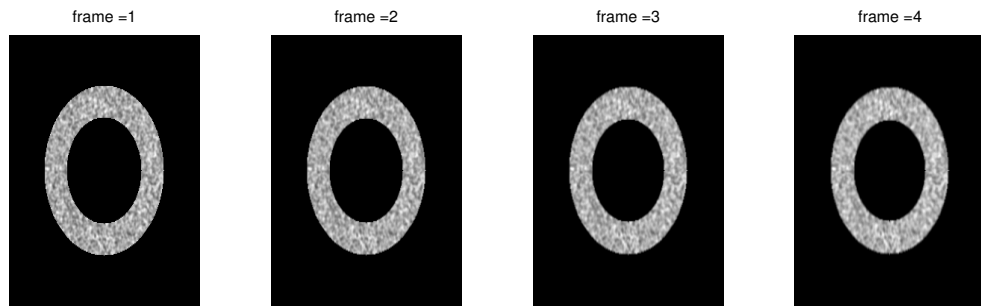


Figure 3.9: The first 4 frames of synthetic cine CMR sequence obtained using synthetic data - method  $B$ .

### 3. Joint Motion Estimation Using Cine and Tagged CMR

---

The synthetic tagged CMR and synthetic cine CMR sequences undergo same motion as illustrated in Figure 3.10. This motion and the derived strain from the motion was used as the ground truth to evaluate the performances of the selected algorithms with respect to the proposed algorithm.

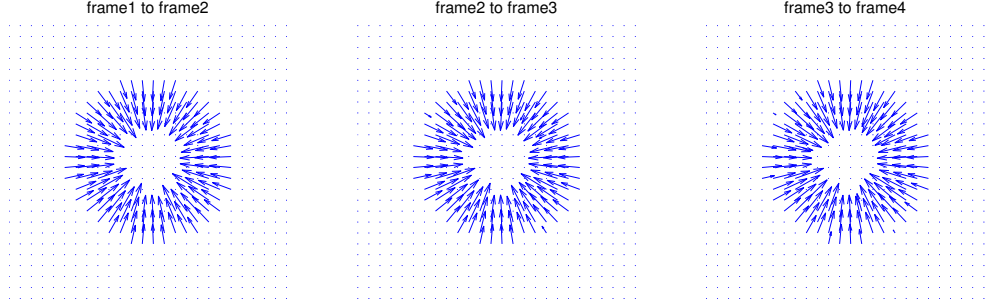


Figure 3.10: Ground truth radial motion between each pair of frames in synthetic tagged and cine sequences in synthetic data - method *B*.

#### 3.5.3 Experiments with Real Data

The proposed algorithm is tested with real CMR image sequences. The data were acquired with ECG gating by a 1.5T Siemens Symphony MRI scanner. Eulerian strains, radial and circumferential strains are calculated according to the standardized AHA myocardial division of segments. In order to assess the proposed algorithm qualitatively, points on myocardium has been selected and tracked to visualize the results of the proposed algorithm.

## 3.6 Results

### 3.6.1 Results with Simulated Data

#### 3.6.1.1 Synthetic Data - Method A

Table 3.2 shows the results obtained using the proposed algorithm and other selected algorithms by giving a known motion to two tagged/cine CMR images without adding noise. The results obtained using synthetic data-method *A* (without adding noise) can be visualized using a color wheel as in Figure 3.4. Moreover, the Table 3.3 shows the results obtained from giving a known motion to two tagged /cine CMR images after adding rician noise of  $\sigma_r^2 = 0.5$ . Both Tables 3.2 and 3.3 show mean and standard deviation of angle error of optical flow and pixel wise root mean squared error of optical flow. The results of experiment with Method *A* can also be visualized using color wheel as in Figure 3.4 and 3.5 .

#### 3.6.1.2 Synthetic Data - Method B

Table 3.4 shows the results obtained from Method *B* where synthetic tagged and cine images are constructed by giving a known radial motion. Table 3.4 shows mean and standard deviation of angle error of optical flow and pixel wise root mean squared error of optical flow in consecutive frame pairs.

### 3.6.2 Results with Real Data

The proposed algorithm is tested using real human CMR data. In order to present the results, basal slice of a healthy male is used. The Figure 3.13 demonstrates slice-wise global radial and circumferential strain calculated within myocardium.



### 3. Joint Motion Estimation Using Cine and Tagged CMR

---

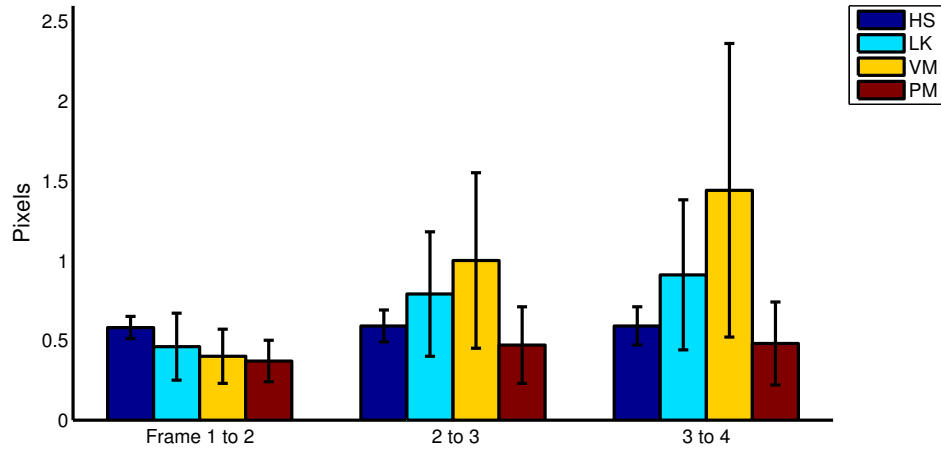


Figure 3.11: Pixel error bar plot of the results in Table 3.4

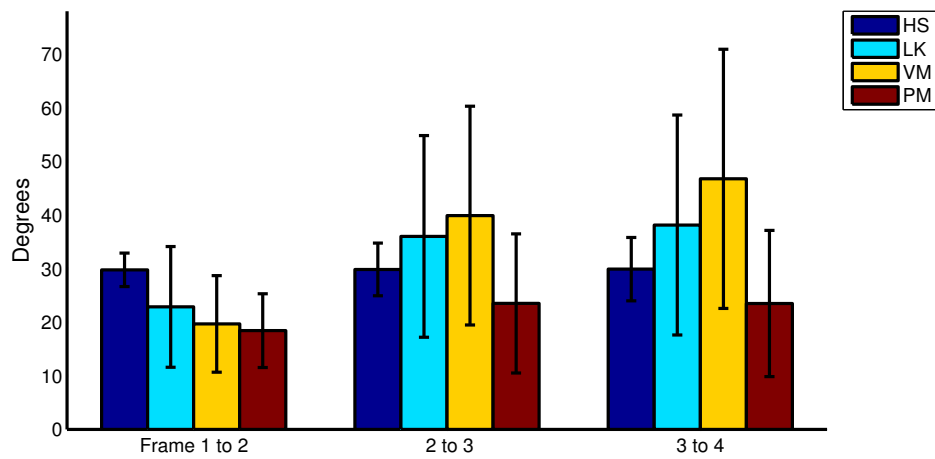


Figure 3.12: Angle error bar plot of the results in Table 3.4

### 3. Joint Motion Estimation Using Cine and Tagged CMR

Table 3.4: Angle and pixel error of optical flow obtained after applying the methods in Table 3.1 to synthetic data - method *B*.

<b>Frame 1 to 2</b>				
Method	Angle Error		Pixels Error	
	Mean	STD	Mean	STD
HS	29.75	3.12	0.58	0.07
LK	22.85	11.26	0.46	0.21
VM	19.66	9.01	0.4	0.17
PM	18.42	6.88	0.37	0.13

<b>Frame 2 to 3</b>				
Method	Angle Error		Pixels Error	
	Mean	STD	Mean	STD
HS	29.83	4.91	0.59	0.1
LK	35.99	18.8	0.79	0.39
VM	39.88	20.4	1	0.55
PM	23.49	12.97	0.47	0.24

<b>Frame 3 to 4</b>				
Method	Angle Error		Pixels Error	
	Mean	STD	Mean	STD
HS	29.89	5.91	0.59	0.12
LK	38.11	20.51	0.91	0.47
VM	46.73	24.18	1.44	0.92
PM	23.47	13.64	0.48	0.26

The Figure 3.14 shows average XX, XY, YY eulerian strains calculated within myocardium. Moreover, Figures 3.15 and 3.16 show circumferential and radial strains calculated according to the standard AHA myocardium segmentation. The XX,XY,YY eulerian strains calculated according to the standard myocardium segmentation is presented in Figures 3.17, 3.18 and 3.19. The change of circumferential and radial strains within myocardium are illustrated in Figure 3.22 and Figure 3.21 using color map in Figure 3.20.

The Figure 3.23 shows tracked points along 16/20 frames of a basal slice and 3.24 shows trajectories of selected points in Figure 3.23. The tracked points along 16 frames and trajectories of the points have been presented in order to provide a qualitative measure regarding the results of the proposed algorithm.

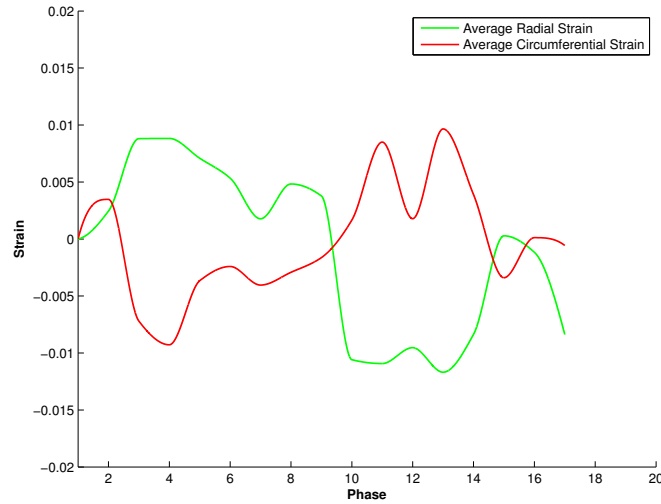


Figure 3.13: Global circumferential and radial strains of a basal slice calculated within whole myocardium

## 3.7 Discussion

As can be seen from the Table 3.2, the proposed method preserves the angles of optical flow (the displacement) than other methods in noise free experiment. Moreover, the proposed method shows the minimum STD with respect to other methods. However, the [60] method shows the minimum RMSE pixel error. Further, with the presence of noise in synthetic data method *A*, the Table 3.3 shows that the proposed method still preserves the angles of optical flow (the displace-

### 3. Joint Motion Estimation Using Cine and Tagged CMR

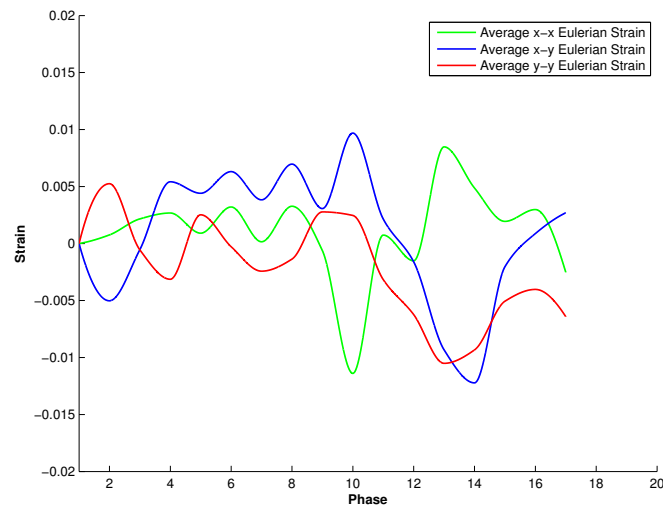


Figure 3.14: XX,XY,YY Eulerian strains of a basal slice calculated in whole myocardium

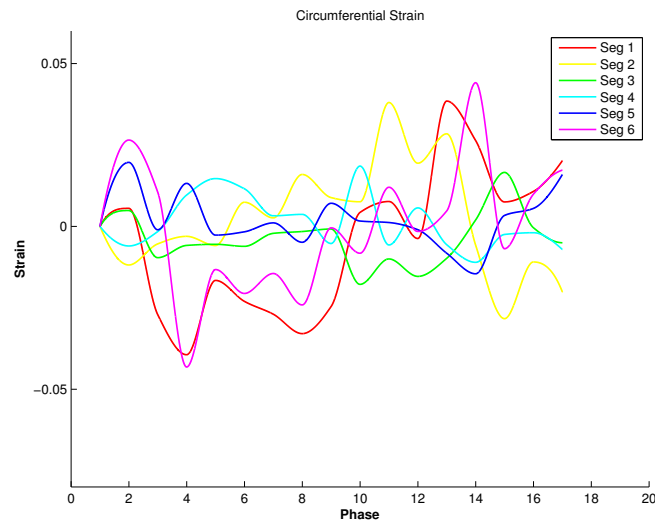


Figure 3.15: Circumferential strain of a basal slice calculated according to standard segmentation

### 3. Joint Motion Estimation Using Cine and Tagged CMR

---

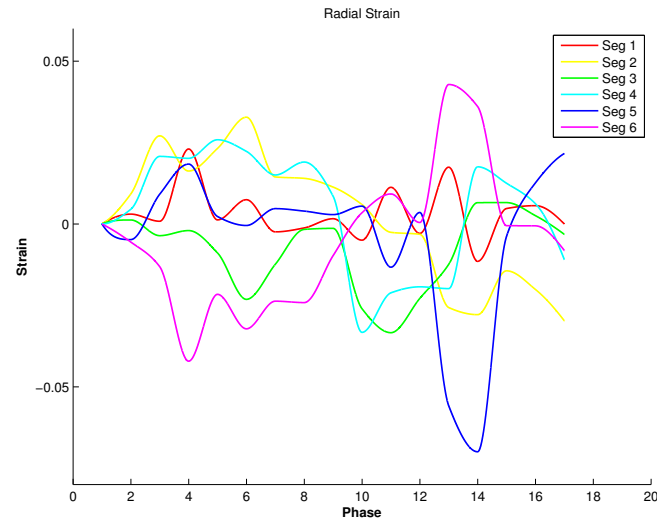


Figure 3.16: Radial strain of a basal slice calculated according to standard segmentation

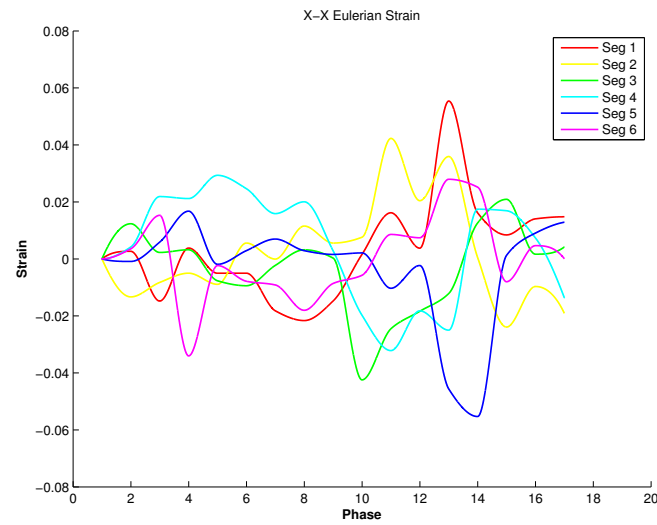


Figure 3.17: XX Eulerian strains of a basal slice calculated according to standard segmentation

### 3. Joint Motion Estimation Using Cine and Tagged CMR

---

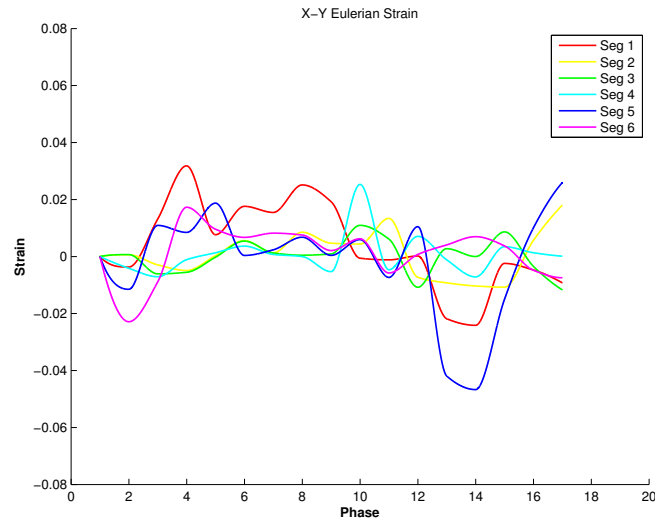


Figure 3.18: XY Eulerian strains of a basal slice calculated according to standard segmentation

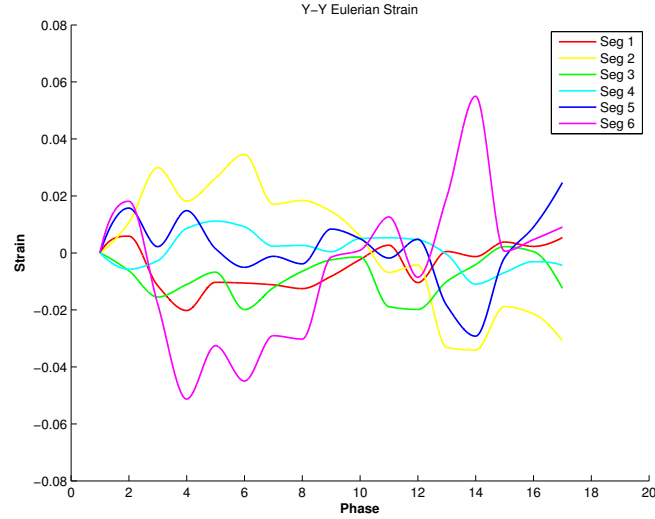


Figure 3.19: YY Eulerian strains of a basal slice calculated according to standard segmentation

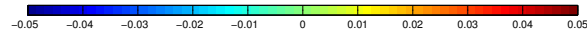


Figure 3.20: Color map used for strain illustrations

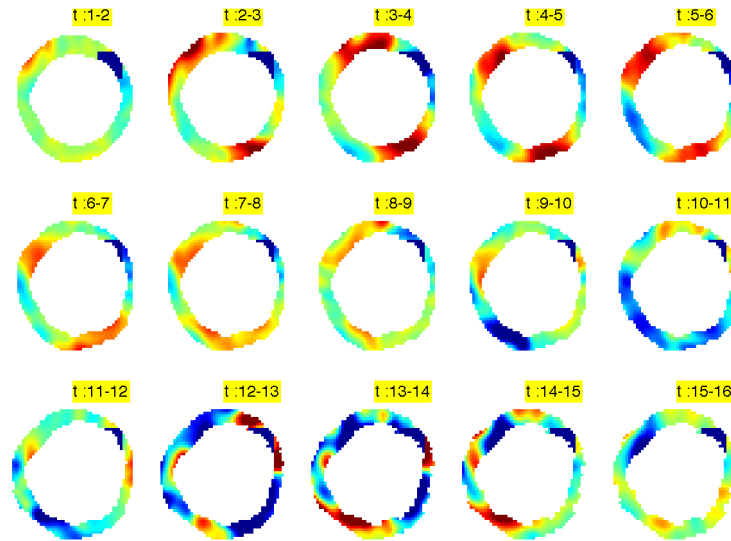


Figure 3.21: Evolution of radial strain visualized using color map in Figure 3.20

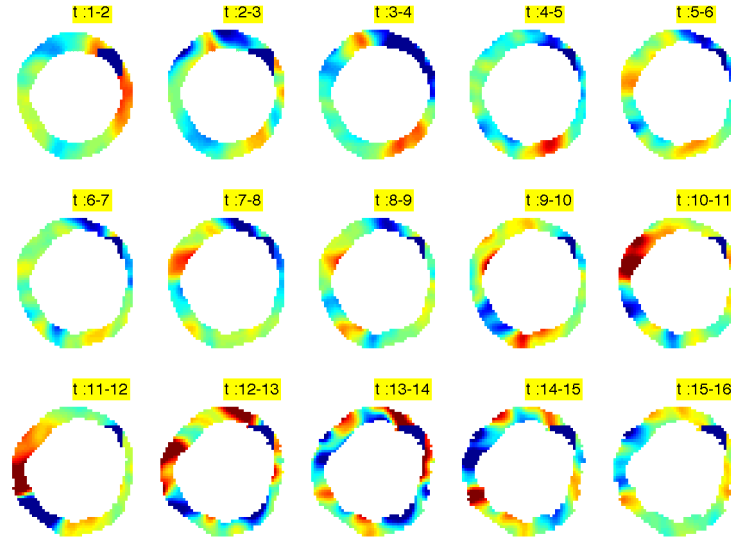


Figure 3.22: Evolution of circumferential strain visualized using color map in Figure 3.20

ment) than other methods. Even though, the [60] method still shows the minimum RMSE pixel error, the proposed method also has a very close error average RMSE pixel Error to the error of [60] method. However, the proposed method shows the minimum STD with respect to other methods. The Figure 3.4 and 3.5 also show qualitatively that the proposed method is able to recover the motion with a reasonable accuracy.

When considering the results of synthetic data method *B*, Table 3.4 shows that the proposed method preserves the angles of optical flow than other methods in consecutive images where the noise is gradually increasing. Even though the [60] method shows better results with synthetic data in method *A*, [60] method shows larger errors with synthetic data in method *B*. This larger error gap suggests that the [60] method is not capable of handling gradually increasing noise. Moreover, Figures 3.11 and 3.12 show that the angle and pixel error of the proposed method



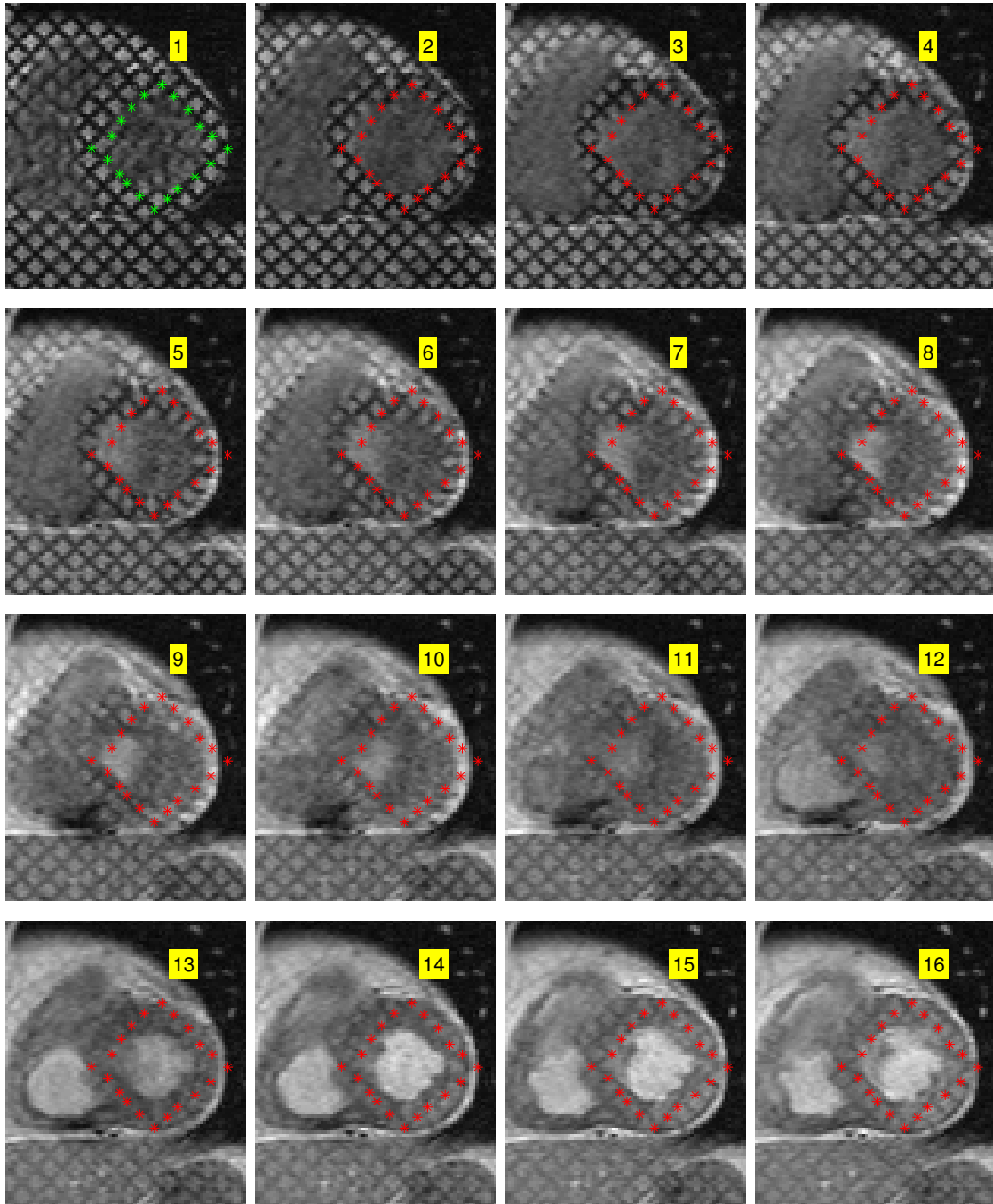


Figure 3.23: Tracked points along 16/20 frames of a basal slice. Frame numbers are indicated at the top-right of each image

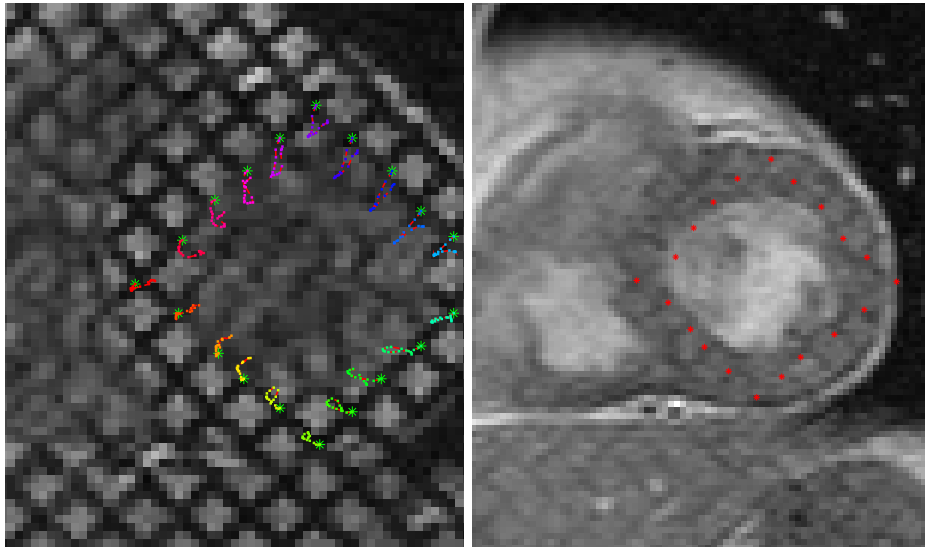


Figure 3.24: Trajectories of selected Points in Figure 3.23

is minimum and more consistent with gradually increasing noise in synthetic data - method  $B$ .

As can be seen in point tracking results shown in Figure 3.23, the points are appeared to be consistent even with the presence of tag fading effect in tagged CMR image sequence. Figure, 3.24 shows that the tracked points can be empirically accepted with respect to the selected points in the first frame.

According to the results obtained from both synthetic data and real data, it can be concluded that the proposed algorithm provides more robust motion estimation even with the presence of noise. Moreover, the results show that the proposed method preserve the angles of displacement (optical flow) which is important in calculating strain measures like radial and circumferential strain. Further, the proposed method shows that joint estimation of cardiac motion using both cine and tagged CMR images tend to be more robust to noise than using a single modality.

# Chapter 4

## Correlation Analysis

This chapter describes the statistical correlation analysis carried out using both strain and infarct data. The statistical analysis aims to identify relationship between strain measures and infarctions. These strain measures were derived from the proposed algorithm described in previous chapter and infarct quantification was done using the framework suggested in [5]. The objectives of the study, processing of data and results have been discussed in the sections below.

### 4.1 Objective

The main objective of this study is to evaluate the ability of established and new strain parameters of global and regional cardiac left ventricle function to estimate myocardial infarct percentage. In order to assess the infarct predicting ability of each parameter, different strain measures (global and regional) and regional I/M% are being studied. In addition, this analysis has taken the data related to whole cardiac cycle without restricting to systolic or diastolic phase. In this

study, both maximum and minimum strains have in-cooperated while most of the available studies concerning a one-peak value during either systolic or diastolic phase. Further, this study aims to evaluate global and regional eulerian strains without restricting to lagrangian radial and circumferential strains. Assessing LV cardiac function according to different AHA segment-wise arrangements is another goal of this study. Therefore, the cardiac function is analyzed according to simple vertical and horizontal arrangements. Finally, the effect of regional I/M% to global strain measures has also been taken in to consideration.

### 4.2 Data

We have collected 10 sets of real patient data with varying amounts of infarcts for the evaluation. The data were acquired with ECG gating by a 1.5T Siemens Symphony MRI scanner from 10 patients (10 males, 38-81 years old, mean age  $52 \pm 10$ ) three months after myocardial infarction, following a bolus injection of a gadolinium-based contrast agent. Tagged, Cine and LGE sequences of a same subject comprise the same number of SA slices with the **same scan locations**. Depending on the individual heart size, there can be 8-11 SA slices for a patient. While slices of a Tagged/Cine sequence comprise 20-25 frames, slices of an LGE sequence comprise only one frame.

## 4.3 Data Processing

### 4.3.1 Infarct Quantification

The LGE CMR images have been processed using the infarct quantification framework suggested by [5]. The regional infarct percentage (I/M%) for each standard AHA myocardial segment is derived. The I/M% has been further averaged when the same segment appears in multiple slices (apical, mid and basal) and this averaged I/M% is used for statistical analysis.

### 4.3.2 Strain Quantification

Firstly the strain tensors were calculated from the tagged and cine SA slices of the 10 patients for the whole cardiac cycle. In order to calculate the cardiac motion (displacement), the proposed method was used. Therefore, displacement was estimated using both cine and tagged CMR data. Lagrangian strains (radial (CS) and circumferential strain (RS)) and eulerian strains (in XX, XY, YY directions) were calculated subsequently. These 5 strains were calculated according to standard AHA myocardium segmentation. In addition to AHA segment-wise strains, each of these strains was calculated for whole myocardium region appears within a particular slice. Moreover, Efficient Strain (ES) which is obtained by subtracting the CS from the RS at the same time for particular region and time instance. Further, efficient strains were also calculated according to the standard AHA myocardium segmentation as in other strains. Finally, maximum and minimum strains take place in each strain parameter (within whole cardiac cycle) was taken for correlation analysis with I/M%. Altogether, 24 descriptors were extracted for the study.

## 4. Correlation Analysis

The type, description and abbreviations of these strain measures are shown in Table 4.1. Figures 4.1 and 4.2 shows the scatter plot of derived regional strain measures.

Table 4.1: Abbreviation and description of strain measures used for correlation analysis

Strain Type	Abb.	Description
Radial	$PRS^+$	Max. AHA segment-wise radial strain
	$PRS^-$	Min. AHA segment-wise radial strain
	$TRS^+$	Max. radial strain from slice wise global strain
	$TRS^-$	Min. radial strain from slice wise global strain
Circumferential	$PCS^+$	Max. AHA segment-wise circumf. strain
	$PCS^-$	Min. AHA segment-wise circumf. strain
	$TCS^+$	Max. circumf. strain from slice wise global strain
	$TCS^-$	Min. circumf. strain from slice wise global strain
Efficient	$PES^+$	Max. AHA segment-wise efficient strain
	$PES^-$	Min. AHA segment-wise efficient strain
	$TES^+$	Max. efficient strain from slice wise global strain
	$TES^-$	Min. efficient strain from slice wise global strain
Eulerian XX	$PXX^+$	Max. AHA segment-wise XX strain
	$PXX^-$	Min. AHA segment-wise XX strain
	$TXX^+$	Max. XX strain from slice wise global strain
	$TXX^-$	Min. XX strain from slice wise global strain
Eulerian XY	$PXY^+$	Max. AHA segment-wise XY strain
	$PXY^-$	Min. AHA segment-wise XY strain
	$TXY^+$	Max. XY strain from slice wise global strain
	$TXY^-$	Min. XY strain from slice wise global strain
Eulerian YY	$PYY^+$	Max. AHA segment-wise YY strain
	$PYY^-$	Min. AHA segment-wise YY strain
	$TYY^+$	Max. YY strain from slice wise global strain
	$TYY^-$	Min. YY strain from slice wise global strain

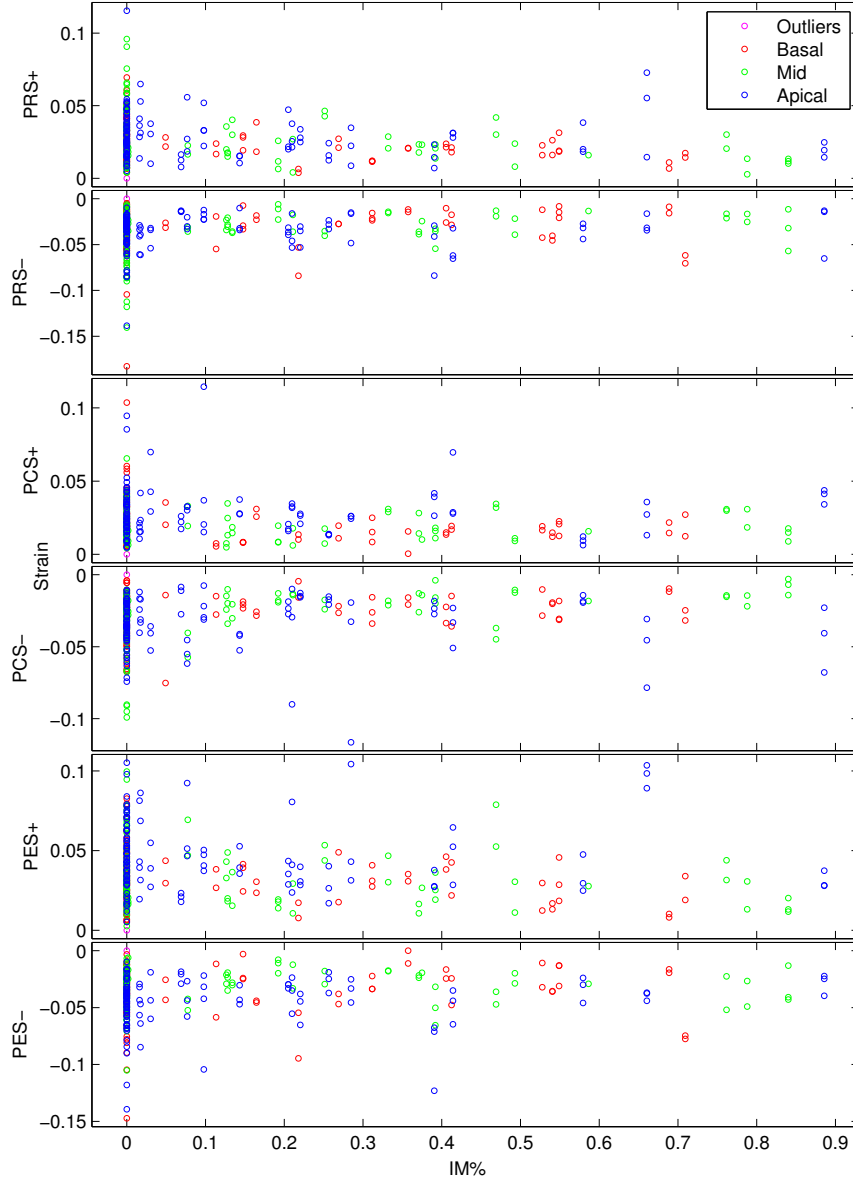


Figure 4.1: The scatter plot of Max. and Min. of regional Lagrangian strains calculated over whole cardiac cycle (I/M% was normalized in to [0 1])

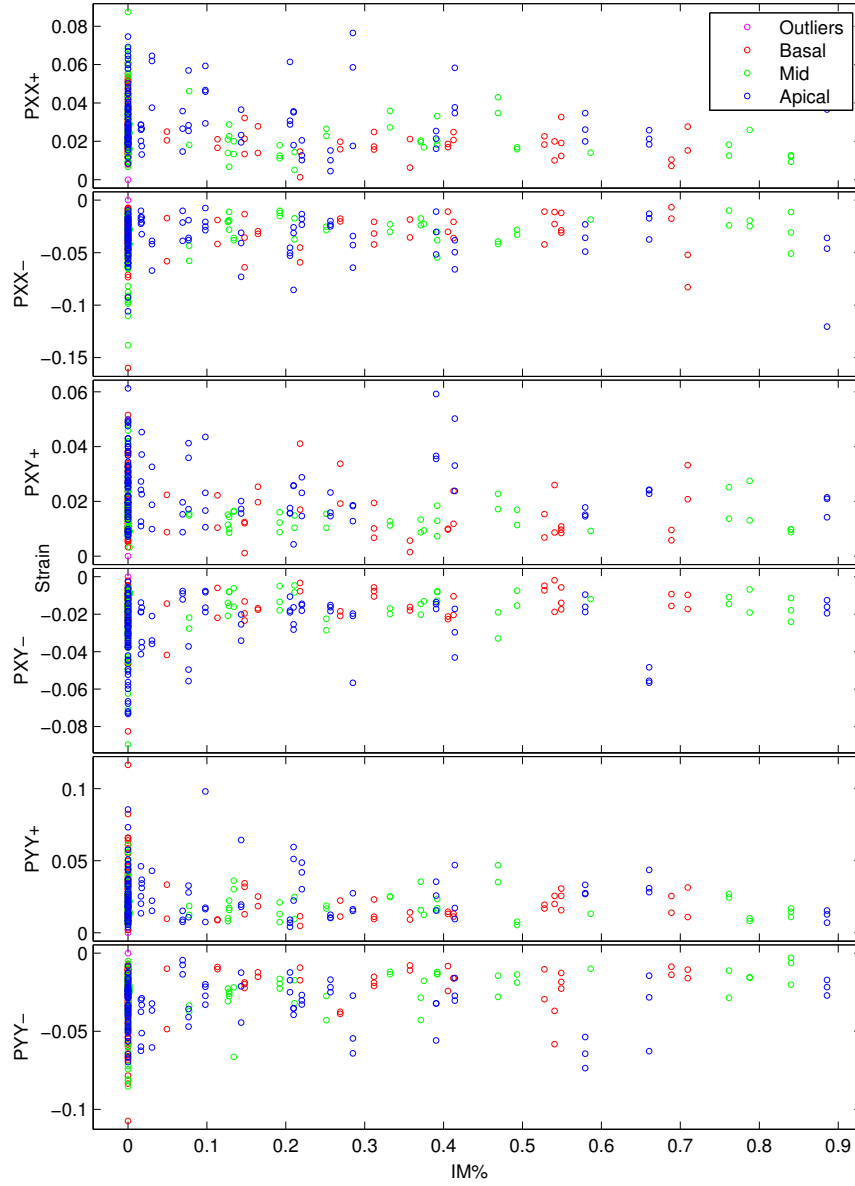


Figure 4.2: The scatter plot of Max. and Min. of regional Eulerian strains calculated over whole cardiac cycle (I/M% was normalized in to [0 1])



## 4.4 Statistical Analysis

Prior to statistical analysis, the I/M% was normalized in to  $[0\ 1]$  range. Subsequently, The pairwise Pearson's correlation coefficient ( $r$ ) is derived considering each I/M% and relevant strain measures. The statistical significance defined as  $p < 0.05$  for all tests.

Firstly, the correlation analysis is carried out considering three slice levels as in standard AHA myocardium segmentation. In this test, all segments are first analyzed without considering their slice location and subsequently, the test is carried out for basal, mid and apical slice segments considering the slice location. In this test, differences of segments within a particular slice has not been considered and the main goal of this test is to assess I/M%'s relationship with strain measures for each slice level. The results of this test have shown in Table 4.2.

Secondly, the correlation analysis is carried out by considering standard AHA myocardium segmentation. In this test, correlation between I/M% of each segment and relevant strain measures of particular segment is analyzed. The goal of this test is to analyze AHA segments-wise correlation of I/M% to each strain measure. The results of this test has shown in Table 4.3 and 4.4.

Thirdly, the correlation analysis is carried out by considering vertical arrangements in standard AHA myocardium segmentation. In this test, the myocardium segments are arranged in to vertical arrangements as anterior, anteroseptal, inferoseptal, inferior, inferolateral, and anterolateral. Subsequently, the correlation between I/M% and strain measures of segments of each of these vertical arrangements is analyzed. The results of this test has shown in Table 4.5.

#### 4. Correlation Analysis

Table 4.2: The results of slice-wise correlation analysis between I/M% strain measures in Table 4.1.  $*p < 0.05$ ,  $**p < 0.01$ ,  $***p < 0.001$  and  $\oslash$  indicates  $p > 0.05$

Strain Type	All Slices		Apical Slices		Mid Slices		Basal Slices	
	$r\%$	$p$	$r\%$	$p$	$r\%$	$p$	$r\%$	$p$
$PRS^+$	-18.54	***	-6.59	$\oslash$	<b>-24.61</b>	*	<b>-25.09</b>	**
$PRS^-$	10.70	$\oslash$	3.16	$\oslash$	20.02	*	6.55	$\oslash$
$PCS^+$	-7.68	$\oslash$	1.61	$\oslash$	-4.03	$\oslash$	-22.24	*
$PCS^-$	15.50	**	-6.02	$\oslash$	<b>34.78</b>	***	16.85	$\oslash$
$PES^+$	-9.83	$\oslash$	1.10	$\oslash$	-16.14	$\oslash$	-18.79	*
$PES^-$	6.08	$\oslash$	10.26	$\oslash$	2.34	$\oslash$	3.70	$\oslash$
$PXX^+$	-15.21	**	2.45	$\oslash$	-22.55	*	<b>-29.55</b>	**
$PXX^-$	6.73	$\oslash$	-15.74	$\oslash$	<b>24.46</b>	*	7.27	$\oslash$
$PXY^+$	-12.24	*	-6.95	$\oslash$	-19.57	*	-13.59	$\oslash$
$PXY^-$	15.44	**	10.39	$\oslash$	22.38	*	18.78	*
$PYY^+$	-10.58	$\oslash$	-1.60	$\oslash$	-14.76	$\oslash$	-15.22	$\oslash$
$PYY^-$	15.79	**	-4.76	$\oslash$	<b>27.32</b>	**	21.51	*
$TRS^+$	-5.68	$\oslash$	-7.00	$\oslash$	-1.89	$\oslash$	-14.03	$\oslash$
$TRS^-$	-4.96	$\oslash$	-8.05	$\oslash$	-3.66	$\oslash$	-3.60	$\oslash$
$TCS^+$	-7.54	$\oslash$	-19.05	*	-5.44	$\oslash$	2.48	$\oslash$
$TCS^-$	10.79	$\oslash$	3.04	$\oslash$	22.67	*	14.04	$\oslash$
$TES^+$	-9.03	$\oslash$	-1.82	$\oslash$	-20.44	*	-17.80	$\oslash$
$TES^-$	5.14	$\oslash$	9.69	$\oslash$	4.09	$\oslash$	2.18	$\oslash$
$TXX^+$	-11.46	*	<b>-34.71</b>	***	1.98	$\oslash$	6.99	$\oslash$
$TXX^-$	-8.49	$\oslash$	-16.11	$\oslash$	0.80	$\oslash$	-9.93	$\oslash$
$TXY^+$	-4.99	$\oslash$	-7.74	$\oslash$	-9.75	$\oslash$	1.43	$\oslash$
$TXY^-$	17.17	**	19.07	*	<b>29.10</b>	**	18.22	$\oslash$
$TY Y^+$	-14.35	**	-12.87	$\oslash$	-17.15	$\oslash$	-17.03	$\oslash$
$TY Y^-$	16.91	**	23.19	*	11.96	$\oslash$	<b>25.97</b>	**

Table 4.3: The results from standard AHA segment-wise correlation Analysis [Segments 1-8] between I/M% strain measures in Table 4.1.  $*p < 0.05$ ,  $**p < 0.01$ ,  $***p < 0.001$  and  $\circ$  indicates  $p > 0.05$

Strain Type	1		2		3		4		5		6		7		8	
	$r\%$	$p$	$r\%$	$p$	$r\%$	$p$	$r\%$	$p$	$r\%$	$p$	$r\%$	$p$	$r\%$	$p$	$r\%$	$p$
$PRS^+$	-9.29	$\circ$	-10.47	$\circ$	-37.11	$\circ$	<b>-49.10</b>	$\star$	<b>-55.71</b>	$\star$	-28.90	$\circ$	-18.80	$\circ$	-6.91	$\circ$
$PRS^-$	9.20	$\circ$	19.07	$\circ$	19.48	$\circ$	-39.42	$\circ$	20.74	$\circ$	43.52	$\circ$	-5.56	$\circ$	16.58	$\circ$
$PCS^+$	-42.23	$\circ$	-17.96	$\circ$	-12.50	$\circ$	-17.40	$\circ$	-26.42	$\circ$	-34.38	$\circ$	34.33	$\circ$	42.92	$\circ$
$PCS^-$	14.63	$\circ$	7.61	$\circ$	<b>-49.74</b>	$\star$	-2.33	$\circ$	28.34	$\circ$	<b>58.21</b>	$\star\star$	21.14	$\circ$	25.78	$\circ$
$PES^+$	14.00	$\circ$	-21.24	$\circ$	-1.30	$\circ$	-21.89	$\circ$	-33.31	$\circ$	<b>-56.62</b>	$\star$	-5.68	$\circ$	-8.04	$\circ$
$PES^-$	-14.20	$\circ$	22.36	$\circ$	10.00	$\circ$	-26.18	$\circ$	19.22	$\circ$	43.09	$\circ$	-31.07	$\circ$	-15.18	$\circ$
$PXX^+$	-19.86	$\circ$	-14.11	$\circ$	-20.58	$\circ$	-40.52	$\circ$	<b>-55.93</b>	$\star$	-37.63	$\circ$	34.55	$\circ$	4.04	$\circ$
$PXX^-$	-15.48	$\circ$	12.79	$\circ$	18.77	$\circ$	<b>-47.78</b>	$\star$	26.91	$\circ$	<b>49.65</b>	$\star$	17.11	$\circ$	9.28	$\circ$
$PXY^+$	-34.29	$\circ$	-17.38	$\circ$	-13.36	$\circ$	14.01	$\circ$	-12.54	$\circ$	<b>-51.31</b>	$\star$	17.78	$\circ$	<b>53.85</b>	$\star$
$PXY^-$	25.73	$\circ$	32.13	$\circ$	-42.08	$\circ$	24.66	$\circ$	38.49	$\circ$	31.18	$\circ$	14.13	$\circ$	21.00	$\circ$
$PYY^+$	-4.87	$\circ$	-24.14	$\circ$	-40.05	$\circ$	8.00	$\circ$	-8.34	$\circ$	-21.15	$\circ$	-16.80	$\circ$	-0.11	$\circ$
$PYY^-$	26.71	$\circ$	20.21	$\circ$	33.90	$\circ$	19.85	$\circ$	21.14	$\circ$	37.88	$\circ$	16.66	$\circ$	7.39	$\circ$
$TRS^+$	8.51	$\circ$	7.39	$\circ$	-3.15	$\circ$	-25.15	$\circ$	-41.10	$\circ$	-30.50	$\circ$	5.14	$\circ$	15.44	$\circ$
$TRS^-$	21.95	$\circ$	14.79	$\circ$	-17.62	$\circ$	-37.65	$\circ$	-2.67	$\circ$	14.54	$\circ$	-3.90	$\circ$	-23.58	$\circ$
$TCS^+$	-1.22	$\circ$	11.35	$\circ$	17.97	$\circ$	30.25	$\circ$	-13.17	$\circ$	-31.44	$\circ$	-1.58	$\circ$	24.69	$\circ$
$TCS^-$	-35.89	$\circ$	-39.88	$\circ$	0.00	$\circ$	33.54	$\circ$	<b>60.09</b>	$\star\star$	<b>49.86</b>	$\star$	14.86	$\circ$	9.55	$\circ$
$TES^+$	3.46	$\circ$	13.36	$\circ$	7.90	$\circ$	-16.38	$\circ$	<b>-57.19</b>	$\star$	<b>-55.14</b>	$\star$	-22.67	$\circ$	-6.19	$\circ$
$TES^-$	29.10	$\circ$	23.86	$\circ$	-27.45	$\circ$	-41.36	$\circ$	13.22	$\circ$	29.20	$\circ$	2.44	$\circ$	-26.87	$\circ$
$TXX^+$	30.78	$\circ$	33.48	$\circ$	-8.64	$\circ$	-18.92	$\circ$	3.50	$\circ$	7.50	$\circ$	36.12	$\circ$	23.62	$\circ$
$TXX^-$	-0.22	$\circ$	-0.58	$\circ$	-5.30	$\circ$	-22.69	$\circ$	-16.10	$\circ$	-6.62	$\circ$	-33.06	$\circ$	-40.82	$\circ$
$TXY^+$	-26.01	$\circ$	-23.52	$\circ$	12.99	$\circ$	30.82	$\circ$	4.56	$\circ$	-7.33	$\circ$	-1.85	$\circ$	14.27	$\circ$
$TXY^-$	6.65	$\circ$	0.05	$\circ$	5.70	$\circ$	21.14	$\circ$	40.81	$\circ$	36.15	$\circ$	22.25	$\circ$	18.57	$\circ$
$TY Y^+$	-4.07	$\circ$	-3.20	$\circ$	-7.48	$\circ$	-5.03	$\circ$	-43.90	$\circ$	-43.73	$\circ$	-9.64	$\circ$	-2.08	$\circ$
$TY Y^-$	-10.67	$\circ$	-19.23	$\circ$	38.20	$\circ$	<b>47.36</b>	$\star$	<b>53.28</b>	$\star$	44.32	$\circ$	-7.51	$\circ$	-33.41	$\circ$

Table 4.4: The results from standard AHA segment-wise correlation Analysis [Segments 9-10] between I/M% strain measures in Table 4.1.  $*p < 0.05$ ,  $**p < 0.01$ ,  $***p < 0.001$  and  $\circ$  indicates  $p > 0.05$

Strain Type	9		10		11		12		13		14		15		16	
	$r\%$	$p$	$r\%$	$p$	$r\%$	$p$	$r\%$	$p$	$r\%$	$p$	$r\%$	$p$	$r\%$	$p$	$r\%$	$p$
<i>PRS</i> <sup>+</sup>	-6.03	$\circ$	<b>-60.01</b>	*	-46.84	$\circ$	<b>-52.21</b>	*	-16.95	$\circ$	13.67	$\circ$	-0.01	$\circ$	<b>-40.86</b>	*
<i>PRS</i> <sup>-</sup>	18.21	$\circ$	<b>48.75</b>	*	36.08	$\circ$	39.88	$\circ$	-8.64	$\circ$	7.85	$\circ$	27.93	$\circ$	-3.71	$\circ$
<i>PCS</i> <sup>+</sup>	-17.76	$\circ$	-36.87	$\circ$	<b>-54.22</b>	*	-37.59	$\circ$	8.55	$\circ$	-17.98	$\circ$	17.83	$\circ$	-10.08	$\circ$
<i>PCS</i> <sup>-</sup>	24.58	$\circ$	<b>53.94</b>	*	<b>59.10</b>	*	<b>65.60</b>	**	-0.80	$\circ$	-16.10	$\circ$	-27.78	$\circ$	<b>40.27</b>	*
<i>PES</i> <sup>+</sup>	15.17	$\circ$	-9.35	$\circ$	<b>-55.19</b>	*	-46.94	$\circ$	-30.10	$\circ$	30.54	$\circ$	22.91	$\circ$	<b>-43.43</b>	*
<i>PES</i> <sup>-</sup>	11.46	$\circ$	10.83	$\circ$	26.14	$\circ$	33.53	$\circ$	20.28	$\circ$	24.37	$\circ$	16.94	$\circ$	-26.95	$\circ$
<i>PXX</i> <sup>+</sup>	-20.65	$\circ$	<b>-54.24</b>	*	<b>-66.76</b>	**	<b>-48.97</b>	*	20.30	$\circ$	-11.51	$\circ$	31.24	$\circ$	-36.87	$\circ$
<i>PXX</i> <sup>-</sup>	31.79	$\circ$	47.77	$\circ$	38.54	$\circ$	44.89	$\circ$	-36.21	$\circ$	-14.36	$\circ$	-4.17	$\circ$	7.04	$\circ$
<i>PXY</i> <sup>+</sup>	-15.44	$\circ$	-47.84	$\circ$	<b>-62.53</b>	**	-46.88	$\circ$	-20.42	$\circ$	-1.71	$\circ$	-7.58	$\circ$	12.52	$\circ$
<i>PXY</i> <sup>-</sup>	-5.13	$\circ$	37.19	$\circ$	<b>49.93</b>	*	<b>50.78</b>	*	37.34	$\circ$	-10.18	$\circ$	<b>-38.55</b>	*	<b>52.98</b>	**
<i>PYY</i> <sup>+</sup>	-38.51	$\circ$	-1.02	$\circ$	-47.32	$\circ$	<b>-57.58</b>	*	-9.24	$\circ$	18.21	$\circ$	6.30	$\circ$	-34.67	$\circ$
<i>PYY</i> <sup>-</sup>	3.83	$\circ$	36.05	$\circ$	<b>53.86</b>	*	<b>71.87</b>	**	16.76	$\circ$	-24.51	$\circ$	-27.65	$\circ$	25.40	$\circ$
<i>TRS</i> <sup>+</sup>	<b>72.71</b>	***	17.33	$\circ$	<b>-50.90</b>	*	-29.66	$\circ$	-14.76	$\circ$	-6.86	$\circ$	36.79	$\circ$	-35.40	$\circ$
<i>TRS</i> <sup>-</sup>	5.12	$\circ$	8.71	$\circ$	0.95	$\circ$	7.88	$\circ$	-19.30	$\circ$	-0.72	$\circ$	19.57	$\circ$	-14.75	$\circ$
<i>TCS</i> <sup>+</sup>	20.11	$\circ$	-11.30	$\circ$	-31.80	$\circ$	-33.03	$\circ$	-21.68	$\circ$	<b>-41.24</b>	*	-17.86	$\circ$	2.02	$\circ$
<i>TCS</i> <sup>-</sup>	-11.75	$\circ$	34.25	$\circ$	<b>49.73</b>	*	37.00	$\circ$	12.05	$\circ$	-7.93	$\circ$	<b>-38.28</b>	*	<b>43.58</b>	*
<i>TES</i> <sup>+</sup>	26.58	$\circ$	-20.27	$\circ$	-45.93	$\circ$	-46.82	$\circ$	-11.13	$\circ$	3.65	$\circ$	<b>47.25</b>	*	-36.12	$\circ$
<i>TES</i> <sup>-</sup>	-2.58	$\circ$	19.10	$\circ$	19.45	$\circ$	26.44	$\circ$	3.04	$\circ$	27.47	$\circ$	23.25	$\circ$	-2.47	$\circ$
<i>TXX</i> <sup>+</sup>	18.56	$\circ$	-28.12	$\circ$	-41.43	$\circ$	16.73	$\circ$	<b>-45.60</b>	*	<b>-47.78</b>	*	-5.92	$\circ$	<b>-42.74</b>	*
<i>TXX</i> <sup>-</sup>	4.04	$\circ$	<b>49.89</b>	*	43.25	$\circ$	-6.42	$\circ$	-8.72	$\circ$	-15.14	$\circ$	-30.40	$\circ$	-26.25	$\circ$
<i>TXY</i> <sup>+</sup>	14.34	$\circ$	-17.68	$\circ$	-36.49	$\circ$	-30.90	$\circ$	1.47	$\circ$	-19.97	$\circ$	-26.13	$\circ$	-8.50	$\circ$
<i>TXY</i> <sup>-</sup>	4.08	$\circ$	39.20	$\circ$	<b>50.54</b>	*	<b>48.43</b>	*	25.11	$\circ$	13.79	$\circ$	-5.65	$\circ$	<b>51.99</b>	**
<i>TYY</i> <sup>+</sup>	37.68	$\circ$	-5.24	$\circ$	<b>-56.73</b>	*	<b>-48.60</b>	*	-20.69	$\circ$	-6.16	$\circ$	-1.64	$\circ$	-30.34	$\circ$
<i>TYY</i> <sup>-</sup>	0.98	$\circ$	<b>57.45</b>	*	46.70	$\circ$	22.44	$\circ$	21.35	$\circ$	26.61	$\circ$	<b>39.26</b>	*	36.83	$\circ$

Table 4.5: he results from standard AHA vertical segments-wise correlation Analysis between I/M% strain measures in Table 4.1.  $*p < 0.05$ ,  $**p < 0.01$ ,  $***p < 0.001$  and  $\emptyset$  indicates  $p > 0.05$ . Ant-*anterior*, AS-*anteroseptal*, IS-*inferoseptal*, Inf-*inferior*, IL-*inferolateral*, AL- *anterolateral*

Strain Type	Ant		AS		IS		Inf		IL		AL	
	$r\%$	$p$	$r\%$	$p$	$r\%$	$p$	$r\%$	$p$	$r\%$	$p$	$r\%$	$p$
$PRS^+$	-6.38	$\emptyset$	-5.71	$\emptyset$	-22.07	$\emptyset$	<b>-31.96</b>	*	<b>-51.04</b>	**	<b>-35.50</b>	*
$PRS^-$	-8.54	$\emptyset$	14.80	$\emptyset$	21.19	$\emptyset$	5.70	$\emptyset$	23.65	$\emptyset$	<b>39.64</b>	*
$PCS^+$	13.36	$\emptyset$	13.70	$\emptyset$	-11.57	$\emptyset$	-6.99	$\emptyset$	<b>-38.96</b>	*	-32.67	$\emptyset$
$PCS^-$	2.78	$\emptyset$	16.45	$\emptyset$	-25.60	$\emptyset$	6.81	$\emptyset$	<b>46.04</b>	**	<b>57.76</b>	***
$PES^+$	-7.71	$\emptyset$	-8.58	$\emptyset$	5.93	$\emptyset$	-7.29	$\emptyset$	<b>-47.06</b>	**	<b>-43.92</b>	**
$PES^-$	-0.89	$\emptyset$	-0.06	$\emptyset$	9.22	$\emptyset$	-4.72	$\emptyset$	20.02	$\emptyset$	<b>35.45</b>	*
$PXX^+$	22.64	$\emptyset$	-6.00	$\emptyset$	-19.70	$\emptyset$	-20.98	$\emptyset$	<b>-58.88</b>	***	<b>-38.36</b>	*
$PXX^-$	<b>-24.75</b>	*	11.15	$\emptyset$	21.26	$\emptyset$	0.78	$\emptyset$	29.49	$\emptyset$	<b>44.38</b>	**
$PXY^+$	-7.77	$\emptyset$	23.09	$\emptyset$	-13.79	$\emptyset$	-5.39	$\emptyset$	<b>-44.77</b>	**	<b>-46.05</b>	**
$PXY^-$	16.01	$\emptyset$	18.31	$\emptyset$	-17.74	$\emptyset$	9.48	$\emptyset$	<b>37.71</b>	*	<b>37.54</b>	*
$PYY^+$	-4.95	$\emptyset$	-12.25	$\emptyset$	<b>-37.20</b>	*	2.40	$\emptyset$	-25.34	$\emptyset$	-31.29	$\emptyset$
$PYY^-$	14.54	$\emptyset$	15.68	$\emptyset$	24.24	$\emptyset$	11.81	$\emptyset$	<b>39.54</b>	*	<b>38.52</b>	*
$TRS^+$	-0.05	$\emptyset$	14.08	$\emptyset$	30.43	$\emptyset$	2.39	$\emptyset$	<b>-45.44</b>	**	-27.49	$\emptyset$
$TRS^-$	-15.49	$\emptyset$	-9.87	$\emptyset$	-6.20	$\emptyset$	3.29	$\emptyset$	-2.70	$\emptyset$	11.63	$\emptyset$
$TCS^+$	-3.00	$\emptyset$	13.61	$\emptyset$	19.89	$\emptyset$	-7.15	$\emptyset$	-23.74	$\emptyset$	-30.84	$\emptyset$
$TCS^-$	2.01	$\emptyset$	-10.15	$\emptyset$	-4.19	$\emptyset$	10.96	$\emptyset$	<b>49.53</b>	**	<b>40.49</b>	*
$TES^+$	-4.87	$\emptyset$	3.18	$\emptyset$	14.33	$\emptyset$	0.12	$\emptyset$	<b>-45.75</b>	**	<b>-47.65</b>	**
$TES^-$	-0.45	$\emptyset$	-4.33	$\emptyset$	-17.01	$\emptyset$	2.71	$\emptyset$	14.18	$\emptyset$	27.92	$\emptyset$
$TXX^+$	-7.77	$\emptyset$	28.83	$\emptyset$	2.87	$\emptyset$	-19.26	$\emptyset$	-25.75	$\emptyset$	10.30	$\emptyset$
$TXX^-$	-15.93	$\emptyset$	-17.48	$\emptyset$	-2.06	$\emptyset$	-1.25	$\emptyset$	11.60	$\emptyset$	-6.37	$\emptyset$
$TXY^+$	6.00	$\emptyset$	-1.98	$\emptyset$	13.13	$\emptyset$	-10.62	$\emptyset$	-21.48	$\emptyset$	-16.02	$\emptyset$
$TXY^-$	13.03	$\emptyset$	3.90	$\emptyset$	7.89	$\emptyset$	16.18	$\emptyset$	<b>36.56</b>	*	<b>36.97</b>	*
$TYY^+$	-12.66	$\emptyset$	-1.26	$\emptyset$	11.85	$\emptyset$	-6.15	$\emptyset$	<b>-50.29</b>	**	<b>-42.92</b>	**
$TYY^-$	-0.02	$\emptyset$	-28.42	$\emptyset$	26.05	$\emptyset$	<b>42.27</b>	***	<b>41.32</b>	*	<b>36.36</b>	*

## 4.5 Results and Discussion

As it can be seen in Table 4.2,  $PRS^+$  shows a negative and weaker correlation with a higher significance ( $p < 0.05$ ) in mid and basal slices. These results suggest that the maximum regional radial strain in mid and basal slice segments may reduce due to the presence of infarctions. The Table 4.2 also shows that  $PCS^-$  has a weaker and positive correlation with I/M%. This weaker correlation suggests that the minimum regional circumferential strain may also increase due to the presence of infarctions and therefore the circumferential contraction may become weak in mid slices. Moreover, both  $PXX^-$  and  $PYY^-$  also show a positive and weaker correlation with I/M% in mid slices. Hence, it suggests that both minimum XX and YY strains are sensitive to infarctions. Further, according to the results in Table 4.2, I/M% in apical slice segments have a negative and weaker correlation with the slice-wise maximum XX eulerian strain ( $TXX^+$ ) and this result suggest that the global myocardial extraction of apical slices in XX direction may reduce due to the presence of infarctions. In addition to that, it can be seen that minimum value of global eulerian strains in XY and YY directions are also showing a positive and weaker correlation in mid and basal slices consecutively.

When considering the results of AHA segment-wise correlation analysis in Table (4.3 and 4.4), it can be seen that more moderate and stronger correlations are visible than the basal, mid and apical slices wise correlation analysis. As can be seen in Table 4.3, any correlation with a higher significance was not detected in Segment 1 and 2. However, I/M% of Segment 3 shows a moderate negative correlation of 49% with regional minimum circumferential strain ( $PCS^-$ ). The I/M% in Segment 4 shows a negative and moderate correlations with maximum regional ra-

dial strain ( $PRS^+$ ) and minimum regional XX directional eulerian strain ( $PXX^-$ ). Specially, the I/M% in Segment 4 shows a positive and moderate correlation with minimum slice-wise YY directional eulerian strain ( $TTY^-$ ). This correlation in Segment 4 suggests that, its infarctions are more effective in global YY directional eulerian strain. This correlation with  $TTY^-$  in Segment 4, is also visible in Segment 5. The I/M% in Segment 5 also shows a strong correlation of 60% to slice-wise minimum circumferential strain ( $TCS^-$ ) and it suggests that the infarctions presence in Segment 5 is highly disturbed the whole slice's circumferential contraction. Moreover, the results show that I/M% in Segment 5 is also moderately correlated with slice-wise maximum efficient strain ( $TES^+$ ). The Segment 5's this correlation with slice-wise global strains, are also visible in Segment 6. In addition, I/M% in Segment 5 also shows more moderate correlation with maximum regional radial strain ( $PRS^+$ ) and with maximum regional XX directional eulerian strain ( $PXX^+$ ). The I/M% in Segment 6 also shows moderate correlations with  $PCS^-$ ,  $PES^+$ ,  $PXX^-$  and  $PXX^+$  which are approximately strong about 50-60%. However, the I/M% in Segment 7 does not shows any correlation with a higher significance and the I/M% in Segment 8 only shows a moderate correlation with  $PXY^+$ . As can be seen in Table 4.2, I/M%s in Segment 1, 2 and 7, 8 do not show strong relationships to strain measures like in other segments such as 4, 5 and 6. This observation suggests that the presence of infarctions in anterior and anteroseptal may not be highly effective in slice-wise global or regional, minimum and maximum strain alterations.

According to the results shown in Table 4.4, it can be seen that I/M% in Segment 9 is strongly correlated with slice-wise maximum radial strain( $TRS^+$ ) and it suggests that infarctions in Segment 9 is highly effective in whole slice's

radial extraction. However, similar to Segment 3, I/M% in Segment 9 also does not show any significant correlation with other maximum and minimum strain measures. This evidence suggests that inferospetal segments are not correlated strongly with I/M% according to results of selected strain measures.

Moreover, the results in Table 4.4 show that I/M% in Segment 10 is strongly correlated with maximum regional radial strain ( $PRS^+$ ). The I/M% in Segment 10 also exhibits moderate correlations of 50-60% with  $PRS^-$ ,  $PCS^-$ ,  $PXX^+$ ,  $TXX^-$  and  $TTY^-$ . When comparing this result with the results of Segment 4, it can be seen that I/M% in both Segment 4 and 10 show a moderate correlation to global slice-wise minimum YY directional eulerian strain ( $TTY^-$ ). This observation suggests that infarctions presence in inferior segments are correlated with  $TTY^-$ . Further, it can be seen that when it come from basal inferior to mid inferior, this correlation becomes stronger.

The I/M% in Segment 11 shows stronger correlations with  $PXX^+$ ,  $PCS^-$  and  $PXY^+$  while it shows several other moderate correlations. Moreover, the I/M% in Segment 12 shows strong correlations with  $PYY^-$ ,  $PCS^-$  and  $PXY^+$  while it shows several other moderate correlations. The anterior Segment 13, only shows a moderate correlation between  $TXX^+$  and it does not show any other significant correlation like in Segment 1 and 7.

The septal Segment 14 also shows only moderate correlations of 40-50% with  $TCS^+$  and  $TXX^+$ . This observation further suggests that infarctions presence in anterior, anteroseptal or septal is not highly effective to the selected maximum/minimum strain measures.

When considering the I/M% in Segment 15, 16 and correlation with the selected strain measures, it can be seen that more moderate correlations are visible than



Segment 13 and 14. Moreover, these correlations of Segment 15 and 16 share similar correlations with other inferior and lateral segments as well.

According to the results and observations of segment-wise correlation analysis, it can be seen that anterior, anteroseptal, inferoseptal, inferior, inferolateral, and anterolateral segments shows similarities in correlated maximum and minimum strain measures. It can also be seen that the segments 4,5, 6, 10, 11, 12, 15 and 16 show relatively higher number of moderate or strong correlations than the other segments. Moreover, the inferolateral and anterolateral segments show highest number of correlations. These results suggest that right side region of LV is likely to be more sensitive to motion and strain due to the presence of infarction. When considering the results of the anterior, anteroseptal, inferoseptal, inferior, inferolateral, and anterolateral segments wise correlation analysis in Table 4.5, it further suggests that inferolateral and anterolateral segments show the highest number of correlations and more stronger correlations than other arrangements in standard AHA segmentation. The Table 4.5 shows that both  $TTY^-$  and  $PRS^+$  shows moderate correlations in inferior, inferolateral, and anterolateral segments. Further, it can be observed that the strain measures that show moderate correlations in inferolateral, and anterolateral are largely similar.

This study also had several limitations. The main limitation of this study is the sample size that is 10 patients and all are only male patients. Another limitation of this study is using AHA segment-wise averaged I/M%. This segment-wise averaged I/M% might reduce the strength of the correlation coefficient.

### 4.6 Conclusion

In conclusion, this study has used data from tagged, cine and LGE CMR images. This study has incorporated 24 strain measures that are calculated over the full cardiac cycle using the motion estimation method described in this thesis. The result of the correlation analysis shows that regional analysis of correlation is more effective than global analysis. More strong correlations can be detected when it is dealing with regional measures. It can also be seen that the selected maximum and minimum strain measures can be used to provide prognosis information to predict infarctions in inferior, inferolateral, and anterolateral segments more effectively. However, selected maximum and minimum strain measures that are related to anterior, anteroseptal and inferoseptal segments do not show a strong possibility in providing prognosis information on myocardial infarctions or ischemia. Finally, it can also be seen that Eulerian strain measures are also showing a greater potential in providing information on myocardial infarctions.

# Chapter 5

## Conclusion and Future Work

This chapter concludes the thesis and suggests several directions for future work. Section 5.1 summarizes the technical contributions achieved in this thesis. Section 5.2 suggests some directions for future research.

### 5.1 Conclusion

#### 5.1.1 Cardiac Motion Estimation

In conclusion, we have proposed a novel method for cardiac motion estimation using both tagged and cine CMR image sequences. In this thesis, we have used SA slices to estimate 2D motion within myocardium. Moreover, the estimated 2D motion has been used to derive global and regional strain measures that includes; Lagrangian strains (radial and circumferential), Eulerian strains (in XX, XY and YY directions) and efficient strain (radial strain - circumferential strain). The evaluation of proposed method using synthetic and real data shows that the proposed method is capable of tracking material points over the cardiac cycle with

a minimum error while being robust to increasing noise and tag fading effect. It can be concluded that, the tag fading and its effects on motion estimation of tagged CMR, can be compensated by using the rich anatomical information in cine CMR images and using the rich regional motion information in tagged CMR images simultaneously. In addition, the proposed method shows that an optical flow based solution can be used effectively to estimate motion jointly using both cine and tagged CMR data. Since cine CMR images are routinely acquired as part of clinical MR image acquisition, extra effort is not needed for the data acquisition. Hence, it can also be concluded that the proposed motion estimation method can be practically used in clinical settings in order to derive 2D motion and strain information.

### 5.1.2 Correlation Analysis

The correlation analysis between I/M% and strain measures shows that the strains calculated over the full cardiac cycle can provide valuable prognosis in global and regional LV function analysis. It also shows that the regional analysis of correlation is more effective than global analysis in the study context. The study also shows that in inferior, inferolateral, and anterolateral segments tend to show stronger correlations than the other segments of LV. Moreover, this thesis shows the importance of Eulerian strains where the eulerian strains are also showing moderate and strong correlations like the other established strain measures such as peak Lagrangian strains.

### 5.2 Limitations and Future Work

One of the limitations of the proposed motion estimation method is that it only estimates 2D motion. Empirically, the same motion estimation may work with good accuracy in LA slices. However, future work will explore the estimation of 3D motion by incorporating LA slices of cine and tagged CMR as well. Further, by having 3D motion estimation, more descriptors such as ejection fraction, LV volume, LV mass and torsion can be derived in order to provide more details on cardiac function.

Future work in correlation analysis may include more patients' data with more descriptors. In addition to maximum and minimum strains, the time to maximum and minimum strains can also be used in analyzing relationship between I/M% and strains. Moreover, other descriptors such as ejection fraction, LV volume, LV mass and torsion can also be used in correlation study with an extended statistical analysis. Further, this correlation analysis and prognosis information identification can be viewed as a learning problem. Hence, future work might also include learning LV motion data in order to regress the I/M%.

Finally, the joint analysis of CMR can be extended to fuse more cardiac MRI imaging modalities in order to provide more patient specific information and visualization. Therefore, future work may explore the ways of fusing other CMR imaging modalities while preserving the motion of the heart.

# Bibliography

- [1] S. Mendis, P. Puska, B. Norrving, *et al.*, *Global atlas on cardiovascular disease prevention and control*. World Health Organization, 2011. xii, 2
- [2] Wikipedia, “Heart,” 2014. xii, 8
- [3] D. T. Ginat, M. W. Fong, D. J. Tuttle, S. K. Hobbs, and R. C. Vyas, “Cardiac imaging: part 1, mr pulse sequences, imaging planes, and basic anatomy,” *American Journal of Roentgenology*, vol. 197, no. 4, pp. 808–815, 2011. xii, 13, 14
- [4] M. D. Cerqueira, N. J. Weissman, V. Dilsizian, A. K. Jacobs, S. Kaul, W. K. Laskey, D. J. Pennell, J. A. Rumberger, T. Ryan, M. S. Verani, *et al.*, “Standardized myocardial segmentation and nomenclature for tomographic imaging of the heart a statement for healthcare professionals from the cardiac imaging committee of the council on clinical cardiology of the american heart association,” *Circulation*, vol. 105, no. 4, pp. 539–542, 2002. xii, 13, 14, 15, 16, 27, 41
- [5] D. Wei, “Computer aided analysis of late gadolinium enhanced cardiac mri,” 2013. xii, xiii, 22, 26, 27, 41, 43, 74, 76
- [6] S. Monda, C. Susan, O. Nael, B. David, and L. João, “Myocardial tissue tagging with cardiovascular magnetic resonance,” *Journal of Cardiovascular Magnetic Resonance*, vol. 11. xii, 25
- [7] W. H. Organization, “Cardiovascular diseases (cvds),” 2014. 1, 2
- [8] Wikipedia, “Coronary artery disease,” 2014. 3, 10

- [9] R. Chandrashekara, “Analysis of cardiac motion using mri and nonrigid image registration,” 2004. 3, 24, 26, 38, 39
- [10] H. Wang and A. A. Amini, “Cardiac motion and deformation recovery from mri: a review,” *Medical Imaging, IEEE Transactions on*, vol. 31, no. 2, pp. 487–503, 2012. 3, 18, 28, 31, 33, 35
- [11] A. Thorstensen, B. H. Amundsen, H. Dalen, P. Hala, G. Kiss, S. A. Aase, H. Torp, and A. Støylen, “Strain rate imaging combined with wall motion analysis gives incremental value in direct quantification of myocardial infarct size,” *European Heart Journal–Cardiovascular Imaging*, p. jes070, 2012. 4
- [12] F. Weidemann, C. Wacker, A. Rauch, W. R. Bauer, B. Bijmens, G. R. Sutherland, G. Ertl, W. Voelker, F. Fidler, and J. M. Strotmann, “Sequential changes of myocardial function during acute myocardial infarction, in the early and chronic phase after coronary intervention described by ultrasonic strain rate imaging,” *Journal of the American Society of Echocardiography*, vol. 19, no. 7, pp. 839–847, 2006. 4
- [13] E. Heiberg, H. Engblom, M. Ugander, and H. Arheden, “Automated calculation of infarct transmuralty,” in *Computers in Cardiology, 2007*, pp. 165–168, IEEE, 2007. 4
- [14] L. Rosendahl, “Infarct size and myocardial function: A methodological study,” 2010. 4
- [15] G. Weissman, M. Kern, A. Barac, M. A. Gonzalez, R. Torguson, R. Waksman, and A. Fuisz, “CMR in acute myocardial infarction: correlation between myocardial scar and echocardiographic strain,” *Journal of Cardiovascular Magnetic Resonance*, vol. 14, pp. 1–2, 2012. 4
- [16] Wikipedia, “Myocardial infarction,” 2014. 10
- [17] Wikipedia, “Cardiomyopathy,” 2014. 10
- [18] L. S. Lilly, *Braunwald’s heart disease: a textbook of cardiovascular medicine*, vol. 1. Elsevier Health Sciences, 2012. 11

- [19] Wikipedia, “How is coronary heart disease diagnosed?,” 2014. 11
- [20] N. F. Osman, “Measuring regional cardiac function using harmonic phase magnetic resonance imaging,” 2000. 11, 24
- [21] E. A. Zerhouni, D. M. Parish, W. J. Rogers, A. Yang, and E. P. Shapiro, “Human heart: tagging with mr imaging - a method for noninvasive assessment of myocardial motion.,” *Radiology*, vol. 169, no. 1, pp. 59–63, 1988. 18, 27
- [22] L. Axel and L. Dougherty, “Mr imaging of motion with spatial modulation of magnetization.,” *Radiology*, vol. 171, no. 3, pp. 841–845, 1989. 18
- [23] S. E. Fischer, G. McKinnon, S. Maier, and P. Boesiger, “Improved myocardial tagging contrast,” *Magnetic Resonance in Medicine*, vol. 30, no. 2, pp. 191–200, 1993. 18
- [24] U. of Virginia Health System, “Cine imaging,” 2014. 20
- [25] M. Vöhringer, H. Mahrholdt, A. Yilmaz, and U. Sechtem, “Significance of late gadolinium enhancement in cardiovascular magnetic resonance imaging (cmr),” *Herz Kardiovaskuläre Erkrankungen*, vol. 32, no. 2, pp. 129–137, 2007. 22
- [26] C. M. Kramer, W. J. Rogers, T. M. Theobald, T. P. Power, G. Geskin, and N. Reichek, “Dissociation between changes in intramyocardial function and left ventricular volumes in the eight weeks after first anterior myocardial infarction,” *Journal of the American College of Cardiology*, vol. 30, no. 7, pp. 1625–1632, 1997. 24
- [27] P. P. Sengupta, A. J. Tajik, K. Chandrasekaran, and B. K. Khandheria, “Twist mechanics of the left ventricle: principles and application,” *JACC: Cardiovascular Imaging*, vol. 1, no. 3, pp. 366–376, 2008. 26
- [28] V. V. Valindria, M. Angue, N. Vignon, P. M. Walker, A. Cochet, and A. Lalande, “Automatic quantification of myocardial infarction from delayed enhancement mri,” in *Signal-Image Technology and Internet-Based Systems (SITIS), 2011 Seventh International Conference on*, pp. 277–283, IEEE, 2011. 26



- [29] Q. Tao, J. Milles, K. Zeppenfeld, H. J. Lamb, J. J. Bax, J. H. Reiber, and R. J. van der Geest, “Automated segmentation of myocardial scar in late enhancement mri using combined intensity and spatial information,” *Magnetic Resonance in Medicine*, vol. 64, no. 2, pp. 586–594, 2010. 26
- [30] D. Wei, Y. Sun, S.-H. Ong, P. Chai, L. L. Teo, and A. F. Low, “Three-dimensional segmentation of the left ventricle in late gadolinium enhanced {MR} images of chronic infarction combining long- and short-axis information,” *Medical Image Analysis*, vol. 17, no. 6, pp. 685 – 697, 2013. 26
- [31] A. A. Amini, Y. Chen, M. Elayyadi, and P. Radeva, “Tag surface reconstruction and tracking of myocardial beads from spamm-mri with parametric b-spline surfaces,” *Medical Imaging, IEEE Transactions on*, vol. 20, no. 2, pp. 94–103, 2001. 30
- [32] A. A. Amini, Y. Chen, R. W. Curwen, V. Mani, and J. Sun, “Coupled b-snake grids and constrained thin-plate splines for analysis of 2-d tissue deformations from tagged mri,” *Medical Imaging, IEEE Transactions on*, vol. 17, no. 3, pp. 344–356, 1998. 30
- [33] S. Sampath and J. L. Prince, “Automatic 3d tracking of cardiac material markers using slice-following and harmonic-phase mri,” *Magnetic Resonance Imaging*, vol. 25, no. 2, pp. 197–208, 2007. 30
- [34] N. F. Osman, W. S. Kerwin, E. R. McVeigh, and J. L. Prince, “Cardiac motion tracking using cine harmonic phase (harp) magnetic resonance imaging,” *Magnetic Resonance in Medicine*, vol. 42, no. 6, p. 1048, 1999. 30, 31
- [35] T. McInerney and D. Terzopoulos, “Deformable models in medical image analysis: a survey,” *Medical Image Analysis*, vol. 1, no. 2, pp. 91–108, 1996. 30
- [36] P. Shi, A. J. Sinusas, R. T. Constable, E. Ritman, and J. S. Duncan, “Point-tracked quantitative analysis of left ventricular surface motion from 3-d image sequences,” *Medical Imaging, IEEE Transactions on*, vol. 19, no. 1, pp. 36–50, 2000. 30

- [37] P. Shi and H. Liu, “Stochastic finite element framework for simultaneous estimation of cardiac kinematic functions and material parameters,” *Medical Image Analysis*, vol. 7, no. 4, pp. 445–464, 2003. 30
- [38] P. Yan, A. Sinusas, and J. S. Duncan, “Boundary element method-based regularization for recovering of lv deformation,” *Medical image analysis*, vol. 11, no. 6, pp. 540–554, 2007. 30
- [39] J. Park, D. Metaxas, and L. Axel, “Analysis of left ventricular wall motion based on volumetric deformable models and mri-spamm,” *Medical Image Analysis*, vol. 1, no. 1, pp. 53–71, 1996. 30
- [40] N. F. Osman, E. R. McVeigh, and J. L. Prince, “Imaging heart motion using harmonic phase mri,” *Medical Imaging, IEEE Transactions on*, vol. 19, no. 3, pp. 186–202, 2000. 31
- [41] N. F. Osman and J. L. Prince, “Visualizing myocardial function using harp mri,” *Physics in medicine and biology*, vol. 45, no. 6, p. 1665, 2000. 31
- [42] T. Arts, F. W. Prinzen, T. Delhaas, J. Milles, A. C. Rossi, and P. Clarysse, “Mapping displacement and deformation of the heart with local sine-wave modeling,” *Medical Imaging, IEEE Transactions on*, vol. 29, no. 5, pp. 1114–1123, 2010. 31
- [43] Wikipedia, “Gabor filter,” 2014. 32
- [44] T. Chen and L. Axel, “Using gabor filter banks and temporal-spatial constraints to compute 3d myocardium strain,” in *Engineering in Medicine and Biology Society, 2006. EMBS’06. 28th Annual International Conference of the IEEE*, pp. 4755–4758, IEEE, 2006. 32
- [45] T. Chen, X. Wang, S. Chung, D. Metaxas, and L. Axel, “Automated 3d motion tracking using gabor filter bank, robust point matching, and deformable models,” *Medical Imaging, IEEE Transactions on*, vol. 29, no. 1, pp. 1–11, 2010. 32

- [46] A. Montillo, D. Metaxas, and L. Axel, “Extracting tissue deformation using gabor filter banks,” in *Medical Imaging 2004*, pp. 1–9, International Society for Optics and Photonics, 2004. 32
- [47] Z. Qian, D. N. Metaxas, and L. Axel, “Extraction and tracking of mri tagging sheets using a 3d gabor filter bank,” in *Engineering in Medicine and Biology Society, 2006. EMBS’06. 28th Annual International Conference of the IEEE*, pp. 711–714, IEEE, 2006. 32
- [48] D. Rueckert, L. I. Sonoda, C. Hayes, D. L. Hill, M. O. Leach, and D. J. Hawkes, “Nonrigid registration using free-form deformations: application to breast mr images,” *Medical Imaging, IEEE Transactions on*, vol. 18, no. 8, pp. 712–721, 1999. 32
- [49] E. Oubel, M. De Craene, M. Gazzola, A. O. Hero, and A. F. Frangi, “Multiview registration of cardiac tagging mri images,” in *Biomedical Imaging: From Nano to Macro, 2007. ISBI 2007. 4th IEEE International Symposium on*, pp. 388–391, IEEE, 2007. 32
- [50] J. L. Prince and E. McVeigh, “Motion estimation from tagged mr image sequences,” *Medical Imaging, IEEE Transactions on*, vol. 11, no. 2, pp. 238–249, 1992. 34, 38
- [51] M. A. Gennert and S. Negahdaripour, “Relaxing the brightness constancy assumption in computing optical flow,” 1987. 35
- [52] S. N. Gupta and J. L. Prince, “On variable brightness optical flow for tagged mri,” in *Information Processing in Medical Imaging*, vol. 3, pp. 323–334, Springer, 1995. 35
- [53] L. Dougherty, J. C. Asmuth, A. S. Blom, L. Axel, and R. Kumar, “Validation of an optical flow method for tag displacement estimation,” *Medical Imaging, IEEE Transactions on*, vol. 18, no. 4, pp. 359–363, 1999. 35
- [54] D. J. Fleet and A. D. Jepson, “Computation of component image velocity from local phase information,” *International Journal of Computer Vision*, vol. 5, no. 1, pp. 77–104, 1990. 35

- [55] S. N. Gupta, J. L. Prince, and S. Androutsellis-Theotokis, “Bandpass optical flow for tagged mr imaging,” in *Image Processing, International Conference on*, vol. 3, pp. 364–364, IEEE Computer Society, 1997. 35
- [56] J. L. Prince, S. N. Gupta, and N. F. Osman, “Bandpass optical flow for tagged mri,” *Medical physics*, vol. 27, no. 1, pp. 108–118, 2000. 35
- [57] L. Florack, H. C. van Assen, and A. Suinesiaputra, “Dense multiscale motion extraction from cardiac cine mr tagging using harp technology.,” in *ICCV*, pp. 1–8, 2007. 36
- [58] N. Carranza-Herrezuelo, A. Bajo, F. Sroubek, C. Santamarta, G. Cristóbal, A. Santos, and M. J. Ledesma-Carbayo, “Motion estimation of tagged cardiac magnetic resonance images using variational techniques,” *Computerized Medical Imaging and Graphics*, vol. 34, no. 6, pp. 514–522, 2010. 36, 38, 39, 44, 53
- [59] W. Kerwin, N. Osman, and J. Prince, “Image processing and analysis in tagged cardiac mri,” *Bankman, I., éditeur, Handbook of Medical Imaging, chapitre*, vol. 24, pp. 375–391, 2000. 36
- [60] B. D. Lucas, T. Kanade, *et al.*, “An iterative image registration technique with an application to stereo vision.,” in *IJCAI*, vol. 81, pp. 674–679, 1981. 36, 44, 45, 53, 66, 71
- [61] W. Shi, X. Zhuang, H. Wang, S. Duckett, D. V. Luong, C. Tobon-Gomez, K. Tung, P. J. Edwards, K. S. Rhode, R. S. Razavi, *et al.*, “A comprehensive cardiac motion estimation framework using both untagged and 3-d tagged mr images based on nonrigid registration,” *Medical Imaging, IEEE Transactions on*, vol. 31, no. 6, pp. 1263–1275, 2012. 37, 41
- [62] E. Waks, J. L. Prince, and A. S. Douglas, “Cardiac motion simulator for tagged mri,” in *Mathematical Methods in Biomedical Image Analysis, 1996., Proceedings of the Workshop on*, pp. 182–191, IEEE, 1996. 38

- [63] T. Arts, W. Hunter, A. Douglas, A. Muijtjens, and R. Reneman, “Description of the deformation of the left ventricle by a kinematic model,” *Journal of biomechanics*, vol. 25, no. 10, pp. 1119–1127, 1992. 38
- [64] M. J. Ledesma-Carbayo, J. Kybic, M. Desco, A. Santos, M. Suhling, P. Hunziker, and M. Unser, “Spatio-temporal nonrigid registration for ultrasound cardiac motion estimation,” *Medical Imaging, IEEE Transactions on*, vol. 24, no. 9, pp. 1113–1126, 2005. 38, 39
- [65] I. Smal, N. Carranza-Herrezuelo, S. Klein, P. Wielopolski, A. Moelker, T. Springeling, M. Bernsen, W. Niessen, and E. Meijering, “Reversible jump mcmc methods for fully automatic motion analysis in tagged mri,” *Medical image analysis*, vol. 16, no. 1, pp. 301–324, 2012. 38, 39, 53, 55, 58
- [66] C. Tobon-Gomez, M. De Craene, K. McLeod, L. Tautz, W. Shi, A. Henemuth, A. Prakosa, H. Wang, G. Carr-White, S. Kapetanakis, *et al.*, “Benchmarking framework for myocardial tracking and deformation algorithms: An open access database,” *Medical image analysis*, 2013. 39, 51
- [67] B. K. Horn and B. G. Schunck, “Determining optical flow,” *Artificial intelligence*, vol. 17, no. 1, pp. 185–203, 1981. 44, 52, 53
- [68] W. Y. Yang, W. Cao, T.-S. Chung, and J. Morris, *Applied numerical methods using MATLAB*. John Wiley & Sons, 2005. 48, 49
- [69] H. Gudbjartsson and S. Patz, “The rician distribution of noisy mri data,” *Magnetic Resonance in Medicine*, vol. 34, no. 6, pp. 910–914, 1995. 53